REPUBLIQUE DU CAMEROUN
Paix Travail Patrie
****
UNIVERSITE DE YAOUNDE I
****
CENTRE DE RECHERCHE ET DE FORMATION DOCTORALE EN SCIENCES, TECHNOLOGIES ET GEOSCIENCES
****
UNITE DE RECHERCHE ET DE FORMATION DOCTORALE PHYSIQUES ET APPLICATIONS
****
P.O BOX : 812, Yaoundé

Email : crfd_stg@uy1.uniet.cm

REPUBLIC OF CAMEROON
Peace Work Fatherland
****
UNIVERSITY OF YAOUNDE I
****
POSTGRADUATE SCHOOL FOR SCIENCE, TECHNOLOGY AND GEOSCIENCE
****
RESEARCH AND POSTGRADUATE TRAINING UNIT FOR PHYSICS AND APPLICATIONS
****
P.O BOX : 812, Yaoundé

Email : crfd_stg@uy1.uniet.cm

DYNAMICS OF ELECTROMECHANICAL DEVICES POWERED BY NONLINEAR ELECTRICAL TRANSMISSION LINES

Thesis

Submitted and defended publicly in fulfillment of the requirements for the degree of **Doctor of Philosophy** in Physics

Speciality: **Mechanics, Materials and Structures**

BIBLIOTHEQUE UNIVERSITAIRE UY1

By

KOUAMI MBEUNGA Nadine

Registration number: **07W384**

Master of sciences in Physics, Option: **Mechanics and complex systems**

Under the supervision of

NANA Bonaventure
Associate Professor
University of Bamenda

WOAFO Paul
Professor
University of Yaoundé I

YEAR 2023

UNIVERSITÉ DE YAOUNDÉ
THE UNIVERSITY OF YAOUNDE I

FACULTÉ DES SCIENCES
FACULTY OF SCIENCES

DÉPARTEMENT DE PHYSIQUE
DEPARTMENT OF PHYSICS

ATTESTATION DE CORRECTION DE LA THÈSE DE DOCTORAT/Ph.D

Nous, Professeur **NANA NBENDJO Blaise Romeo** et Professeur **ESSIMBI ZOBO Bernard**, respectivement Examinateur et Président du jury de la Thèse de Doctorat/PhD de Madame **KOUAMI MBEUNGA Nadine**, Matricule **07W384**, préparée sous la direction des Professeurs **NANA Bonaventure** (Université de Bamenda) et **WOAFO Paul** (Université de Yaoundé I), intitulée : « **Dynamics of electromechanical devices powered by nonlinear electrical transmission lines**», soutenue le Lundi, **10 Juillet 2023**, en vue de l'obtention du grade de Docteur/PhD en Physique, Spécialité **Mécanique, Matériaux et Structures,** option **Mécanique Fondamentale et Systèmes Complexes** attestons que toutes les corrections demandées par le jury de soutenance ont été effectuées.

En foi de quoi, la présente attestation lui est délivrée pour servir et valoir ce que de droit.

Fait à Yaoundé, le 18 JUIL 2023

Examinateur	Le Président du jury	Le Chef de Département de Physique
Pr NANA NBENDJO B. R	Pr ESSIMBI ZOBO Bernard	Pr NDJAKA Jean-Marie

REPUBLIQUE DU CAMEROUN
Paix Travail Patrie
****
UNIVERSITE DE YAOUNDE I
****
CENTRE DE RECHERCHE ET DE FORMATION DOCTORALE EN SCIENCES, TECHNOLOGIES ET GEOSCIENCES
****
UNITE DE RECHERCHE ET DE FORMATION DOCTORALE PHYSIQUES ET APPLICATIONS
****
P.O BOX : 812, Yaoundé

Email : crfd_stg@uy1.uniet.cm

REPUBLIC OF CAMEROON
Peace Work Fatherland
****
UNIVERSITY OF YAOUNDE I
****
POSTGRADUATE SCHOOL FOR SCIENCE, TECHNOLOGY AND GEOSCIENCE
****
RESEARCH AND POSTGRADUATE TRAINING UNIT FOR PHYSICS AND APPLICATIONS
****
P.O BOX : 812, Yaoundé

Email : crfd_stg@uy1.uniet.cm

DYNAMICS OF ELECTROMECHANICAL DEVICES POWERED BY NONLINEAR ELECTRICAL TRANSMISSION LINES

Thesis

Submitted and defended publicly in fulfillment of the requirements for the degree of **Doctor of Philosophy** in Physics

Speciality: **Mechanics, Materials and Structures**

By

KOUAMI MBEUNGA Nadine

Registration number: **07W384**

Master of sciences in Physics, Option: **Mechanics and complex systems**

Under the supervision of

NANA Bonaventure

Associate Professor

University of Bamenda

WOAFO Paul

Professor

University of Yaoundé I

YEAR 2023

DEDICATION

– To **LORD, GOD ALMIGHTY, THE CREATOR OF THE UNIVERSE**, who by his will, has allowed me the grace to accomplish this work.

– To my tender mother **TCHOUDJA MBEUNGA Jeannette**, who has always struggled without any remission to provide for my needs. This work is the fruit of the guidance you have always given me.

ACKNOWLEDGMENTS

This thesis is coming to the end. Behind this work, many persons have contributed, each one at his level to increase the quality of this thesis. Their support and assistance can never be overestimated. I would like to express my gratitude to them. This thesis is the fruit of moral and financial support of the special persons whom I would like to address my very kind gratitude:

My gratitude goes to my supervisor, Prof. WOAFO Paul, who allowed me to work in his research team. With the difficulties encountered, he was able to guide and catalyze this work. For his rigor, his prompt reaction to work, and the team spirit that he transmits.

To Prof. NANA Bonaventure, who by his simplicity and understanding, agreed to follow this work to its end by making it effective. Thank you for your availability and your advice. He has been a remarkable teacher by the theoretical and practical knowledge that he has provided since the Master cycle. My sincere gratitude professor.

I wish to express my acknowledgments to all the members of the public defense jury who have accepted to discuss and appreciate the results of this thesis.

I am grateful to Prof. NDJAKA Jean-Marie, the head of the Department of Physics, Faculty of Science, UYI, and the teaching staff of his department for their valuable teachings and their fruitful advice since my first-year undergraduate at this University.

I am grateful to Prof. KOFANE Timoléon Crépin, former Head of the Department of Physics, for the enlightening teachings.

I am thankful to Prof. NANA NBENDJO Blaise, for his teaching, his advice, and encouragement during difficult times.

I would like to thank Prof. Sifeu TAKOUGANG KINGNI for fruitful discussions and its advice.

I am grateful to late Dr. MBOUSSI Aissatou, for her dynamism, her great support, her availability, and her advice. She was a big sister to me and would have liked to accompany me in this work.

My gratitude here is expressed to Dr. CHAMGOUE CHEAGE André for his availability, its advice, and for fruitful discussions. You are an elder brother to me.

I would like to thank all my lab elders of the Laboratory of Modelling and Simulation in Engineering and Biomimetics and Prototypes (LaMSEBP) especially: Dr. ENJIEU KADJI Herve, Dr. ABOBDA Lejuste, Dr. SIMO Hervé , Dr. NDOUKOUO Ahoudou, Dr. DJORWE Philippe, Dr.NANHA Armand, Dr. TALLA MBE Jimmi, Dr. TALLA Alain, Dr. GOUNE Geraud, Dr. NGUEUTEU Serges.

I also thank all my labmates and Ph.D. students of LaMSEBP with whom I share wonderful moments and particularly Dr. METSEBO Jules, Dr. NDEMANOU Peguy, Dr. TSAPLA Rolande, Dr. TOKOUE NGATCHA Dianorre, Dr. NWAGOUM Peguy, Dr. Fankem Raissa Éliane, Dr. ANAGUE Lionel, Dr. NOTUE Arnaud, Dr. DONGMO Eric, Dr. MBA Clorian, Dr MAKOUO Lucienne, Dr. THEPI Raoul, Dr. SIMO DOMGUIA Ulrich, Dr. MBOU Bertrand, Dr. YOUMBI Dorota, Dr. ESSAMBA Ursule, Mr KOUEMOU CEDRIC, Mr KEMADJOU Issac, Mr MONKAM.

I would like to thank my family MBEUNGA, I especially think to: My Brother TCHAMBA Allen, My sisters NKOUKOUANN Eliane, KETCHANKEU Carine, KEMADJOU Béatrice, DANKEU Irène, YAMEDJEU Sandrine, GANOU Stéphanie. May the Lord continue to reinforce, and even perpetuate, the brotherhood and the spirit of love in our great family.

I would like to thank my husband KWEDI DITENG Prospère Yannick, to support me and be understanding during the end of this thesis

I would like to thank the TCHAPTCHET family, I especially think to: To late TCHAPTCHET Joseph, my Aunt YOPA Lysette, NKOUAMI Arnaud, TCHATON Chantal, MBATCHOU Henriette, YAKAM Serge. For the affection, they have always given me, for their education, their encouragement, and their support.

I would like to thank the NDANKEU family: DJEUKAM Flaubert, NGANOU Olivier, KETCHANKEU Virginie, YAMEDJEU Rosette, NDANKEU Giselle, NDANKEU Bibiane.

I thank all my brothers in law: NTSINDJA Jean Paul, MBATCHOU Chanfreri, NGASSA Auge, NANDA Patrick, WANGSO André, NDJEUMEN Arnaud for their support and encouragement.

I would like to thank my family in law: DITENG family and Mme Ngang Olga Yvette Charlotte. For their understandings and their advices.

I particularly thank my spiritual mother: NDJEUMEN Rachelle. For her spiritual assistance, hers encouragements.

I would like to thank my spiritual family. For their spiritual assistance.

All those whose names have not been mentioned here, but who have contributed in one or another way to the success of this work should hereby receive my sincere gratitude.

Contents

LIST OF ABBREVIATIONS

AC	Alternating Current
DC	Direct Current
EMS	Electromechanical System
FN	FitzHugh-Nagumo
FDM	Finite Difference Methods
HH	Hodgkin-Huxley
JDTL	Josephson Junction Discrete Transmission Line
JJTL	Josephson Junction Transmission Line
JTL	Josephson Transmission Line
KdV	Kordeweg-de-Vries
MaEMS	Macro Electromechanical Systems
MEMS	Micro Electromechanical Systems
NEMS	Nano Electromechanical Systems
NLETL	Nonlinear Electrical Transmission Line
ODE	Ordinary Differential Equation
PDE	Partial Differential Equation
RCLSJ	Resistance Capacitive Inductance Shunted Junction
RCSJ	Resistively Capacitively Shunted Junction
RF	Radio Frequency
RSFQ	Rapid Single Flux Quantum Electronics
SE	Semiconductor
SIS	Superconductor-Insulator-Superconductor
SNS	Superconductor-Normal Metal-Superconductor

List of Tables

List of Figures

ABSTRACT

An array of nanoelectromechanical beams driven by an electrical line of Josephson junctions equivalent models is firstly studied in this thesis. It is found that a single electromechanical system displays oscillations under a critical value of the DC bias current. In the case of an array of the electromechanical systems constituted of a series of coupled discrete Josephson junction with a beam placed at each node, the numerical simulation shows that as the electric signal flows in the discrete array, each beam executes a pulse-like motion coming back at each resting state as the electrical signal passes the node. When the bias current increases, the amplitude and period of the pulse-like shapes increase. One also notes the increase of the amplitude of the pulse-like shape when the magnetic field increases. The electromechanical system analyzed can be seen as a model for periodic nano-actuation processes or as a model of legs in a millipede system.

Secondly, the analysis of an array of electromechanical systems driven by an electrical line of Fitzhugh-Nagumo neurons is performed. It is shown theoretically and experimentally that a single electromechanical system can display different dynamical behaviors such as single and multiple pulse generation, transient and permanent chaos, and antimonotonicity according to the system parameters. In the case of an array of the electromechanical system constituted of a series of coupled discrete Fitzhugh-Nagumo neurons, the numerical simulation shows that as the action potential flows in the discrete array, each electromechanical system executes a pulse-like motion coming at each resting state as the electrical signal passes the node. Furthermore, this line can also carry an envelope of action potential and can be useful for various kinds of information processing systems.

Keywords: Electrical line, Nanoelectromechanical, Josephson junction, neuron, Fitzhugh Nagumo, pulse signal, antimonotonicity.

RESUME

Dans cette thèse, une rangée de nanopoutres actionnée par une ligne électrique de jonctions Josephson est premièrement étudiée. Nous constatons qu'un seul système électromécanique constitué d'une nanopoutre actionnée par une jonction Josephson effectue des oscillations au dessus d'une valeur critique du courant de polarisation. Dans le cas d'une ligne de jonctions Josephson discrète contenant une nanopoutre à chaque nœud, la simulation numérique montre que lorsque le signal électrique circule dans la ligne, chaque nanopoutre exécute un mouvement de type impulsion et revient à sa position initiale lorsque le signal électrique a passé le nœud. Lorsque le courant de polarisation augmente, l'amplitude et la période des impulsions générées augmentent. On note également l'augmentation de l'amplitude de la forme impulsionnelle lorsque le champ magnétique augmente. Le système électromécanique analysé peut être considéré comme un modèle pour les processus d'actionnement périodique à l'échelle macroscopique, microscopique ou nanoscopique. Et également comme un modèle de pattes d'un robot de mille-pattes.

Ensuite, une rangée de bras électromécaniques couplée à une ligne électrique de neurones Fitzhugh-Nagumo est analysée. Nous avons montré théoriquement et expérimentalement qu'un bras électromécanique alimenté par un neurone de Fitzhugh-Nagumo peut afficher en fonction des paramètres du système différents comportements dynamiques tels que: les impulsions simples et multiples, le chaos transitoire et permanent et l'antimonotonie. Dans le cas d'une ligne de neurones de Fitzhugh-Nagumo discrète ayant à chacun de ses nœuds un bras électromécanique, la simulation numérique montre que lorsque le potentiel d'action passe dans la ligne discrète, chaque bras exécute un mouvement de type impulsion et revient à sa position initiale. De plus, cette ligne peut également faire propager une enveloppe de potentiel d'actions et peut par conséquent être utile pour divers types de systèmes de traitement de l'information.

Mots clés: Ligne électrique, électromécanique, jonction Josephson, Neurone, Fitzhugh Nagumo, impulsion, antimonocité.

GENERAL INTRODUCTION

Different types of oscillators can be used to actuate mechanical arms, among which we can name the Josephson junction oscillator and Fitzhugh-Nagumo oscillator. One particular interest in the Josephson junction is its potential to generate high-frequency signals ranging from Gigahertz to Terahertz [1, 2]. Thus, it is generally considered as a microwave radiation source and can be used for practical applications such as Superconducting Quantum Interference Devices (SQUIDs), detectors, digital logic circuits, and voltage standards [3–6]. Because of its large range of frequency variation and the high values of the frequencies, one can think of supplying some actuation processes at the nano level using a Josephson junction. This will lead to high-frequency nanoelectromechanical systems.

The usefulness of the Fitzhugh-Nagumo model is its ability to generate low and moderate frequency signals. Being most used because of its simplicity and its small equivalent circuit [7], Fitzhugh-Nagumo model is a relaxation oscillator [8]. It is also well known as a generalization of the Van der Pol equations that are used to model the behavior of excitable systems [9]. The excitability represents the fact that from his resting state, if an excitable cell receives a stimulus (small perturbation) at a brief time interval, the membrane potential of the cell reaches a threshold value and generates an action potential before returning to its resting state [10–12]. For the actuation tasks, we will analyze a system where the Fitzhugh-Nagumo neuron is used to control a mechanical arm. This is similar to the coupling between a biological neuron and a muscle. In fact, when the brain decides to move part of the body and gives the command to the motor neurons to execute this movement, it is the muscles at the end of the chain of command that ultimately contract to move the body part concerned. To transmit this command, the axons of these motor neurons, emerging from the spinal cord, form a nerve that extends to the muscles. Where the tip of each axon comes into proximity with a muscle fiber, it forms a synapse with that fiber.

Another way is to consider an electrical line in which an electrical signal propagates steadily with a constant shape. This requires some special electrical lines such as nonlinear electrical transmission lines which are able to propagate special electrical signals such as solitons [13–17]. In these electrical transmission lines, the signal can be inserted periodically at one entrance

node. Each signal introduced in the line will propagate along the line. An example of such electrical transmission lines, representing a discrete model of myelinated nerve fibers has been used to power an array of electromechanical systems [18].

Thus, many research activities have considered arrays of Josephson junctions [2, 19–24] in order to appreciate the output power. This is not the case with a single Josephson junction which is unable to deliver high power. It is well known that Josephson junction equivalent model and Fitzhugh-Nagumo model have been widely studied as nonlinear electrical transmission lines where long Josephson junctions and arrays of discrete Josephson junctions exhibit soliton-like excitations [25, 26]. Likewise, Fitzhugh-Nagumo neuron displays the nerve impulse during its propagation evolve from cell to cell by keeping their shape [27–30]. As the nano-actuation is concerned, scientists and engineers are interested in the design of a large ensemble of nano-actuators. This can be obtained by coupling several nanoelectromechanical systems through their mechanical parts or through the electrical parts with different types of coupling. In the same manner, the legs of millipedes can be viewed as an array of Fitzhugh-Nagumo neurons coupled each to an electromechanical system. Thus, following the idea of Ref. [18], we consider in this thesis the dynamical behavior of an array of electromechanical devices, each of which is placed at a node of the discrete array. such an electromechanical system can be used model for macro, micro, and nano-actuation, but also a model for the legs of artificial millipedes. Indeed, millipedes move their legs in a wave-like undulation along their body propelling themselves forward (or backward) against the substrate [31, 32].

The research leads to three important contributions to the field of electromechanical systems.
− The first purpose of our thesis was to study the dynamical behavior of nano-beams motion in an array constituted of coupled discrete Josephson junctions.
− The second main aim of the thesis was to analyze the dynamical behavior of an array of electromechanical systems powered by an array of Fitzhugh-Nagumo neurons.
− The third purpose of our work was to study experimentally the system constituted of one single Fitzhugh-Nagumo neuron coupled magnetically to a mechanical arm.

The present work is divided into three chapters and organized as follows:

Chapter one is concerned with the literature review on networks of electromechanical systems, discrete Josephson junction transmission lines, and Fitzhugh- Nagumo neuron. We will conclude this chapter by recalling the problems to be solved in this thesis.

The physical description and mathematical models of the systems analyzed in this thesis are presented in chapter 2. Here, the theoretical and experimental methods are also investigated. The types of equipment and components used during our experimental work are presented.

In Chapter 3, we present our obtained analytical and simulation results. We analyze the effects of some parameters on the behavior of the system. The comparisons are then made between the theoretical results and experimental ones.

We end this thesis with a general conclusion where the work is summarized and perspectives for future investigations are proposed.

Chapter 1

LITERATURE REVIEW AND PROBLEM STATEMENT

Introduction

For several decades, biomimetics and bioengineering contribute to significant progress in the technology of multilegged locomotion. This thesis is embedded in biomimetics, in particular electromechanical systems which are focused on the research question of how to technically mimic the behavior of many legs. Some information about networks of electromechanical systems is given in this chapter. Discrete Josephson junction transmission lines as well as Fitzhugh-Nagumo neuron are also presented. The problem statement of the thesis is discussed at the end of this chapter.

1.1 NETWORKS OF ELECTROMECHANICAL SYSTEMS

1.1.1 Definition of electromechanical systems

The electromechanical system focuses on the interaction of electrical and mechanical systems as a whole and how the two systems interact with each other. This interaction is done through a coupling. the coupling between the electrical part and the mechanical part can be an electromagnetic [33], a piezoelectric [34], a piezoresistive, or a capacitive coupling [35]. According to their size, Electromechanical systems (EMSs) are classified into three domains as follows:

a) Macro-electromechanical systems

Macroelectromechanical system (MaEMS) is classified in the category of big sizes EMS [36]. They can be found in various fields such as domestic equipment, manufacturing, communication, and energy production. Mechanical motion is typically converted into electrical energy and vice versa through various transducers mechanisms. However, although conversion can have place through many converters, magnetic coupling is generally used in experiments as in most practical devices. In these devices, MaEMSs thus consist of a subsystem (an electric

circuit), a magnetic subsystem (magnetic field), and a mechanical subsystem. The magnetic subsystem fits between the electrical and mechanical subsystems and acting in the energy conversion. When coupled with an electric circuit, the magnetic flux interacting with the current in the circuit would produce a force on a mechanical part. On the other hand, the motion of the mechanical arm in the magnetic field causes an induced electromotive force in the circuit.

b) Microelectromechanical systems

Microelectromechanical system (MEMS) is a process technology used to create tiny integrated devices or systems that combine mechanical and electrical components. They can range in size from a few micrometers to millimeters [37]. These devices (or systems) can sense, control, and actuate on the micro-scale, and generate effects on the macro scale. They are used in fields as varied as automotive, aeronautics, medicine, biology (BioMEMS), and telecommunications. applications have gone into production while in others, they remain in the field of research and development. Although MEMS can be manufactured aseptically and hermetically. Biology and medicine are areas where MEMS are very interesting. It is quite possible to create autonomous systems that can diagnose and act within the human body.

c) Nanoelectromechanical systems

Nanoelectromechanical systems (NEMS) are a class of devices integrating electrical and mechanical functionality on the nanoscale. The system is extremely small in size (dimension less than one cubic micrometer) [38]. Unlike MEMS, NEMS are an emerging technology. NEMS have long been tools devoted to fundamental studies to probe mesoscopic physical mechanisms. Their extremely small size makes them extremely sensitive to any external stimulus. NEMS are interesting both in terms of fundamentals and applications. They often have high mechanical resonance frequencies typically from (1 to 100 MHz) and dissipate low quantities of energy (mechanical and electrical). They are sensitive enough to enable mass measurements to be realized at the single molecular level (molecule counting), to count electrons or phonons one by one, or to measure forces approaching the pico-Newton. In other words, NEMS respond to requests as fast as the size of the nanobeam is small. It is, therefore, possible to actuate high-frequency NEMS with a thermomechanical force, something that was not possible with microsystems. This also means that a NEMS sensor can be used to detect fast phenomena.

The mechanical part can be of various nature (rigid or flexible arm). It can also be consisting of springs, movable rods, pendulums, discs... EMS can be linear or nonlinear. It is considered linear when the equations that model the behavior of the electrical and/or mechanical parts are linear. It is nonlinear if at least one of the two parts is nonlinear. Nonlinearity in the mechanical part may be due to the behavior of several components: damping coefficient, elastic

coefficient, high-value deformation giving rise to geometric nonlinearity, etc. The electrical part is generally consisting of resistors, capacitors, potentiometers, coils, relays, diodes, transistors, and integrated circuits. Nonlinearity in the electrical part is generated by the presence of nonlinear components such as capacitors, resistors, or coils. many works have been carried out to investigate their different dynamical states by building the electrical circuits on the base of the components mentioned above [33, 36].

1.1.2 Dynamical behavior of single Electromechanical system with nonlinear components

Many essential works of which the list is non-exhaustive have already been done in the case of single nonlinear EMS. The interesting results on the dynamic behavior have been observed and have improved the quality of electromechanical devices in modern life. Mogo and Woafo [39] investigated the dynamics modeling of a cantilever arm magnetically coupled to a nonlinear electric circuit. It is shown that the nonlinearity is from the capacitor component. Moreover, they found that the system presents various types of nonlinear behaviors including chaos. Chedjou et al. [40] studied the dynamics of a self-sustained electromechanical system consisting of an electrical Van der pol oscillator coupled to a mechanical Duffing oscillator. They observed that the system can exhibit harmonic oscillators, quenching phenomena, and Shilnikov chaos. Other researchers are Kitio and Woafo [36, 41, 42] who studied analytically, numerically, and experimentally some self-sustained electromechanical systems. The systems considered in these works are made up of an electrical implementation consisting of different types of oscillators such as (Van der pol-Duffing oscillator, Rayleigh-Duffing oscillator) actuating a mechanical arm (rigid and flexible). The authors showed that these systems exhibit periodic oscillations, quenching phenomena, bifurcation, and chaos oscillations. Yamapi et al. [43–47] in their studies, have performed several works on a single electromechanical system for which many dynamics behaviors have been observed. By the method of harmonic balance and the Floquet theory, they obtained the frequency responses and stability boundaries, and also reported various types of bifurcation sequences. The transition to chaotic behavior is found using numerical simulations. The canonical feedback controllers have been used to drive the electromechanical device from a chaotic trajectory to a regular target orbit. Ngueuteu and Woafo [48] included a Fractional-order to describe an electromechanical system and detailed attention is granted to the bifurcations that can occur in the dynamics of a single uncoupled electromechanical system as the fractional order varies.

1.1.3 Networks of electromechanical systems

A great interest devoted to networks of the electromechanical systems is investigated several decades ago. A network of the electromechanical systems is constituted of several coupled electromechanical systems. It is inspired by the connectivities between cells which are frequently observed in nature and applied to many branches of electromechanical engineering and many other disciplines. An important element in the dynamics of a network is the coupling phenomenon. It can lead to a failure of signal propagation or transmission signal in the system depending on the strength of coupling. The coupling schemes can be divided into two qualitatively different groups. The first one is a global coupling where all oscillators are connected with each other directly [49, 50]. The second type is a local coupling where the single node is connected to oscillators in its nearest neighborhood [51, 52]. Such coupling can be bidirectional or unidirectional. In a bidirectional local coupling, the signal is transmitted and received simultaneously by all connected systems while in a unidirectional local coupling, the signal is transmitted in one direction from one to another.

Due to interactions between nodes in networks, there exist different types of configuration networks: a ring, a chain, a star, or a random configuration.

A ring configuration network is a type of network where the node is exactly connected to two other nodes, forward and backward thus forming a single continuous path for signal propagation. Many researchers performed their works in this type of network. Ngueuteu et al. studied the stability of a synchronized network of N chaotic electromechanical devices, coupled through a linear capacitor and resistance, connected in series [53]. Yamapi and Woafo investigated the dynamics of a ring of four mutually coupled identical self-sustained electromechanical devices both in their autonomous and non-autonomous chaotic states. By varying the coupling strength, the transition boundaries that can occur between instability and complete synchronization states have been performed [54]. Furthermore, Taffoti and Woafo studied the synchronization in a ring of mutually coupled electromechanical devices. In this work, each device consisted of an electrical Duffing oscillator coupled magnetically with a linear mechanical oscillator. They found the ranges for cluster and complete synchronization in the regular state or in the chaotic state [55]. Tchakui et al. in their works [56] studied the bifurcation structures in three unidirectionally coupled nonlinear electromechanical systems with no external signal. They found that the magnetic field and the damping coefficient control the appearance of Hopf bifurcation. Also, they found that for the small delay and generative process strength, the system remains motionless, leading to periodic oscillation at critical value.

Concerning a chain configuration network, it is an opened ring with an infinite number of

elements. In This configuration, the last unit is not connected to the first one. It is described in the same way as the ring configuration. The particularity of this case lies in its boundary conditions. Some works have been done in a chain configuration network [57–59].

Finally, a network of mutually coupled EMS following a star configuration is a configuration in which unit 1 is coupled to all the other units of the network and all the other units are coupled only to unit 1 [57].

1.2 DISCRETE JOSEPHSON JUNCTION TRANSMISSION LINES

1.2.1 Generalities on nonlinear electrical transmission lines

Nonlinear electrical transmission line (NLETL) is an ordinary transmission line whose electrical characteristics are functions of local voltages and currents. Its structure usually consists of repeated identical subcircuits made up of lumped elements. This structure can be either discrete or continuous. Nonlinear electrical transmission lines are interconnected. Since pioneering works by Hirota and Suziki [60] on electrical line simulating Toda lattices [61], a growing interest has been devoted to the use of the NLETLs in general for the study of the nonlinear modulated wave, pulse solitons, envelope pulse (bright) solitons, hole (dark) solitons [62, 63], intrinsic localized modes also called breathers [64, 65], modulational instability [66, 67], in particular for the study of nonlinear wave propagation [68, 69].

Over the past decade, the nonlinear propagation of signals in NLETLs was investigated theoretically and experimentally [70–72] by studying linear stability and the higher-order solutions in NLETL. These nonlinear electrical transmission lines serve as nonlinear dispersive media where electrical solitons can propagate in the form of voltage waves without changing their shape. A balancing mechanism between nonlinearity and dispersion is responsible for the appearance of soliton phenomena [73]. Solitons can propagate over long distances and survive collisions. These are highly localized solutions in space of nonlinear partial differential equations. They have infinite support due to the exponential decrease of their profile at large distances [74]. The studies of NLETLs have progressed in both the theoretical field [75] and technology [76–78] and are used in a variety of applications: Indeed, NLETLs have proven to be extremely useful in pulse generation and shaping using nonlinear phenomena having a wide range of frequencies from DC to 100 GHz [79, 80].

There exist many mathematical models of nonlinear electrical transmission lines to inves-

tigate the propagation of solitons such as nonlinear Schrodinger equation [81, 82], Kordeweg-de-Vries (KdV) equation [83], Sine-Gordon equation (long Josephson Junctions) [84], to name just a few. In the reaction-diffusion equations, a mathematical model of nonlinear electrical transmission lines are Hodgkin-Huxley equation [85], Fitzhugh-Nagumo equation [86], Morris Lecar equation [87] and so on.

1.2.2 Short Josephson junction

Brian David Josephson in 1962 predicted theoretically the Josephson effect [88] and in 1963 it was for the first time experimentally observed by Anderson and Rowell [89]. The principle of the Josephson effect is that the phase difference ϕ between superconductors 1 and 2 in Figure 1.1 generates a cooper pair current passing through the insulating barrier. This barrier is also called Junction. Thus, the Josephson junction is a device that consists of two superconductors weakly separated by a thin insulating barrier [90, 91] as illustrated in Figure 1.1. ψ_L and ψ_R are macroscopic wave functions of cooper pairs in the first and second electrodes respectively.

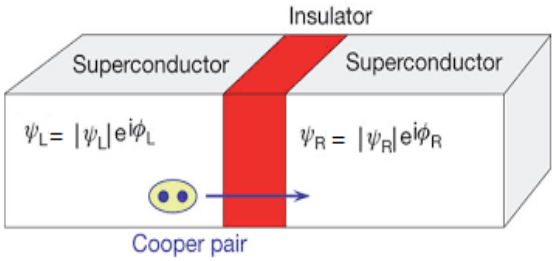

Figure 1.1: Schematic diagram of a Josephson Junction [92].

If The insulating barrier is thick, the electron pairs can not get through; but if the layer is thin enough (approximately 10 nm) there is a probability for electron pairs to the tunnel. This effect became known as Josephson tunneling. The tunnel effect is one of the most emblematic phenomena of mechanics quantum. Conventionally, a given energy barrier is impassable by any particle whose energy is lower. Tunneling junctions have an SIS (Superconductor-Insulator-Superconductor) type structure. Josephson effects can be studied on various contact types besides the tunnel contact such as Superconductor-Normal Metal-Superconductor (SNS), micro bridges, proximity effect bridge, point contact, bloc-type junction [93], Figure 1.2.

The conducting region of the two last types of weak links is shown schematically in the circle on the bottom. S stands for Superconductor, S' for the Superconductor with reduced critical parameters, N for Normal metal or alloy, SE for Semiconductor (usually highly doped),

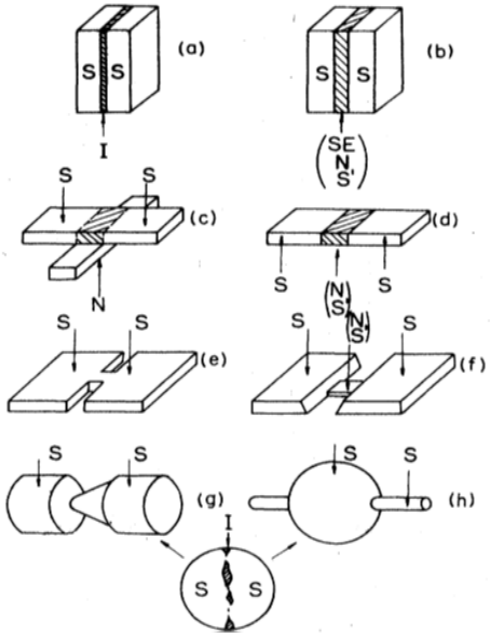

Figure 1.2: Different types of structures where the Josephson effect can take place. (a) tunnel junction, (b) Sandwich, (c) proximity effect bridge, (d) ion implanted bridge, (e) microbridge, (f) variable thickness bridge, (g) point contact; (h) blob-type junction [91].

I stands for Insulator. Normal metal barriers typically have thicknesses between 10 nm and 100 nm [94]. The first dynamics Josephson effect equation is:

$$i(t) = I_c \sin(\phi(t)), \tag{1.1}$$

where $\phi = \phi_R - \phi_L$ is the phase difference between the macroscopic wave functions that describe the paired electrons of the two electrodes, I_c is a function parameter called the critical current, that is the maximum current that can pass through the junction. It depends on the temperature, the applied magnetic field, the geometry of the superconductors and the barrier, and the materials used. $i(t)$ is a cooper current through the Josephson Junction. The second dynamics Josephson effect equation is:

$$\frac{d\phi}{dt} = \frac{2e}{\hbar} v. \tag{1.2}$$

In the above equation, v is the potential difference across the junction, the physical constant $\phi_0 = \dfrac{\hbar}{2e}$ is the magnetic flux quantum where $\hbar$ denotes the reduced Planck's constant and e the electron charge. These equations define the relation between the Josephson current $\imath$ and the voltage v using the phase ϕ as an intermediary [95, 96].

There are three main effects predicted by Josephson according to the Josephson equations:

- **The DC Josephson effect:**

In the absence of a voltage, the supercurrent flow between the two superconductors separated by a thin insulating barrier and may take values between $-I_c$ and I_c.

• **The AC Josephson effect:**

In the presence of a constant voltage, the Josephson current will oscillate at a frequency $f = \frac{2ev}{h}$ called the Josephson frequency where $\frac{2e}{h} = 483.6$ GHz/mV.

• **The inverse AC Josephson effect:**

If an alternating current of radian frequency ω is applied to the junction terminals by microwave irradiation, the current of cooper pairs tends to synchronize with this frequency (and its harmonics) and a direct voltage appears at the junction terminals. This synchronization is revealed in the current-voltage characteristics by the appearance of voltage steps at integer multiples of the value $V = \frac{h}{2e} f$.

Josephson junctions are theoretical and applied devices extensively studied in the field of nonlinear dynamics and materials sciences [97–100]. Different models to study the dynamics of a single Josephson junction are performed such as RCSJ (Resistance Capacitive shunted junction) [101, 102]. This model was first explored by Stewart [103] and Mc Cumber [104]. In this model, conduction through the junction includes three independent components: an ideal Josephson junction which carries a supercurrent, a superconducting current due to the tunneling of quasiparticles, and a displacement current associated with the junction capacitance. Thus, the equivalent circuit of a Josephson junction base on the RCSJ model is shown in Figure 1.3. Here quasiparticle conduction is represented by the linear resistance R, displacement current by the capacitance C, and pair tunneling by an ideal Josephson element JJ, indicated by a cross. I_S is an external current source necessary to bias the junction. RCLSJ (Resistance, Capacitive, Inductance shunted junction) [97,99,105,106]. This model is found more appropriate to generate chaotic oscillation with external DC bias only. It is noted that a refinement of the RCSJ model exists in which the resistance R is assumed to be nonlinear and is a function of the applied voltage [107]. This model is theoretically more suited to SNS (Superconductor- Normal metal-Superconductor) or weak links. In our work, we will focus on the RCSJ model where R is linear.

Several investigations in the nonlinear dynamics by using a single Josephson junction based on RCSJ have been widely explored. Valkering and al. [109] have investigated analytically and numerically the dynamics of two capacitively coupled Josephson junctions based on the RCSJ model. The work revealed that below a certain value of the coupling capacitance, the dynamics take place on a two-dimensional torus in the phase space. Furthermore, The authors of ref. [110] have worked on the bifurcation and transition to chaos in a Josephson junction.

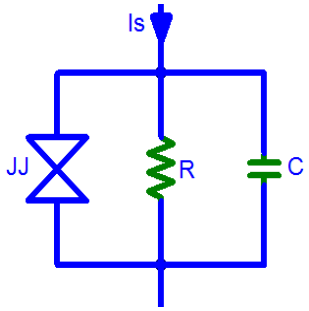

Figure 1.3: Equivalent circuit of a Josephson Junction according to the RCSJ model [108].

They observed that the system can show chaotic behavior in some regions of the parameter space both the DC and AC current are applied to the junction.

1.2.3 Josephson junction transmission lines

A Josephson junction is a high-frequency oscillator with high-frequency applications [1, 22]. Two major problems are encountered in the application of the Josephson junction: the power generated by a single junction is too small and secondly the linewidth of the emitted radiation is undesirable. [2]. To solve those problems, it is important to note that the application of Josephson junctions as high-frequency oscillators crucially depends on achieving high enough output power. The possibility to increase the power transmitted and to increase the radiation output power is through the Josephson transmission line which is supposed to be a large number of Josephson oscillators. Josephson junction transmission line (JJTL) is a long Josephson junction in which a vortex (fluxons or soliton) can propagate freely [111]. It can be constructed in different geometries, and the junction geometry has a significant effect on the junction dynamics. The most extensively studied geometries are the overlap geometry, the inline geometry, and the annular geometry [112], depicted in Figure 1.4.

The first two are somewhat similar in that they consist of finite length, quasi-one-dimensional strips; the essential difference between them is how the bias current is applied to them. In the overlap geometry, the current is applied perpendicular to the long dimension of the junction, whereas, in the inline geometry, it is applied parallel to the long dimension. The annular geometry, instead is qualitatively different, consisting of a strip closed upon itself in an annular. Although somewhat more difficult to construct and control from the point of view of fabrication technology, the annular geometry junction offers the interesting possibility of studying soliton dynamics in the absence of boundary reflection effects. The structure of Josephson junction transmission line equivalent circuit has been shown in ref. [114]. Several studies have used

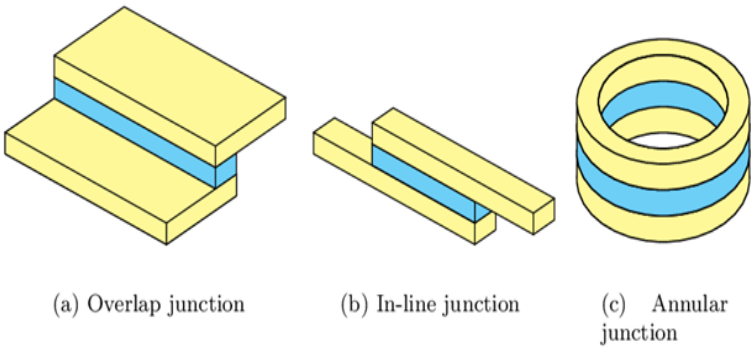

Figure 1.4: Different geometries of Josephson Junction devices: a) Overlap, b) Inline, c) Annular geometry [113].

Josephson junction transmission lines in the concept of new designs such as information storage, processing circuity, using Josephson transmission line by employing flux quantum (fluxon) as information bit [115–117]. The Josephson junction transmission line in one dimension is described by the normalized nonlinear partial differential equation of ref. [114, 117–119].

1.2.4 Josephson discrete transmission lines

Josephson discrete transmission lines (JDTLs) have attracted considerably high interest, both as an excellent laboratory for nonlinear dynamics and because of their relatively wide area of applications. The JDTL belongs to the basic element set of a quickly developing family of superconducting digital circuits, rapid single flux quantum electronics (RSFQ) [120]. The basic dynamic properties of such lines were recently a subject of several studies [120–123]. JDTL is known as Josephson junction array and the need to generate high power as a continuous long Josephson transmission line (JTL). The advantages of JDTL have over a Josephson transmission line are that the vortex velocity of JDTL can be higher so that higher frequencies are accessible and that parameters can over leaving more freedom when designing circuits [124]. Also, long JTL shows very promising attributes but the JDTL has demonstrated to have superior properties for microwave applications and electronics due to its [125]. The works have been done by using DJTL [126–128]

1.3 FITZHUGH-NAGUMO NEURON

1.3.1 Neuron cell structure

The fundamental task of the nervous system is to communicate and process information. Animals, including humans, perceive, learn, think, deliver motion instructions, and are aware of themselves and the outside world through their nervous systems. The basic structural units of the nervous system are individual neurons. There are approximately 100 billion neurons in the human brain [129] and each is linked to thousands of other neurons. They have two physiological properties: excitability and conductivity which are characterized by their function such as the sensory neurons respond to stimuli such as touch, sound, or light that affect the cells of the sensory organs and they send signals to the spinal cord or brain.

Motor neurons receive signals from the brain and spinal cord and then carry them to the outside to control the movement of muscles and the activities of glands. Interneuron sends messages from one neuron to another. Different types of neurons show great diversity in size and shape, which makes sense given the tremendous complexity of the nervous system and the huge number of different tasks it performs. Some examples are Pyramidal cells (neurons with triangular soma), Purkinje cells (huge neurons in the cerebellum, Basket cells (interneurons, found in the cortex and cerebellum), Spiny cells (most neurons in the corpus striatum) [130,131]. A typical neuron possesses a cell body (the soma), dendrites, and an axon as illustrated in Figure 1.5

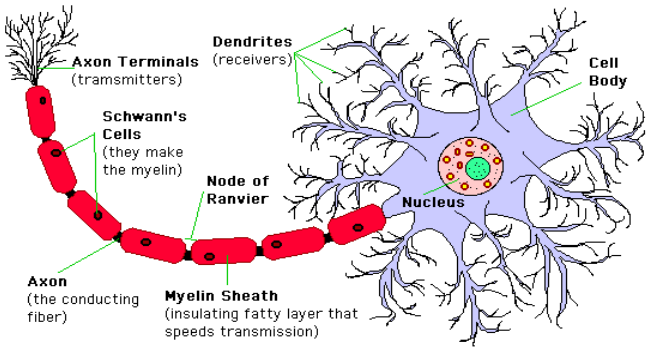

Figure 1.5: Schematic drawing of a neuron [132].

– **Cell body**

Also known as soma, the cell body carries genetic information, maintains the structure of the neuron, and provides energy to drive activities. Like other cell bodies, a neuron's soma

contains a nucleus and specialized organelles. The diameter of the cell body is in the order of 5 to 100 micrometers.

– **Dendrites**

Dendrites receive and process signals from the axons of other neurons. Neurons can have more than one set of dendrites, known as dendritic trees. They can receive many thousands of input signals.

– **Axons**

An axon is a tube-like structure that propagates the integrated signal to specialized endings called axon terminals. These terminals communicate with adjacent neurons, muscles, or target organs. Some axons are covered with myelin, which acts as an insulator to minimize the dissipation of the electrical signal as it travels down the axon, greatly increasing the speed of conduction. The axon or nerve fibre has a diameter between 1 and 15 micrometer. Its length varies from, millimeters to more than one meter. Along the axon, there are periodic gaps in the myelin sheath. These gaps are called nodes of Ranvier and are sites where electrical impulses travel along the axon. The unmyelinated spaces are about one micrometer long.

There are three types of neurons according to their structure. The first type is called unipolar neurons and they have only one structure that extends away from the soma. The second type named bipolar neurons has one axon and one dendrite extending from the soma. Finally, the multipolar neurons contain one axon and multiple dendrites.

Every neuron contains charged ions whose concentration is different inside and outside the cell. This difference is called the membrane potential. The permeability of the axon membrane to sodium Na^+ and potassium K^+ ions includes ion channels that permit electrically charged ions to flow across the membrane and ion pumps that chemically transport ions from one side of the membrane to the other.

The movement of ions across the nerve membrane is governed by two opposing forces: concentration gradient and electrical gradient. Concentration gradient means the difference in the distribution of ions between the inside and the outside membrane. And these concentration differences are caused by active pumps. The further electrical gradient is the difference in positive and negative charges across the membrane. The membrane potential at which these two opposing forces are balanced is called the equilibrium potential [133].

a)Resting potential

A neuron at rest is negatively charged: the inside of a cell is approximately 70 millivolts more negative than the outside (70 mV, note that this number varies by neuron type and by species). This voltage is called the resting membrane potential presented in Figure 1.6.

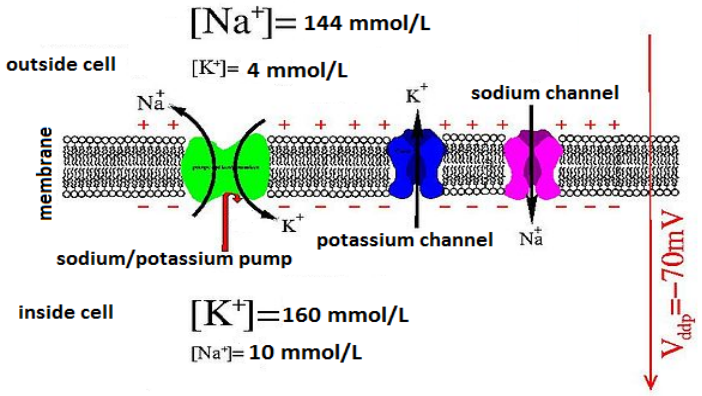

Figure 1.6: The resting membrane concentrations and potential [134].

It is caused by differences in the concentrations of ions inside and outside the cell. At rest, the neuron is said to be in a polarized state. The difference in the number of positively charged potassium ions K^+ inside and outside the cell dominates the resting membrane potential. When the membrane is at rest, K^+ ions accumulate inside the cell due to a net movement with the concentration gradient. The negative charge within the cell is created by the cell membrane being more permeable to potassium ion movement than sodium ion movement. In neurons, potassium ions are maintained at high concentrations within the cell while sodium ions are maintained at high concentrations outside of the cell.

The cell possesses potassium and sodium leakage channels that allow the two cations to diffuse down their concentration gradient. However, the neurons have far more potassium leakage channels than sodium leakage channels. Therefore, potassium diffuses out of the cell at a much faster rate than sodium leaks in. Because more cations are leaving the cell than are entering, this causes the interior of the cell to be negatively charged relative to the outside of the cell. The actions of the sodium-potassium pump help to maintain the resting potential, once established. Recall that sodium-potassium pumps bring two K^+ ions into the cell while removing three Na^+ ions per ATP consumed.

b)Action potential

When we talk about neurons "firing" or being "active", we are talking about the action potential: a brief, positive change in the membrane potential along a neuron's axon. When an action potential occurs, the neuron sends the signal to the next neuron in the communication chain, and, if an action potential also occurs in the next neuron, then the signal will continue being transmitted. When a neuron receives a signal from another neuron, the signal causes a change in the membrane potential on the receiving neuron.

The signal causes the opening or closing of voltage-gated ion channels, channels that open or close in response to changes in the membrane voltage. The opening of voltage-gated ion channels causes the membrane to undergo either a hyperpolarization, where the membrane potential increases in magnitude (becomes more negative), or a depolarization, where the membrane potential decreases in magnitude (becomes more positive). Whether the membrane undergoes a hyperpolarization or a depolarization depends on the type of voltage-gated ion channel that opened.

Not all depolarizations result in an action potential. The signal must cause a depolarization that is large enough in magnitude to overcome the threshold potential or the specific voltage that the membrane must reach for an action potential to occur. The threshold potential is usually about -55 mV, compared to the resting potential of about -70 mV. If the threshold potential is reached, then an action potential is initiated at the axon hillock in the following stages:

– **Depolarization.**

Voltage-gated sodium channels open quickly after depolarization past the threshold potential. As sodium rushes into the axon (influx), the inside becomes relatively electrically positive (approximately $+30$ mV, compared to the initial resting potential of approximately -70 mV).

– **Repolarization**

Shortly after the initial depolarization, the voltage-gated sodium channels close and remain closed (and cannot be opened) for about $1-2$ ms. Voltage-gated potassium channels then open, allowing potassium to rush out of the axon (efflux), causing the membrane to repolarize (become more negative).

– **Hyperpolarizaton**

Potassium continues leaving the axon to the point that the membrane potential dips below the normal resting potential. Sodium channels return to their resting state, meaning they are ready to open again if the membrane potential again exceeds the threshold potential.

– **Reset resting potential**

The sodium-potassium pump and potassium leak channels reset the locations of sodium and potassium ions, reestablishing the membrane potential to allow another action potential to fire.

Action potentials always proceed in one direction only, from the cell body (soma) to the synapse(s) at the end of the axon. Action potentials never go backward, due to the refractory period of the voltage-gated ion channels, where the channels cannot re-open for a period of $1-2$ ms after they have closed. The refractory period forces the action potential to travel only in

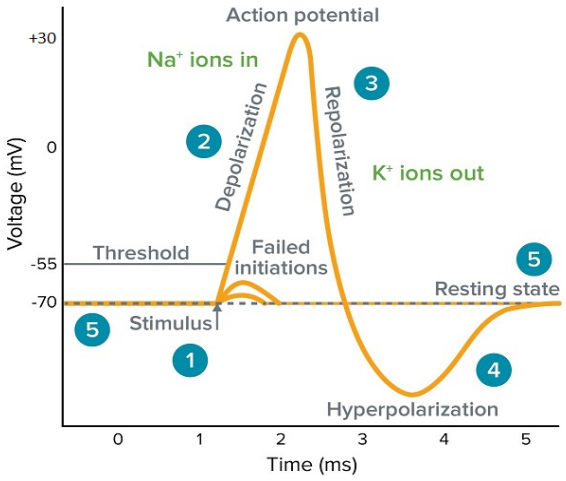

Figure 1.7: Formation of an action potential [134].

one direction. Action potentials do not vary in magnitude or speed; they are "all-or-nothing".

When a given neuron fires, the action potential always depolarizes to the same magnitude and always travels at the same speed along the axon. There is no such thing as a bigger or faster action potential. The parameter that can vary is the frequency of action potentials, or how many action potentials occur in a given amount of time. Action potentials travel down the axon by jumping from one node to the next. This jumping is called saltatory conduction. The image above shows a trace of an action potential at a single point in the membrane of an axon; the same pattern repeats down the entire length of the axon until it reaches the synapse.

c)Synaptic transmission

The synapse or "gap" is the place where information is transmitted from one neuron to another. Synapses usually form between axon terminals and dendritic spines, but this is not universally true. There are also axon-to-axon, dendrite-to-dendrite, and axon-to-cell body synapses. The neuron transmitting the signal is called the presynaptic neuron, and the neuron receiving the signal is called the postsynaptic neuron. Note that these designations are relative to a particular synapse. Most neurons are both presynaptic and postsynaptic. The synaptic connection between neurons and skeletal muscle cells is generally called neuromuscular Junction, and the connections between neurons and smooth muscle or glands are known as neuroreffector junctions. Action potentials can trigger both chemical and electrical synapses.

– Chemical synapses

In a chemical synapse, action potentials affect other neurons via a gap between neurons called a synapse. Synapses consist of a presynaptic ending, a synaptic cleft, and a postsynaptic ending. Presynaptic cells are ending axon of one neuron, postsynaptic cells are dendrites and cell

body of another cell and synaptic cleft which is the tiny gap between the pre-and postsynaptic cell as shown in Figure 1.8.

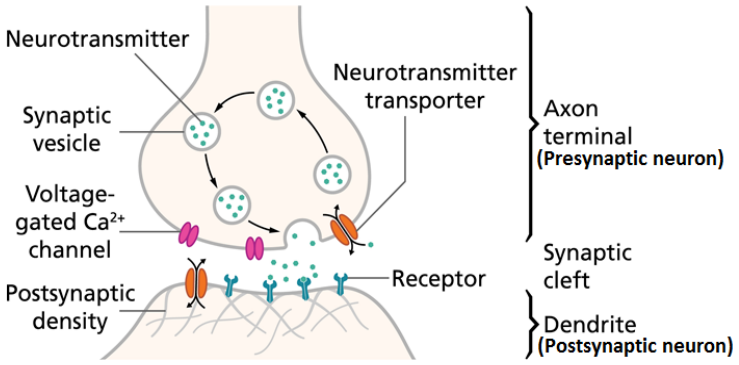

Figure 1.8: Schematic drawing of a synapse between two neurons [134].

When an action potential is generated, it is carried along the axon to a presynaptic ending. This triggers the release of chemical messengers called neurotransmitters. These molecules cross the synaptic cleft and bind to receptors in the postsynaptic ending of a dendrite. Synaptic between neurons are either excitatory or inhibitory. It means that Neurotransmitters can excite the postsynaptic neuron, causing it to generate an action potential of its own. Alternatively, they can inhibit the postsynaptic neuron, in which case it doesn't generate an action potential.

−Electrical synapses

Electrical synapses can only excite. They occur when two neurons are connected via a gap junction. This gap is much smaller than a synapse and includes ion channels that facilitate the direct transmission of a positive electrical signal. As a result, electrical synapses are much faster than chemical synapses. However, the signal diminishes from one neuron to the next, making them less effective at transmitting.

1.3.2 Fitzhugh-Nagumo model

The Fitzhugh-Nagumo (FN) model is a mathematical model of neuronal excitability developed by Richard FitzHugh in 1961 as a reduction of the Hodgkin and Huxley(HH) model of action potential generation in the squid giant axon [135]. In 1962, Nagumo et al. subsequently designed, implemented, and analyzed an equivalent electric circuit [136]. In its basic form, the model consists of two coupled, nonlinear ordinary differential equations, one of which describes the fast evolution of the neuronal membrane voltage, the other representing the slower recovery

action of sodium channel deactivation and potassium channel deactivation.

$$\begin{cases} \dot{v} = \alpha \left[f(v) - w + I(t) \right] \\ \dot{w} = \beta \left[g(v) - w \right] \end{cases} \tag{1.3}$$

where v is the membrane potential and w is the flow of ions through the membrane. $I(t)$ is the stimulation current. α and β are positive constants, f is a cubic function of v whereas g is a linear function of v. There are three types of behavior well reproduced by this model: resting potential, spiking, and bursting behaviors [137, 138].

1.3.3 Dynamical behavior

The Fitzhugh-Nagumo (FN) model is commonly used in neuroscience, chemistry, physics, and other disciplines as simple models of excitable dynamics, relaxation oscillations, and reaction-diffusion wave propagation. Various dynamics behaviors based on the FN model have been investigated. In order to reproduce the spiking and bursting behavior of real neurons, Zhilong et al. [139] established and analyzed a new hybrid biological neuron model by combining the FN neuron model, the threshold for spike initiation, and the state-dependent impulsive effects. They obtained some sufficient criteria for the existence and stability of order 1 or order 2 periodic solution to the impulsive neuron. The presented bifurcation diagrams describe the phenomena of a period-doubling route to chaos which implies that the dynamic behavior of the neuron model becomes more complex due to impulsive effects. Anderson Hoff et al. [140] studied numerically the dynamical behavior of two coupled FN oscillators. By the bifurcation curves and Lyapunov diagrams, they show that the system presents multistability in the planes of the basin of attractions. Muhammad et al. [141] studied the synchronization of two FN systems coupled with gap junctions. They found that synchronization is achieved by stabilizing the error dynamics. Moreover, another study on the phenomenon of vibrational multiresonance in a delayed FN system that is excited by two-frequency periodic signals is investigated. They found that time delay feedback induced in the system the quasi-periodic and periodic vibrational resonances, and also the firing pattern of the neuron can be regulated by modulating the delay parameter [142]. Finally, Valenti et al. analyzed the dynamics of a FN system subjected to autocorrelated noise. They investigated the role of the colored noise on the neuron dynamics by finding that, strongly correlated noise, efficiency enhance the neuronal response [143].

1.3.4 Discrete transmission lines mode of Fitzhugh-Nagumo model

The modeling of these nerve fibers has been subjected by the pioneering works of Hodgkin and Huxley [144] who have modeled the dynamics of the nervous impulse by a complex system of nonlinear partial differential equations. Inspired by this work, a chain of electrical circuits of FN has been taken into account where the diffusion term has been added as a means of propagation of signals in nerve fibers. And this has allowed to obtain FN partial differential equations model [145–148]. However, electrically, nerve fibers behave as spatially discrete periodic structures. This is due to the periodically spaced active channels (nodes of Ranvier) in the myelin insulation [149]. Thus, when studying the propagation of electrical signals through nerve fibers, it turns out to be more natural to study the discrete system instead of its continuous counterpart. Most researchers have made the investigations on FN model as a discrete transmission line, such as Irmantas and Pyragas [150] who have investigated the effect of a homogeneous high-frequency stimulation on a one-dimensional chain of coupled excitable elements governed by the FN equations. They showed that depending on the amplitude of high-frequency stimulation, the high-frequency stimulation can either enhance or suppress pulse propagation. [151, 152] investigated a discrete chain of coupled bistable reaction-diffusion modeled by the Nagumo equations. They determined propagation front initial conditions. They also obtained the critical coupling constant above which propagation is possible and determined the propagation speed. Furthermore, some authors [153] studied the effect of random long-range connections on signal propagation in an array of coupled FN neurons. They showed that when the first neuron is subjected to external stimuli, it fires and excites its connected neighbors, such that the neural signal may propagate along the chain favored by the shortcuts. Also, that disorder in the neural network may play a vital role in helping information processing in living systems.

1.4 PROBLEM STATEMENT OF THE THESIS

The study of multi-legged locomotion has increased exponentially in recent years. This concept of legged locomotion relating the biological and engineered system offers potential solutions to unsolved problems in daily life. Numerous studies have been carried out and have shown the advantages of the use of many legs. The legged locomotion is quite rich due to the variety of morphologies, gaits, and body sizes and due to the complexity of the environment where these multi-legged characters move: overcoming objects, crossing uneven terrain via coordination of their numerous legs, avoiding moving obstacles [154]. This allowed the development of a multi-legged robot that enables one to traverse rough terrain where

wheeled mobile robots cannot move around; eg. higher bumps, trenches, deep ruts, and so on [155].

For assembly line work, networks of electromechanical systems are increasingly recommended in the industry. In addition, to optimize their operation, it is advisable to supply such networks with electrical devices that allow impulse responses of the electromechanical systems. In addition to being used as the transmission lines, such systems can be used to mimic the movement of animals with multiple legs (centipedes and millipedes) [18]. Also, most of the work presented up to date in coupling between biological neuron and electromechanical system have been mainly theoretical [18, 34, 54, 54, 156] with some numerical verifications. According to these reasons our study is based on the dynamics of electromechanical devices powered by nonlinear electrical transmission lines.

Conclusion

In this chapter, we have presented some generalities on networks of electromechanical systems. Information on discrete Josephson junction transmission lines as well as on Fitzhugh-Nagumo are also given. This has enabled us to state the problem solved in this thesis.

Chapter 2

METHODOLOGY AND MATERIALS

Introduction

In this chapter, the physical descriptions of all the systems analyzed in this thesis are presented. Their corresponding mathematical models are then derived. The analytical and numerical methods used to analyze the differential equations found in the thesis are explained here. The experimental methods to analyze electrical circuits are also provided and finally, all the materials and components used during our experimental investigations are presented.

2.1 NANOELECTROMECHANICAL BEAM DRIVEN BY A SINGLE JOSEPHSON JUNCTION

2.1.1 Description of the system

The circuit diagram of the Josephson junction model coupled magnetically to a nanobeam is shown in Figure 2.1.

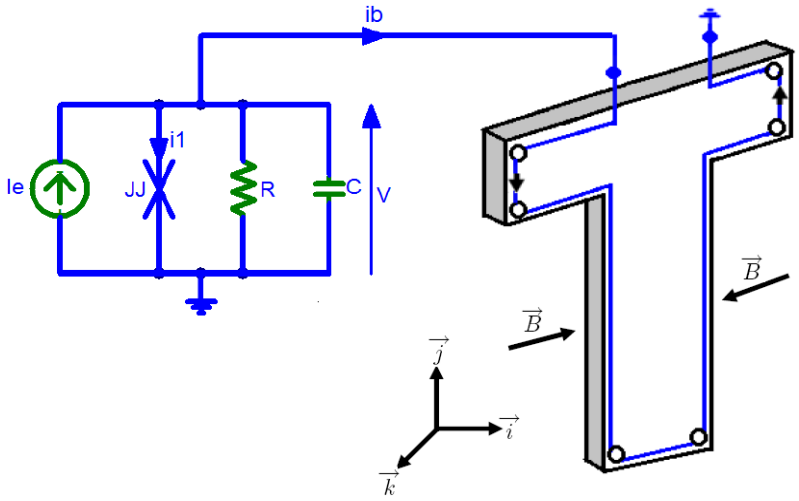

Figure 2.1: A single Josephson junction circuit coupled to a nanoelectromechanical beam and its corresponding symbol.

It is made of an electrical part which is constituted by a Josephson junction circuit model whose components are respectively: JJ denotes the Josephson junction element, C the junction capacitance and R the junction resistance. I_e is an external current source necessary to bias the junction. The mechanical part is made of a nano-beam (parallel to $\overrightarrow{k}$) on which is placed a winding and the whole is in magnetic field $\overrightarrow{B}$ (parallel to $\overrightarrow{i}$).

2.1.2 Mathematical model of a nanoelectromechanical beam driven by a single josephson junction

Let V be the voltage across the Josephson junction and i_1 the current through the junction. The relations between V, the phase difference ϕ across the Josephson barrier and i_1 are given as [157]:

$$V = \frac{\hbar}{2e}\frac{d\phi}{d\tau}, \tag{2.1}$$

$$i_1 = I_c \sin(\phi), \tag{2.2}$$

where e is the electron charge, $\hbar$ denotes the reduced Plank's constant and I_c is the critical current of the junction. The application of the Kirchhoff laws leads to the following differential equations:

$$C\frac{dV}{d\tau} + \frac{V}{R} + i_1 + i_b = I_e, \tag{2.3}$$

$$L\frac{di_b}{d\tau} + ri_b = V + e_f. \tag{2.4}$$

In equation (2.4), i_b is the current flowing through the winding located on the surface of the nano-beam. L and r are respectively the inductance and resistance of the winding and e_f is the induced electromotive voltage provided by the winding moving in the magnetic field, τ is the time. To obtain the equation of the nano-beam, let U be the deflection of nano-beam and ℓ the length of the wire loop located on the surface of the nano-beam. If we assume the nano-beam to be isotropic, uniform and flexible, then equation (2.5) is the transversal vibration of the Euler-Bernoulli beam [158, 159]:

$$\rho S\frac{\partial^2 U}{\partial \tau^2} + \lambda\frac{\partial U}{\partial \tau} + EI\frac{\partial^4 U}{\partial Z^4} = F_L\ , \tag{2.5}$$

where S is the cross-sectional area of the beam, ρ, λ, E, I and F_L are respectively the density, damping coefficient, Young's modulus, the second moment of area and the Laplace force. We have considered a thin beam and we neglect the axial and torsional vibrations compared to

the flexible vibrations. The induced electromotive voltage and the Laplace force acting on the whole nano-beam due to the magnetic coupling are given as:

$$e_f = -B\ell\frac{\partial U}{\partial \tau}, \tag{2.6}$$

$$F_L = B\ell i_b. \tag{2.7}$$

Introducing equations (2.1), (2.2) and (2.6) into equations (2.3) and (2.4), and equation (2.7) into equation (2.5), it comes that the system is described by the following three coupled differential equations:

$$\frac{C\hbar}{2e}\frac{d^2\phi}{d\tau^2} + \frac{\hbar}{2eR}\frac{d\phi}{d\tau} + I_c\sin\phi + i_b = I_e, \tag{2.8}$$

$$L\frac{di_b}{d\tau} + ri_b - \frac{\hbar}{2e}\frac{d\phi}{d\tau} + B\ell\frac{dU}{d\tau} = 0, \tag{2.9}$$

$$\rho S\frac{\partial^2 U}{\partial \tau^2} + \lambda\frac{\partial U}{\partial \tau} + EI\frac{\partial^4 U}{\partial Z^4} - B\ell i_b = 0. \tag{2.10}$$

For the cantilever beam, the following boundary conditions are added to the equation (2.10):

i) the fixed end ($Z = 0$) must have zero displacement and zero slope because of the clamp:

$$U(0,\tau) = 0 \text{ and } \frac{\partial U(0,\tau)}{\partial Z} = 0, \tag{2.11}$$

ii) the free end ($Z = L_1$) cannot have a shearing force nor a bending moment:

$$\frac{\partial^2 U(L_1,\tau)}{\partial Z^2} = 0 \text{ and } \frac{\partial^3 U(L_1,\tau)}{\partial Z^3} = 0. \tag{2.12}$$

L_1 represents the length of the nano-beam. One now introduce a set of dimensionless variables u, x and z. We normalize the variables as $u = \dfrac{U}{L_1}$, $x = \dfrac{i_b}{I_c}$ and $z = \dfrac{Z}{L_1}$. The time τ is normalized as $t = \omega_c\tau$, where ω_c is the characteristic radian frequency of the Junction. The set of equations (2.8) to (2.10) can then be rewritten in the following dimensionless form:

$$\beta_c\frac{d^2\phi}{dt^2} + \frac{d\phi}{dt} + \sin\phi + x = i_e, \tag{2.13}$$

$$\frac{dx}{dt} + \mu x - \eta\frac{d\phi}{dt} + \varepsilon_1\frac{\partial u}{\partial t} = 0, \tag{2.14}$$

$$\frac{\partial^2 u}{\partial t^2} + \alpha\frac{\partial u}{\partial t} + \omega_1^2\frac{\partial^4 u}{\partial z^4} = \gamma_1 x. \tag{2.15}$$

With the new introduced parameters defined as

$$\begin{aligned} &\omega_c = \frac{2eRI_c}{\hbar},\ \beta_c = \frac{2eI_cR^2C}{\hbar},\ i_e = \frac{I_e}{I_c},\ \mu = \frac{r}{L\omega_c},\ \eta = \frac{\hbar}{2eLI_c},\ \varepsilon_1 = \frac{B\ell L_1}{LI_c},\\ &\alpha = \frac{\lambda}{\rho S\omega_c},\ \omega_1 = \frac{1}{L_1^2\omega_c}\sqrt{\frac{EI}{\rho S}} \quad \text{and} \quad \gamma_1 = \frac{B\ell I_c}{\rho S L_1\omega_c^2}. \end{aligned} \tag{2.16}$$

β_c represents the Stewart-McCumber parameter. The dimensionless of boundary conditions become

$$u\left(0,t\right)=0 \text{ and } \frac{\partial u\left(0,t\right)}{\partial z}=0, \tag{2.17}$$

$$\frac{\partial^2 u\left(1,t\right)}{\partial z^2}=0 \text{ and } \frac{\partial^2 u\left(1,t\right)}{\partial z^3}=0. \tag{2.18}$$

Equation (2.15) is a partial differential equation. In order to obtain an equivalent ordinary differential equation, on use the Galerkin's method to have the modal equation [158]. For that purpose, the deflection of the nano-beam can be written as:

$$u\left(z,t\right)=\sum_{p=1}^{\infty}\varphi_p\left(z\right)y_p\left(t\right). \tag{2.19}$$

where $y_p\left(t\right)$ is the function of time at p^{th} mode and $\varphi_p\left(z\right)$ is the spatial function. Resolving equation (2.15) without damping force and Laplace force and also taking into account of the boundary condition, the spatial function $\varphi_p\left(z\right)$ is given by:

$$\varphi_{\mathrm{p}}\left(z\right)=\frac{\sin\left(K_p\right)+\sinh\left(K_p\right)}{\cos\left(K_p\right)+\cosh\left(K_p\right)}\left[\cosh\left(K_pz\right)-\cos\left(K_pz\right)\right]+\left[\sin\left(K_pz\right)-\sinh\left(K_pz\right)\right]. \tag{2.20}$$

Substituting equation (2.20) into equation (2.19) which is then multiplied by $\varphi_m(z)$ and integrating from 0 to 1 for the first mode of vibration, see below.

$$\int_0^1\varphi_m\varphi_p dz=1,\quad \int_0^1\varphi_m(z)dz=c_1\quad\text{and}\quad \int_0^1\varphi_m(z)\frac{\partial^4\varphi_p}{\partial z^4}dz=c_2. \tag{2.21}$$

After some mathematical manipulations, one obtains $K_p=1.8751$, where K_p is the solution of the equation $\cos K_p\cosh K_p=-1$, $c_1=1.066$ and $c_2=22.939$. As consequence, the set of equations (2.13) to (2.15) is reduced to the following system of three ordinary differential equations where the third equation is the modal equation of nano-beam with y the displacement of the nanoelectromechanical beam at the first mode.

$$\begin{cases}\beta_c\ddot{\phi}+\dot{\phi}+\sin\phi+x=i_e,\\ \dot{x}+\mu x-\eta\dot{\phi}+\varepsilon\dot{y}=0,\\ \ddot{y}+\alpha\dot{y}+\omega^2y-\gamma x=0,\end{cases} \tag{2.22}$$

where $\omega=\omega_1\sqrt{c_2}$, $\gamma=c_1\gamma_1$ and $\varepsilon=\dfrac{\varepsilon_1}{c_1}$. The set of equations (2.22) can be transformed to five

first order differential equations convenient for numerical simulation as follows:

$$\begin{cases} \dot{\phi} = v, \\ \dot{v} = -\dfrac{1}{\beta_c}\left(v + \sin\phi + x - i_e\right), \\ \dot{x} = \eta v - \mu x - \varepsilon z, \\ \dot{y} = z, \\ \dot{z} = \gamma x - \omega^2 y - \alpha z. \end{cases} \tag{2.23}$$

2.2 ELECTROMECHANICAL ARM POWERED BY A FITZHUGH-NAGUMO NEURON

2.2.1 Physical description of the system

We consider an equivalent circuit of Fitzhugh-Nagumo neuron coupled magnetically to a mechanical arm, as shown in Figure 2.2.

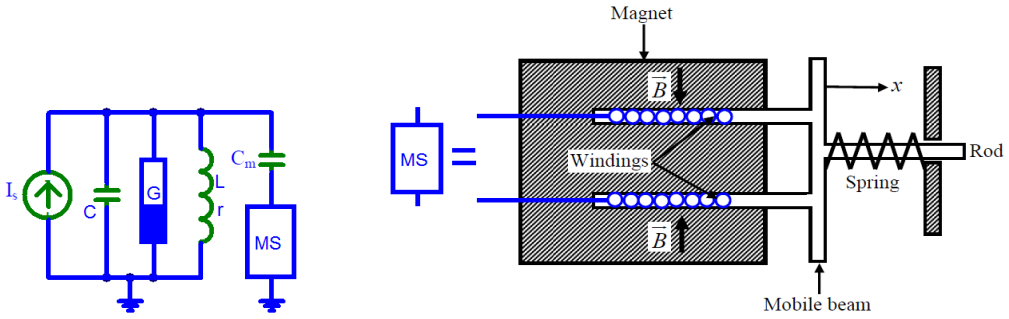

a) b)

Figure 2.2: a) Equivalent circuit of Fitzhugh-Nagumo neuron coupled to an electromechanical arm. b) Internal structure of the electromechanical subsystem.

In the equivalent circuit of Figure 2.2a), I_s represents the external electrical stimulation current source, C is the membrane capacitance, G is the membrane conductance, L and r represent respectively the inductance and resistance of the membrane. The block MS represents our mechanical arm and its internal structure is shown in Figure 2.2b).

The coil is positioned in the air gap of the magnet and a beam is rigidly attached to the coil. Besides, one spring is added to avoid the movement of the mobile beam away from the balanced position established when the system was assembled. The interaction of the current through the windings and the magnetic field produces mechanical vibrations of the mobile beam. The

coupling between both parts is realized through the electromagnetic force due to a permanent magnet which creates a Laplace force in the mechanical part and the Lenz electromotive voltage in the electrical part.

Two different strategies are responsible for electrical communication between neurons. One is the consequence of low resistance intercellular pathways, called "gap junctions". The second occurs in the absence of cell-to-cell contacts and is a consequence of the extracellular electrical fields generated by the electrical activity of neurons. In the same manner, the capacitance C_m is used to realize the coupling between the neuron and the electromechanical system.

2.2.2 Mathematical model of the system

In this model, the conductance G is the only nonlinear element, and its voltage-current characteristics is given in equation (2.24):

$$i_G = \alpha v \left(v - \mu_1\right)\left(v - \mu_2\right), \tag{2.24}$$

where i_G and v are the current through and voltage across the conductance respectively. μ_1 and μ_2 are respectively the threshold voltage and the diffusion potential of the neuron. Finally, α is a fitting parameter and is a function of the potentials of different ions present in the neuron. The Fitzhugh-Nagumo model of nonlinear conductance shown in equation (2.24) can be simulated by a different nonlinear electric circuit, using a tunnel diode or a nonlinear resistor with a smooth cubic $v - i$ characteristic.

The application of the Kirchhoff laws to the circuit shown in Figure 2.2a) leads to the following differential equations:

$$C\frac{dv}{dt} + i + i_m + \alpha v \left(v - \mu_1\right)\left(v - \mu_2\right) = I_s, \tag{2.25}$$

$$L\frac{di}{dt} + ri = v, \tag{2.26}$$

$$L_m\frac{di_m}{dt} + r_m i_m + u - v = -B\ell\frac{dx}{dt}, \tag{2.27}$$

$$C_m\frac{du}{dt} = i_m. \tag{2.28}$$

L_m and r_m are respectively the inductance and resistance of the windings, v represents the membrane potential of the cell, namely the voltage across the membrane capacitance C, i is the current through the inductance L, and represents biologically the recovery variable related to the inactivation of the sodium channels. i_m is the current flowing through the winding, u is the voltage across the capacitance C_m and represents the electrical synaptic potential or coupling potential, and t is the time.

Since there is no contact between the magnet and the moving windings, the friction effects are neglected here. The mechanical subsystem used in this work has been modeled mathematically by many authors [160–162] and the experimental verification of the theoretical results has been made using a motion detector and an accelerometer [40, 41]. During their experimental works, Kitio et al. found excellent agreement between the experimental and theoretical results when the friction forces are not taken into account [40, 41]. The equation of motion of the mobile beam of mass m is given by:

$$m\frac{d^2x}{dt^2} + \beta_0\frac{dx}{dt} + Kx = B\ell i_m, \tag{2.29}$$

where β_0 is the damping coefficient, and K is the spring constant. ℓ is the total length of the conductor used in the winding. The term $-B\ell\dfrac{dx}{dt}$ represents the induced voltage in the winding, while the term $B\ell i_m$ represents the Laplace force acting on the conducting wire in the magnetic field. Equation (2.29) is valid for displacements of small amplitudes in the mechanical subsystem. In case of high magnitude displacements, it is necessary to take into account the nonlinear response of the spring [160, 161].

Introducing the news variables and the following dimensionless parameters:

$$\begin{aligned} &i = w,\ i_m = z,\ \tau = \omega_0 t,\ a = \frac{1}{C\omega_0},\ b = \frac{1}{L\omega_0},\ d = \frac{1}{L_m\omega_0},\ \gamma = B\ell\omega_0,\ \beta = \frac{\beta_0}{m\omega_0},\\ &\varepsilon = \frac{K}{m\omega_0^2},\ \sigma = \frac{B\ell}{m\omega_0^2},\ \text{and } q = \frac{1}{C_m\omega_0}, \end{aligned} \tag{2.30}$$

we obtain that the dimensionless equations governing the dynamics of the whole system are thus:

$$\begin{cases} \dot{v} = a\left(I_s - w - z - \alpha v\left(v - \mu_1\right)\left(v - \mu_2\right)\right), \\ \dot{w} = b\left(v - rw\right), \\ \ddot{x} = -\beta\dot{x} - \varepsilon x + \sigma z, \\ \dot{z} = d\left(v - u - r_m z - \gamma\dot{x}\right), \\ \dot{u} = qz. \end{cases} \tag{2.31}$$

The action of the electrical subsystem on the electromechanical part is visualized through the parameter σ while the effect of the electromechanical system in the electrical block is measured through the product $d\gamma$. If $\sigma \gg d\gamma$, the electrical subsystem is viewed as a voltage source by the mechanical part. In contrast, if $\sigma \ll d\gamma$, the power provided by the electrical part will be less than the power required by the mechanical part. The moderated values of σ and $d\gamma$ are then required for the subsystems to influence each other.

2.3 MATHEMATICAL MODEL OF ARRAY OF ELECTROMECHANICAL SYSTEMS

2.3.1 Array of nanoelectromechanical beams driven by a discrete array of Josephson junctions

In this subsection, we analyze the behavior of a system consisting of nano-beams fixed at each node of a discrete line of coupled Josephson junctions. The coupling between two neighborhood elements is made by an inductance L_c as illustrated in Figure 2.3.

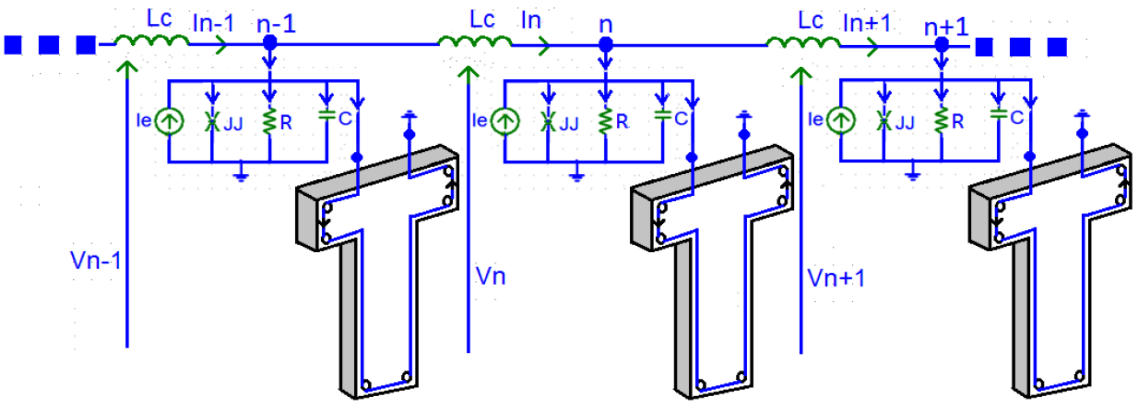

Figure 2.3: Schematic representation of the array of Josephson junctions circuit coupled to nanoelectromechanical beams.

Let ϕ_n, V_n, i_{bn}, and U_n be respectively the phase, the junction voltage, the current through the winding and the deflection of the n^{th} nano-beam. Using the Kirchhoff's laws, the circuit equations for the line are given by:

$$\begin{cases} \dfrac{C\hbar}{2e}\dfrac{d^2\phi_n}{d\tau^2} + \dfrac{\hbar}{2eR}\dfrac{d\phi_n}{d\tau} + I_c\sin\phi_n + i_{bn} = I_e + \dfrac{\hbar}{2eL_c}\left(\phi_{n+1} - 2\phi_n + \phi_{n-1}\right), \\ L\dfrac{di_{bn}}{d\tau} = \dfrac{\hbar}{2e}\dfrac{d\phi_n}{d\tau} - ri_{bn} - B\ell\dfrac{\partial U_n}{\partial\tau}, \\ \rho S\dfrac{\partial^2 U_n}{\partial\tau^2} + \lambda\dfrac{\partial U_n}{\partial\tau} + EI\dfrac{\partial^4 U_n}{\partial Z_n^4} = B\ell i_{bn}. \end{cases} \tag{2.32}$$

Using the dimensionless parameters and the Galerkin transformations presented in above section, it is found that the line circuit is described by the following system of coupled ordinary differential equations:

$$\begin{cases} \beta_c\ddot{\phi}_n + \dot{\phi}_n + \sin\phi_n + x_n = i_e + k\left(\phi_{n+1} - 2\phi_n + \phi_{n-1}\right), \\ \dot{x}_n + \mu x_n - \eta\dot{\phi}_n + \varepsilon\dot{y}_n = 0, \\ \ddot{y}_n + \alpha\dot{y}_n + \omega^2 y_n - \gamma x_n = 0. \end{cases} \tag{2.33}$$

This is the set of differential equations describing the propagation of electrical signal and the motion of N nano-beams. In this set of equations, the coupling parameter k between neighboring nodes is defined as $k = \sqrt{\frac{\hbar}{2eL_cI_c}}$. The other parameters are defined as in equation (2.34).

$$\begin{aligned} &\omega_c = \frac{2eRI_c}{\hbar},\ \beta_c = \frac{2eI_cR^2C}{\hbar},\ i_e = \frac{I_e}{I_c},\ \mu = \frac{r}{L\omega_c},\ \eta = \frac{\hbar}{2eLI_c},\ \varepsilon_1 = \frac{B\ell L_1}{LI_c}, \\ &\alpha = \frac{\lambda}{\rho S\omega_c},\ \omega_1 = \frac{1}{L_1^2\omega_c}\sqrt{\frac{EI}{\rho S}} \quad \text{and} \quad \gamma_1 = \frac{B\ell I_c}{\rho S L_1\omega_c^2}. \end{aligned} \tag{2.34}$$

2.3.2 Array of electromechanical arms powered by an array of Fitzhugh Nagumo neurons

The other goal of this subsection is to analyze the behavior of a system consisting of an electromechanical system fixed at each node of a discrete line of coupled Fitzhugh-Nagumo type oscillator. The coupling between two neighborhood elements is made by a resistance R_c as illustrated in Figure 2.4.

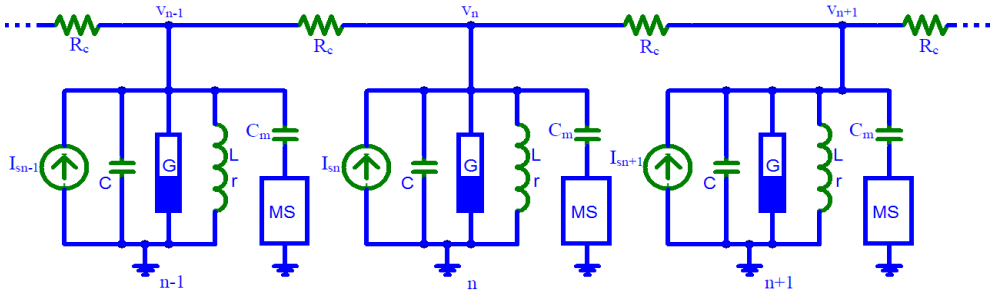

Figure 2.4: Schematic representation of the array of Fitzhugh Nagumo coupled to electromechanical arms.

As mentioned previously, the block MS represents the electromechanical system. R_c is an intercellular resistance that represents the coupling resistance between the cells. $n = 1, 2, \cdots, N$, where $N = 6000$ is the total number of cells. Let v_n and u_n be respectively the voltages drop across the capacitances C and C_m in the n$^{\text{th}}$ cell. Still in the n$^{\text{th}}$ cell, i_n and i_{m_n} are respectively the currents through the inductances L and L_m and x_n is the mechanical displacement of the mobile beam. The application of the Kirchhoff's and Newton laws to the complete system leads

to the following differential equations:

$$\begin{cases} C\dfrac{dv_n}{dt} + i_n + i_{m_n} + \alpha v_n\left(v_n - \mu_1\right)\left(v_n - \mu_2\right) - \dfrac{1}{R_c}\left(v_{n+1} - 2v_n + v_{n-1}\right) = I_{s_n}, \\ L\dfrac{di_n}{dt} + ri_n = v_n, \\ L_m\dfrac{di_{m_n}}{dt} + r_m i_{m_n} + u_n - v_n + B\ell\dfrac{dx_n}{dt} = 0, \\ m\dfrac{d^2x_n}{dt^2} + \lambda\dfrac{dx_n}{dt} + Kx_n = B\ell i_{m_n}, \\ C_m\dfrac{du_n}{dt} = i_{m_n}. \end{cases} \tag{2.35}$$

We will proceed as we have done in the previous section. Then, considering the dimensionless variables introduced in the previous section: v_n, w_n, z_n, u_n and x_n, the overall system is described by the following nonlinear ordinary differential equations:

$$\begin{cases} \dot{v}_n = a\left(I_{s_n} - \alpha v_n\left(v_n - \mu_1\right)\left(v_n - \mu_2\right) - w_n - z_n + \dfrac{1}{R_c}\left(v_{n+1} - 2v_n + v_{n-1}\right)\right), \\ \dot{w}_n = b\left(v_n - rw_n\right), \\ \dot{z}_n = d\left(v_n - u_n - r_m z_n - \gamma\dot{x}_n\right), \\ \ddot{x}_n = -\beta\dot{x}_n - \varepsilon x_n + \sigma z_n, \\ \dot{u}_n = qz_n. \end{cases} \quad \text{with } 1 \leqslant n \leqslant N \tag{2.36}$$

Let us first recall some interesting results when the mechanical part is not connected and the membrane inductance is neglected ($L = 0$ H) in the equivalent circuit. The coupling term in the first equation of system (2.36) can be approximated with partial derivatives with respect to distance, x', assuming that the spacing between two adjacent units is small. If we assume that the voltage v varies slowly from one unit section to the other, the discrete spatial coordinate n can be replaced by a continuous one x', the network is then described by the following diffusion equation:

$$\frac{1}{R_c}\frac{\partial^2 v}{\partial x'^2} + \frac{1}{a}\frac{\partial v}{\partial t'} - \frac{v}{r} - \alpha v\left(v - \mu_1\right)\left(v - \mu_2\right) = 0. \tag{2.37}$$

We start the analysis by looking for wave solutions of equation (2.37) in the form of $v\left(t', x'\right) = V\left(\xi\right)$ where $\xi = x' - V_0 t'$ is a traveling wave variable. This assumption of a traveling wave converts the partial differential equation (2.37) into the second order ordinary differential equation

$$\frac{1}{R_c}\frac{d^2V}{d\xi^2} - \frac{V_0}{a}\frac{dV}{d\xi} - \frac{V}{r} - \alpha V\left(V - \mu_1\right)\left(V - \mu_2\right) = 0. \tag{2.38}$$

In the above ordinary differential equation, the traveling wave speed V_0 is an unknown parameter that must be obtained by the analysis. The corresponding traveling wave solution and the traveling wave speed are given by

$$V(\xi) = \frac{\mu_1 + \mu_2 + A}{4} + \frac{\sqrt{2B}}{4} \tanh\left(\frac{\sqrt{\alpha R_c B}}{4}\xi\right) \text{ and } V_0 = \frac{a}{4}\sqrt{\frac{2\alpha}{R_c}}\left(\mu_1 + \mu_2 - 3A\right), \quad (2.39)$$

where the newly introduced parameters A and B are worth

$$A = -\sqrt{\left(\mu_1 + \mu_2\right)^2 - \frac{4}{\alpha r}} \text{ and } B = \mu_1^2 + \mu_2^2 + \left(\mu_1 + \mu_2\right) A - \frac{2}{\alpha r}. \quad (2.40)$$

Next, let us consider the influence of the recovery term in the system (2.36), where the inductance L and the mechanical part are included. There are no analytical expressions so far, and the results will be achieved in the following sections only through the computer simulations. Nevertheless, the expressions obtained in equations (2.39) and (2.40) can provide some ideas. Looking at an understanding of the underlying physical processes and possible technical applications, we additionally study the influence of circuit parameters on the signal waveform.

2.4 ANALYTICAL METHODS

The primary advantage of analytical methods is that they are very cost effective and they are also reasonably effective to analyze the behavior of dynamical systems. Analytical procedure as a substantive test reduces the time taken in determining the future course of action.

2.4.1 Routh-Hurwitz stability criterion

In control system theory, the Routh-Hurwitz stability criterion is a mathematical test that is a necessary and sufficient condition for the stability of a linear time invariant control system. The Routh test is an efficient recursive algorithm to determine whether all the roots of the characteristic polynomial of a linear system have negative real parts. Hurwitz independently proposed to arrange the coefficients of the polynomial into a square matrix, called the Hurwitz matrix, and showed that the polynomial is stable if and only if the sequence of determinants of its principal submatrices are all positive.

The two procedures are equivalent, with the Routh test providing a more efficient way to compute the Hurwitz determinants than computing them directly. A polynomial satisfying the Routh-Hurwitz criterion is called a Hurwitz polynomial. The importance of the criterion is that the roots s of the characteristic equation of a linear system with negative real parts

represent solutions e^{st} of the system that are stable (bounded). Thus the criterion provides a way to determine if the equations of motion of a linear system have only stable solutions, without solving the system directly.

A tabular method can be used to determine the stability when the roots of a higher order characteristic polynomial are difficult to obtain. For an n$^{\text{th}}$-degree polynomial

$$\mathrm{D}\,(\mathrm{s}) = a_n s^n + a_{n-1} s^{n-1} + \cdots + a_2 s^2 + a_1 s + a_0. \tag{2.41}$$

the table has $n+1$ rows and the following structure:

$$\begin{array}{ccccc} a_n & a_{n-2} & a_{n-4} & a_{n-6} & \cdots \\ a_{n-1} & a_{n-3} & a_{n-5} & a_{n-7} & \cdots \\ b_1 & b_2 & b_3 & b_4 & \cdots \\ c_1 & c_2 & c_3 & c_4 & \cdots \\ \vdots & \vdots & \vdots & \vdots & \ddots \end{array}. \tag{2.42}$$

where the elements b_i and c_i can be computed as follows:

$$b_i = \frac{a_{n-1}a_{n-2i} - a_n a_{n-(2i+1)}}{a_{n-1}} \quad \text{and} \quad c_i = \frac{b_1 a_{n-(2i+1)} - a_{n-1} b_{i+1}}{b_1}. \tag{2.43}$$

When completed, the number of sign changes in the first column will be the number of non-negative roots.

2.4.2 General oscillation startup condition

The Barkhausen criterion has been widely used to determine the oscillation startup condition. However, it is only partially correct [163]. The general oscillation condition and the oscillation frequency related to the general oscillation startup condition are presented in this subsection. Assume the characteristic polynomial of a certain system has the following form:

$$a_0 + a_1 s + a_2 s^2 + a_3 s^3 + a_4 s^4 + \cdots + a_n s^n = 0. \tag{2.44}$$

The corresponding system will oscillate if s is a purely imaginary number. Let $s = j\omega$ where $j^2 = -1$ and ω is the radian frequency of the system. Hence equation (2.44) is equivalent to

$$\begin{cases} a_0 - a_2\omega^2 + a_4\omega^4 + \cdots = 0, \\ a_1 - a_3\omega^2 + a_5\omega^4 + \cdots = 0. \end{cases} \tag{2.45}$$

The first equation of system (2.45) is often used to derive the oscillation start-up condition while the second equation of system (2.45) allows the determination of the oscillation frequency.

In practice, an oscillator needs exponentially increasing amplitude to get the oscillation start up. So the general oscillation condition of a feedback oscillator can be assumed as following: There is at least one root of (2.44) lying in the right half of the s plane or a double roots on the imaginary axe.

2.4.3 Cardano's Method

Cardano's method provides a technique for solving the general cubic equation:

$$ax^3 + bx^2 + cx + d = 0, \tag{2.46}$$

in terms of radicals, as with the quadratic equation, it involves a "discriminant" whose sign determines the number of real solutions. However, its implementation requires substantially more technique than does the quadratic formula. For example, in the "irreducible case" of three real solutions, it calls for the evaluation of the cube roots of complex numbers. In outline, Cardano's methods involves the following steps:
1) "Eliminate the square term" by the substitution $x = \dfrac{y-b}{3a}$. Rather than keeping track of such a substitution relative to the original cubic, the method often begins with an equation in the reduced form

$$y^3 - 3\lambda y + 2q = 0, \tag{2.47}$$

where $\lambda = b^2 - 3ac$ and $q = b^3 - \dfrac{9abc - 27a^2d}{2}$.
2) Letting $y = u + v$, rewrite the above equation as

$$u^3 + v^3 + 3(uv - \lambda)(u + v) + 2q = 0. \tag{2.48}$$

3) The above equation becomes the following system of equations:

$$\begin{cases} u^3 + v^3 = -2q, \\ u^3 v^3 = \lambda^3. \end{cases} \tag{2.49}$$

Since this system specifies both the sum and product of u^3 and v^3, it enables us to determine a quadratic equation whose roots are u^3 and v^3. This equation is

$$\left(u^3\right)^2 + 2qu^3 + \lambda^3 = 0 \text{ and } \left(v^3\right)^2 + 2qv^3 + \lambda^3 = 0, \tag{2.50}$$

The simplified discriminant of the equations (2.50) is given as

$$\Delta = q^2 - \lambda^3. \tag{2.51}$$

According to the sign of the discriminant Δ, we have the following cases:

– If $\Delta > 0$, equation (2.46) has one real solution given as

$$x = \frac{1}{3a}\left(-b + \sqrt[3]{-q - \sqrt{\Delta}} + \sqrt[3]{-q + \sqrt{\Delta}}\right). \tag{2.52}$$

– If $\Delta \leqslant 0$, equation (2.46) has three real solutions and in this case, we have to find the cube roots of complex numbers. After some mathematical transformations, the three real roots are given as

$$\begin{aligned} &x_1 = \frac{-b - 2\sqrt{\lambda}\cos\left(\frac{\theta-2\pi}{3}\right)}{3a},\ x_2 = \frac{-b - 2\sqrt{\lambda}\cos\left(\frac{\theta}{3}\right)}{3a},\ x_3 = \frac{-b - 2\sqrt{\lambda}\cos\left(\frac{\theta+2\pi}{3}\right)}{3a} \\ &\text{where} \quad \theta = \arctan\left(\frac{\sqrt{-\Delta}}{q}\right). \end{aligned} \tag{2.53}$$

2.5 SIMULATION METHODS

2.5.1 Fourth order Runge-Kutta method

This method was developed for the first time by the mathematician C. Runge in 1894 and improved by Mr. W. Kutta in 1901. Let us solve a system of three first-order differential equations given as follows:

$$\begin{cases} \dot{x} = g_1(x, y, z), \\ \dot{y} = g_2(x, y, z), \\ \dot{z} = g_3(x, y, z). \end{cases} \tag{2.54}$$

The Runge-Kutta method allows to find the variables x, y and z at successive time intervals $\Delta t = h$. The iterative scheme of the RK4 method is given by the following relationships:

$$\begin{cases} x_{n+1} = x_n + \dfrac{\ell_1 + 2(\ell_2 + \ell_3) + \ell_4}{6}, \\ y_{n+1} = y_n + \dfrac{k_1 + 2(k_2 + k_3) + k_4}{6} \\ z_{n+1} = z_n + \dfrac{p_1 + 2(p_2 + p_3) + p_4}{6} \end{cases} \quad \text{where } n = 0,\ 1,\ 2,\ 3,\ \cdots. \tag{2.55}$$

x_0, y_0 and z_0 are the known as the initial conditions. The Runge-Kutta coefficients ℓ_1, ℓ_2, ℓ_3,

ℓ_4, k_1, k_2, k_3, k_4, p_1, p_2, p_3 and p_4 are given as

$$\begin{aligned}
\ell_1 = hg_1(t,x,y,z),\ k_1 = hg_2(t,x,y,z),\ p_1 = hg_3(t,x,y,z),\\
\ell_2 = hg_1\left(t+\tfrac{h}{2}, x+\tfrac{\ell_1}{2}, y+\tfrac{k_1}{2}, z+\tfrac{p_1}{2}\right),\\
k_2 = hg_2\left(t+\tfrac{h}{2}, x+\tfrac{\ell_1}{2}, y+\tfrac{k_1}{2}, z+\tfrac{p_1}{2}\right),\\
p_2 = hg_3\left(t+\tfrac{h}{2}, x+\tfrac{\ell_1}{2}, y+\tfrac{k_1}{2}, z+\tfrac{p_1}{2}\right),\\
\ell_3 = hg_1\left(t+\tfrac{h}{2}, x+\tfrac{\ell_2}{2}, y+\tfrac{k_2}{2}, z+\tfrac{p_2}{2}\right),\\
k_3 = hg_2\left(t+\tfrac{h}{2}, x+\tfrac{\ell_2}{2}, y+\tfrac{k_2}{2}, z+\tfrac{p_2}{2}\right),\\
p_3 = hg_3\left(t+\tfrac{h}{2}, x+\tfrac{\ell_2}{2}, y+\tfrac{k_2}{2}, z+\tfrac{p_2}{2}\right),\\
\ell_4 = hg_1(t+h, x+\ell_3, y+k_3, z+p_3),\\
k_4 = hg_2(t+h, x+\ell_3, y+k_3, z+p_3) \text{ and}\\
p_4 = hg_3(t+h, x+\ell_3, y+k_3, z+p_3).
\end{aligned} \tag{2.56}$$

2.5.2 Finite difference methods

Finite difference methods(FDM) are well-known numerical methods to solve differential equations by approximating the derivatives using different difference schemes [164, 165]. Many science and engineering models involve nonlinear and nonhomogeneous differential equations, and solutions of these equations are sometimes beyond the reach of analytical methods. In such cases, FDM may be found to be practical, particularly for regular domains. To apply the difference method to find the solution of a function U(x), let us divide this interval $[AB]$ into equal division $\Delta x = h$ where h is the increment in step size. Consider $x_0 = a$, $x_{i+1} = x_i + h$ and $x_n = b$ with $i = 0, 1, 2, 3, 4, ...n-1$.

The approach used to obtain finite difference equations is Taylor's series:

$$U(x_0+h) = U(x_0) + hf^{'}(x_0) + \frac{1}{2!}h^2 f^{''}(x_0) + \frac{1}{3!}h^3 f^{'''}(x_0) + 0(h)^4 \tag{2.57}$$

$$U(x_0-h) = U(x_0) - hf^{'}(x_0) + \frac{1}{2!}h^2 f^{''}(x_0) - \frac{1}{3!}h^3 f^{'''}(x_0) + 0(h)^4 \tag{2.58}$$

Where $0(h^4)$ is the error introduced by truncating series. Using a forward difference formula for the first derivative of U at x and central difference formula for the second derivative at x, we get respectively

$$U_x = \frac{U_{i+1} - U_i}{h} \text{ and } U_{xx} = \frac{U_{i+1} - 2U_i + U_{i-1}}{h^2}, \tag{2.59}$$

2.6 EXPERIMENTAL METHODS

2.6.1 Operational amplifier

The operational amplifier is the essential component in the design of the inverter, adder and integrator circuits. We will use the operational amplifier of type LF356. These amplifiers feature low input bias and offset currents/low offset voltage and offset voltage drift, coupled with offset adjust, which does not degrade drift or common-mode rejection. The devices are also designed for high slew rate, wide bandwidth, extremely fast settling time, low voltage and current noise. The pin assignment, the physical symbol, and the actual appearance of the component are shown in Figure 2.5a), Figure 2.5b), and Figure 2.5c) respectively.

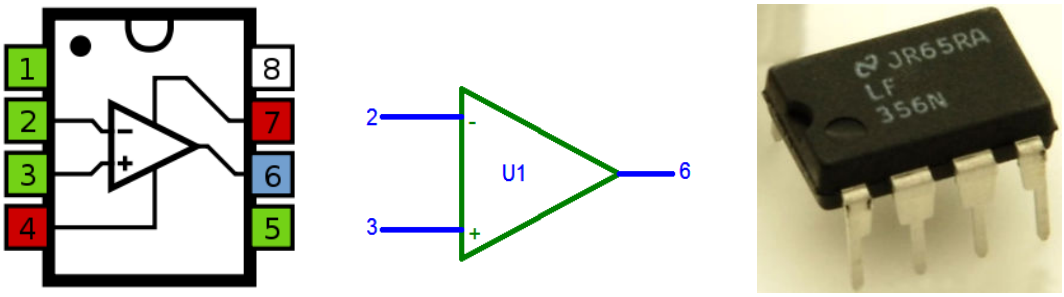

a) b) c)

Figure 2.5: Operational amplifier, a) Pin configuration, b) Physical symbol and c) Picture of the component.

In figures 2.5b), pins 1 and 5 are used for offset compensation. Pins 2 and 3 are the inverting and non-inverting inputs respectively, pins 4 and 7 are used for the negative and positive polarizations and pin 6 is the circuit output.

2.6.2 Integrator circuit

The diagram of one input integrator circuit is shown in Figures 2.6.

The application of the Kirchhoff laws to the above circuit gives the output voltage v_0 as a function of the input voltage v_{in}.

$$v_o = -\frac{1}{RC}\int v_{in}dt. \tag{2.60}$$

We have to notice that the integrator does not work so ideally. In fact, the low input current of the amplifier produces in the resistor R a voltage drop which is also integrated: the output becomes saturated because the capacitor remains charged. To obtain a satisfactory

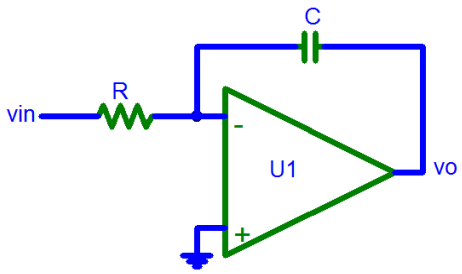

Figure 2.6: Integrator circuit.

integration, the time constant RC must be neither too weak to saturate the operational amplifier nor too large to distort the integration. In this work, we will use it to integrate the electrical signal(acceleration) delivered by the sensor in speed then in position.

2.6.3 Inverter and non inverting circuits

The inverter circuit is shown in Figure 2.7 where v_e and v_s are the input and output voltages respectively.

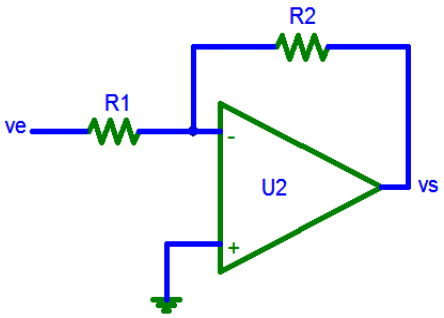

Figure 2.7: Inverter circuit.

The application of the Kirchhoff laws leads to the following relation:

$$v_s = -\frac{R_2}{R_1} v_e. \tag{2.61}$$

The negative sign in the equation indicates an inversion of the output signal with respect to the input as it is out of phase. This is due to the feedback being negative in value. The equation for the output voltage also shows that the circuit is linear in nature for a fixed amplifier gain.

A non-inverting amplifier shown in Figure 2.8 is an operational amplifier circuit configuration that produces an amplified output signal and this output signal of the non-inverting operational amplifier is in-phase with the applied input signal.

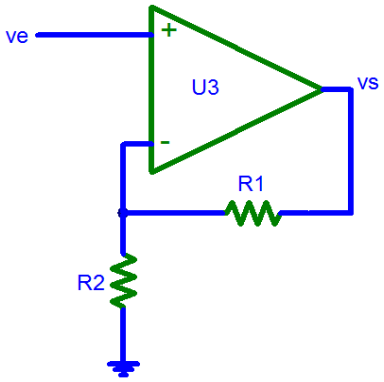

Figure 2.8: A non-inverting amplifier circuit.

A non-inverting amplifier also uses a negative feedback connection, but instead of feeding the entire output signal to the input, only a part of the output signal voltage is fed back as input to the inverting input terminal of the op-amp. The high input impedance and low output impedance of the non-inverting amplifier make the circuit ideal for impedance buffering applications. The application of the Kirchhoff laws to the circuit gives the output voltage as a function of the input voltage.

$$v_s = \left(1 + \frac{R_1}{R_2}\right) v_e. \tag{2.62}$$

When a positive-going input signal is applied to the non-inverting input terminal, the output voltage will shift to keep the inverting input terminal equal to that of the input voltage applied. Hence, there will be a feedback voltage developed across resistor R_2. In the design of our analogue device, we need it to understand first the operating principle of the inverting and non-inverting circuits.

2.6.4 Negative resistance

Strictly speaking, there are not true negative resistors exactly as there are not true energy sources since they will violate thermodynamics laws; there are only energy converters. Whereas positive resistors consume energy from circuits, the equivalent true negative resistors add the same energy to circuits. For example, if the same current i flows through a positive resistor and through an negative resistor with the same absolute resistance R, the positive resistor subtracts a voltage drop $v = Ri$ from while the negative resistor adds voltage $v = Ri$ to the circuit.

The two-terminal negative resistance circuit shown in Figure 2.9 is an operational amplifier implementation of an "absolute" negative resistor.

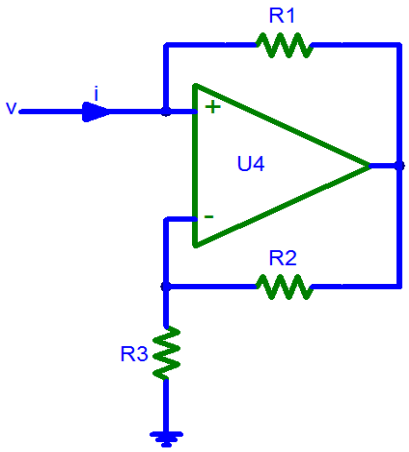

Figure 2.9: A negative impedance converter with current inversion acting as a negative resistor.

The two resistors R_2 and R_3 and the operational amplifier constitute a non-inverting amplifier that serves as the dynamic voltage source needed. It amplifies the input voltage v across the two input circuit terminals and applies it through the resistance R_1 back to the input. For a positive input voltage, the current i is given as

$$i = -\frac{R_2}{R_1 R_3} v. \tag{2.63}$$

The relation between the current i and voltage v is reversed and "pushed" back the current into the input source instead to be drawn from it as in the case of positive resistance. The circuit as though converts the "positive resistance" $R = \dfrac{R_1 R_3}{R_2}$ into negative one by inverting the current direction; thus the name negative impedance converter with current inversion. This will allow us to understand the concept of negative resistance and to be able to build the equivalent circuit of the nonlinear FitzHugh Nagumo's resistance.

2.6.5 Ground load voltage to current converter

Most commonly in parallel circuits, current sources are used in preference to voltage sources, because current signals are exactly equal in magnitude throughout the series circuit loop carrying current from the source to the load. In order to use current as an analog representation of a physical quantity, we have to have some way of generating a precise amount of current within the signal circuit. Our aim to use a voltage-current converter is due to the fact that Fitzhugh-Nagumo circuit which inductance, capacitance and resistance are connected in parallel needs a current source. The voltage to current converter shown in Figure 2.10 delivers a well-regulated current to a load which can be connected to a voltage greater than the operational amplifier supply voltage.

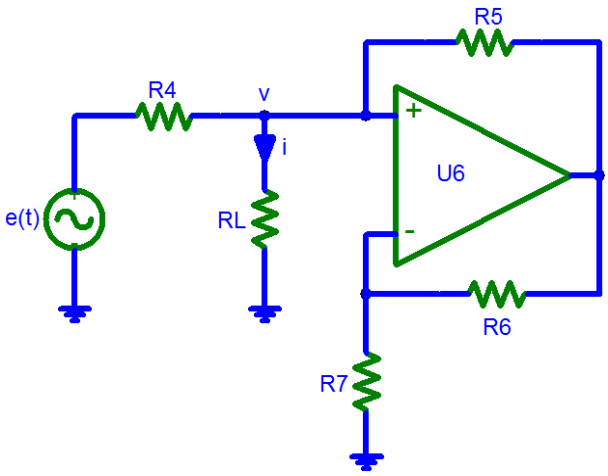

Figure 2.10: The voltage to current converter.

The circuit accepts an input voltage $e(t)$ and converts it to a current i. The application of the Kirchhoff current law at the node v leads to the following expression of i:

$$i = \frac{R_5 R_7}{R_4 R_5 R_7 + R_L \left(R_5 R_7 - R_4 R_6\right)} e\left(t\right). \tag{2.64}$$

Thus, we can conclude from the above equation that if $R_5 R_7 = R_4 R_6$ the current i is related to the voltage, $e(t)$ and the resistor, R_4 as follows:

$$i = \frac{e\left(t\right)}{R_4}. \tag{2.65}$$

The circuit of Figure 2.10 represents a voltage-current converter. Because the output current provides by the circuit is proportional to the input voltage $e(t)$ as well as to R_4^{-1} and independent of those elements of the circuit.

2.7 COMPONENTS AND MATERIALS USED

2.7.1 The accelerometer

An accelerometer is a tool that measures proper acceleration. Proper acceleration is the acceleration of a body in its own instantaneous rest frame; this is different from coordinate acceleration, which is acceleration in a fixed coordinate system. The picture of the multi-axis accelerometer used in this thesis is shown in Figure 2.11.

Single- and multi-axis accelerometers can detect both the magnitude and the direction of the proper acceleration, as a vector quantity, and can be used to sense orientation (because the direction of weight changes), coordinate acceleration, vibration, shock, and falling in a resistive medium.

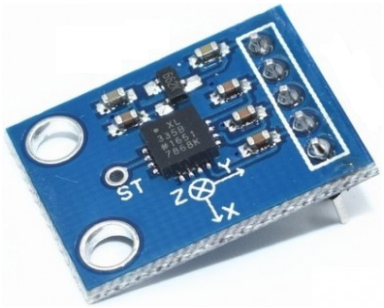

Figure 2.11: Multi-axis accelerometer.

2.7.2 The electrical components

In addition to the components mentioned in the previous section, we have used resistors, ceramic capacitors, electrolytic capacitors, inductors, potentiometers and rectified diodes. Figure 2.12 presents the pictures of these components.

Resistors, ceramic capacitors and inductors have two symmetrical terminals. They can thus be connected easily in the circuits. Electrolytic capacitors and diodes are polarized components due to their asymmetrical construction and must be operated with a higher voltage on the anode than on the cathode at all times. For this reason the anode terminal is marked with a plus sign and the cathode with a minus sign. On the other hand, the potentiometer has three terminals. To use them as a variable resistor, we must connect the terminal in the middle and one other. The screw above the potentiometer allows to vary its resistance. We will need these electrical components for the experimental study of our system.

2.7.3 Function generator

A function generator is usually a piece of electronic test equipment or software used to generate different types of electrical waveforms over a wide range of frequencies. Some of the most common waveforms produced by the function generator are the sine wave, square wave, triangular wave and sawtooth shapes. These waveforms can be either repetitive or single-shot. Integrated circuits used to generate waveforms may also be described as function generator ICs.

In addition to producing sine waves, function generators may typically produce other repetitive waveforms including sawtooth and triangular waveforms, square waves, and pulses. Another feature included on many function generators is the ability to add a DC offset. The picture of the function generator used during our experimental investigations (LW-1641) is shown in Figure 2.13.

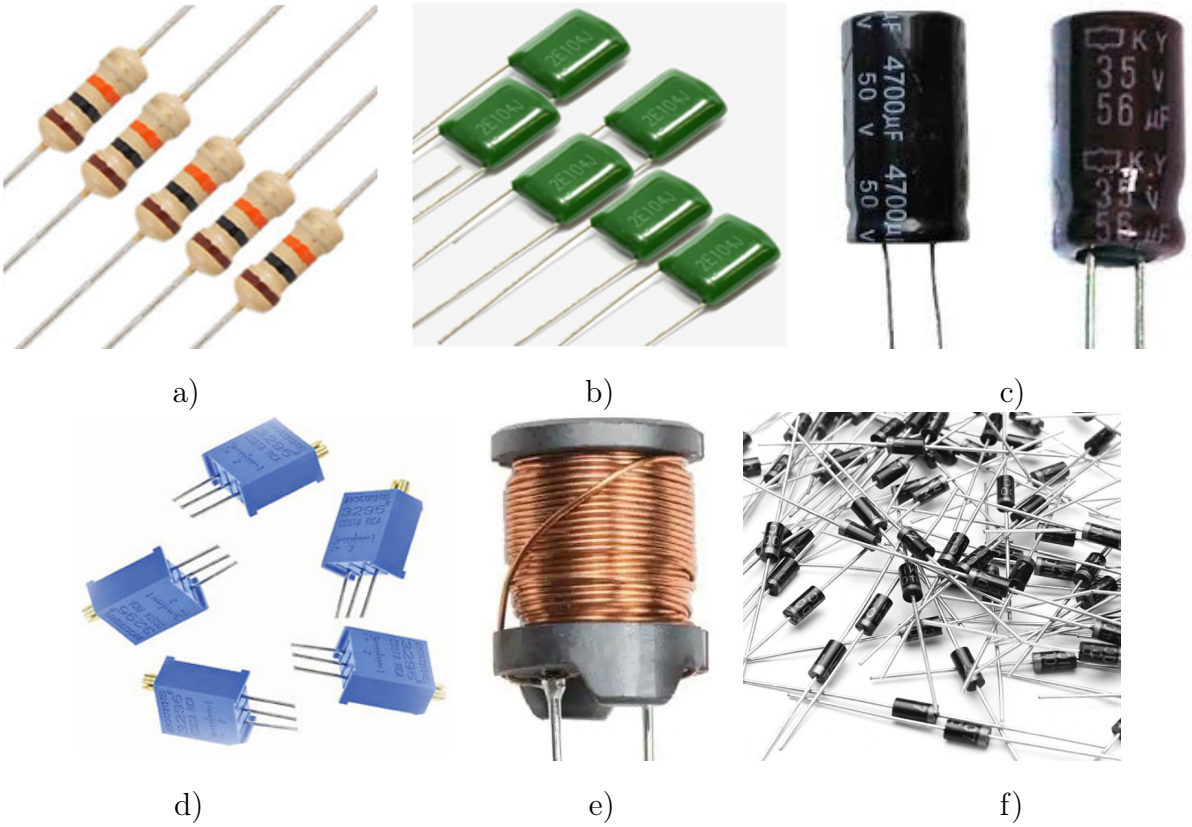

Figure 2.12: a) Resistors, b) Ceramic capacitors, c) Electrolytic capacitors, d) Potentiometers, e) Inductors and f) Rectifier diodes.

Although function generators cover both audio and RF frequencies, they are usually not suitable for applications that need low distortion or stable frequency signals. When those traits are required, other signal generators would be more appropriate. We will use to generate the waveform of the external excitation and some range of frequencies.

2.7.4 Power supply

A dual electric power supply is important for several reasons. Not only does it ensure a stable power supply to a device, but it also helps prevent system damage. It allows for multiple usages of power by increasing output power. In short, it ensures a regular direct current power supply. Our different circuits have been powered by a variable dual $0 - 30V/3A$ and $5V/3A$ fixed Benchtop Supply. The picture is shown in Figure 2.14. We will use electrical power supply to bias the operational amplifier as well as to generate the constant voltage.

Figure 2.13: Function generator of type LW-1641.

Figure 2.14: Power supply of type LS1330.

2.7.5 Breadboard and stripboard

A breadboard is a construction base for prototyping electronics. Originally the word referred to a literal breadboard, a polished piece of wood used for slicing bread. We have used both the solderless breadboard and stripboard shown in figures 2.15a) and 2.15b) respectively.

Because the solderless breadboard does not require soldering, it is reusable. This makes it easy to use for creating temporary prototypes and experimenting with circuit design. For this reason, solderless breadboards are also popular with students and in technological education. Older breadboard types did not have this property. A stripboard (Veroboard) and similar prototyping printed circuit boards, which are used to build semi-permanent soldered prototypes or one-offs, cannot easily be reused. We will use the breadboard for the assembly of our device.

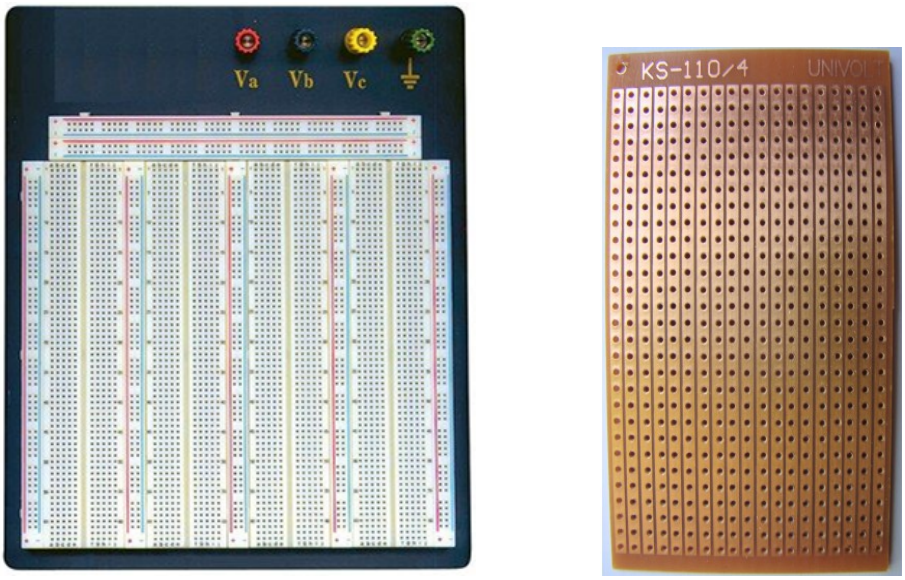

a) b)

Figure 2.15: a) Solderless breadboard and b) stripboard.

2.7.6 Multimeter

A multimeter or a multitester, is an electronic measuring instrument that combines several measurement functions in one unit. A typical multimeter can measure voltage, current, and resistance. Analog multimeters use a microammeter with a moving pointer to display readings. Digital multimeters (DMM, DVOM) have a numeric display, and may also show a graphical bar representing the measured value. We have used a digital multimeter of type DM664 as shown in the picture of figure 2.16.Also, multimeter can serve to check the reliability of the assembly on the breadboard.

2.7.7 Oscilloscope

An oscilloscope which is used for the purpose of digitally storing and analyzing instead of using the analog techniques is referred to as a digital storage oscilloscope. A complex electronic device, it is composed of various electronic hardware software and modules. These are known to work in unity to capture, process, store and display data which represents the signal of interest that the operator possesses. For all our measurements, a digital oscilloscope of type Lw-2102CEL 100MHz Bandwith 2 Channel Digital Storage shown in Figure 2.17 has been used.

Oscilloscopes are used to view the signals coming directly from devices such as sound cards, allowing the real-time display of waves. They are used to test circuits and troubleshoot elec-

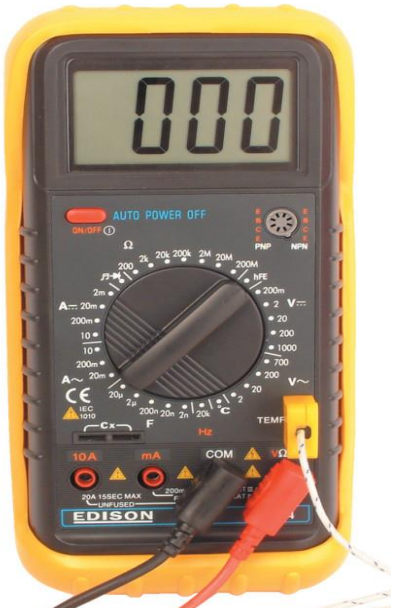

Figure 2.16: Picture of the digital multimeter used during this work.

Figure 2.17: Picture of the Lw-2102CEL 100MHz Bandwith 2 Channel Digital Storage.

tronic devices. Oscilloscopes with storage features allow signals to be captured, retrieved, and analyzed for later use. This oscilloscope will allow us to visualize the curses delivered by our device.

2.7.8 Electromagnetic speakers

Loudspeaker, also called speaker, in sound reproduction, device for converting electrical energy into acoustical signal energy. This definition of a loudspeaker excludes such devices as buzzers, gongs, and sirens, in which the acoustical signal energy does not correspond in form to the electrical signal. Most loudspeakers as presented in Figure 2.18 are of the electromagnetic, or dynamic, variety, in which a voice coil moves in the gap of a permanent magnet when a

time-varying current flows through the coil.

Figure 2.18: Electromagnetic speakers.

The magnet is generally in the shape of a "W" or a ring. The diaphragm, or cone, of such a loudspeaker moves with the coil, converting the electric current in the coil into a pressure wave. A lit candle placed in front of a loudspeaker cone that is oscillating can render the sound wave "visible," as the flame vibrates back and forth longitudinally with the air. The internal structure of an electrodynamics loudspeaker is presented in Figure 2.19.

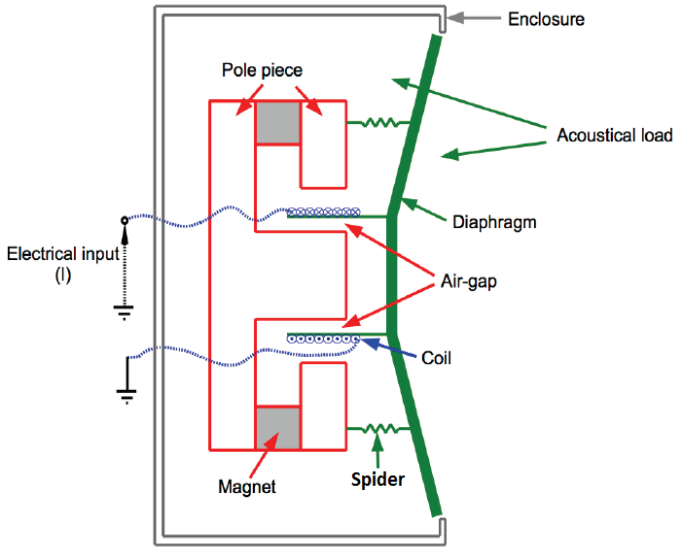

Figure 2.19: Schematic of the electrodynamic loudspeaker.

It consists of three parts:

– electrical which is represented by the voice coil resistance r_m and inductance L_m.

– transducer represented by a gyrator with gyration constant $B\ell$ (called also force factor) where B is the magnetic field provided by the magnet and ℓ is the length of the conductor coil.

– mechanical represented by mass of the moving system m, stiffness k of the spider and

mechanical resistance β. The loudspeaker will be used as the electromechanical arm in the realization of the device.

Conclusion

This chapter aimed to present the description and modeling, mathematical analysis, numerical methods for the dynamics of electromechanical systems. We started by presenting the mathematical modeling of single devices, then we established the mathematical modeling of an array of devices. Methods of mathematical analysis have been presented such as the modal approximation, Routh-Hurwitz criterion, Barkhausen criterion, Cardano's method. The numerical methods for the simulation of ordinary differential equations(ODE) and partial differential equations(PDE) are also given. Finally, the experimental methods, the materials and components used during the experimental work are presented.

Chapter 3

RESULTS AND DISCUSSIONS

Introduction

In the previous chapter, we saw the mathematical study of the electromechanical systems. This chapter is devoted to the presentation of the results and their interpretation. We will first present the theoretical results obtained when nanoelectromechanical beams are driven by an electrical line of Josephson junctions. This is followed by the case where electromechanical arms are powered by a Fitzhugh-Nagumo neuron. Finally, we will present our obtained experimental results and the theoretical results are then compared to the experimental ones.

3.1 NANOELECTROMECHANICAL BEAM DRIVEN BY A SINGLE JOSEPHSON JUNCTION

This section is devoted to the dynamical behavior of a system constituted of one nanoelectromechanical beam driven by a single josephson junction. The values of the physical parameters used in this system are given in Table 3.1.

According to the experimental parameters giving in Table 3.1, we kept constant with the exception of I_e (i_e) the following numerical parameters: $\beta_c = 11.39 \cdot 10^{-3}$, $\eta = 94.07 \cdot 10^{-2}$, $\mu = 37.36 \cdot 10^{-3}$, $\varepsilon = 9.38$, $\gamma = 14.65 \cdot 10^{-3}$, $\omega = 20.28 \cdot 10^{-2}$ and $\alpha = 0.183$.

3.1.1 Stability of the system

The form of the differential equations reveals that the system can have two equilibrium points $G_1\left(\arcsin i_e, 0, 0, 0, 0\right)$ and $G_2\left(\pi - \arcsin i_e, 0, 0, 0, 0\right)$ if the condition $i_e \leqslant 1$ is satisfied. Otherwise, there is no equilibrium point. The Jacobian matrix of the system (2.23) at $G =$

Parameters	Symbols	Values
Junction capacitance	C	3.0 μF
Junction resistance	R	5 $\mu\Omega$
Critical current of the junction	I_c	50 mA
Young's modulus of the nano-beam	E	200 Gpa
Density of the nano-beam	ρ	8050 kg/m^3
Area of the nano-beam	S	$0.224 \cdot 10^{-18}$ m^2
Second moment of area	I	$14 \cdot 10^{-46}$ m^4
Length of the nano-beam	L_1	3.5 nm
Damping coefficient	λ	$2.5 \cdot 10^{-7}$ Ns/m
Magnetic flux intensity	B	0.05 T
Resistance of the winding	r	0.2 $\mu\Omega$
Inductance of the winding	L	$7.0 \cdot 10^{-15}$ H
Length of the wire in the magnetic field	ℓ	20 μm
Coupling inductance	L_c	$6.0 \cdot 10^{-15}$ H

Table 3.1: Values of the physical parameters used when nanoelectromechanical beams are considered.

$(\Phi_0, 0, 0, 0, 0)$ where $\Phi_0 = \arcsin i_e$ or $\Phi_0 = \pi - \arcsin i_e$ is expressed as

$$J = \begin{pmatrix} 0 & 1 & 0 & 0 & 0 \\ -\frac{\cos\Phi_o}{\beta_c} & -\frac{1}{\beta_c} & -\frac{1}{\beta c} & 0 & 0 \\ 0 & \eta & -\mu & 0 & -\varepsilon \\ 0 & 0 & 0 & 0 & 1 \\ 0 & 0 & \gamma & -\omega^2 & -\alpha \end{pmatrix} \tag{3.1}$$

The eigenvalues of the Jacobian matrix J are solutions of the following fifth order algebraic equation in s:

$$s^5 + a_4 s^4 + a_3 s^3 + a_2 s^2 + a_1 s + a_0 = 0, \tag{3.2}$$

where

$$\begin{aligned}
a_4 &= \alpha + \mu + \frac{1}{\beta_c},\\
a_3 &= \alpha\mu + \gamma\varepsilon + \omega^2 + \frac{\cos\Phi_0 + \alpha + \mu + \eta}{\beta_c},\\
a_2 &= \mu\omega^2 + \frac{\alpha\mu + \varepsilon\gamma + \alpha\eta + \omega^2 + (\alpha+\mu)\cos\Phi_0}{\beta_c},\\
a_1 &= \frac{(\mu + \eta + \cos\Phi_0)\,\omega^2 + (\alpha\mu + \varepsilon\gamma)\cos\Phi_0}{\beta_c},\\
a_0 &= \frac{\mu\omega^2\cos\Phi_0}{\beta_c}.
\end{aligned} \tag{3.3}$$

The determinants of all Hurwitz matrices using the coefficients a_i of the characteristic equation (3.2) are given as:

$$\begin{aligned}
d_1 &= a_4,\\
d_2 &= a_4a_3 - a_2,\\
d_3 &= -a_4^2a_1 + a_4a_3a_2 + a_4a_0 - a_2^2,\\
d_4 &= -a_4^2a_1^2 - a_4a_3^2a_0 + a_4a_3a_2a_1 + 2a_5a_1a_0 + a_3a_2a_0 - a_2^2a_1 - a_0^2,\\
d_5 &= -a_4^2a_1^2a_0 - a_4a_3^2a_0^2 + a_4a_3a_2a_1a_0 + 2a_4a_1a_0^2 + a_3a_2a_0^2 - a_2^2a_1a_0 - a_0^3.
\end{aligned} \tag{3.4}$$

According to the Routh-Hurwitz criteria, the system is stable if and only if the coefficients a_i and d_i are all positive. That is, the eigenvalues of the characteristic polynomial have strictly negative real parts. After analysis, we found that the equilibrium point G_1 is unconditionally stable while the point G_2 is unstable.

3.1.2 Oscillation condition and oscillation frequency of the system

For i_e greater than 1, the Josephson junction circuit coupled to the electromechanical block provides asymmetric oscillations as shown in Figure 3.1.

According to the experimental values given in Table 3.1, the natural frequency f_b of the nano-beam and the natural frequency f_j of the Josephson junction can be approximated as follows:

$$\begin{aligned}
f_b &= \frac{1}{2\pi}\left(\frac{1.8751}{L_1}\right)^2\sqrt{\frac{EI}{\rho S}} = 18.0 \text{ MHz},\\
f_j &= \frac{2eRI_c}{2\pi\hbar}\overline{v} = 135.23 \text{ MHz}.
\end{aligned} \tag{3.5}$$

These given values are of the order of MHz. The Characteristic frequency of the Josephson junction circuit used here is compatible with those of Nb-Au-Nb Josephson junction [166, 167].

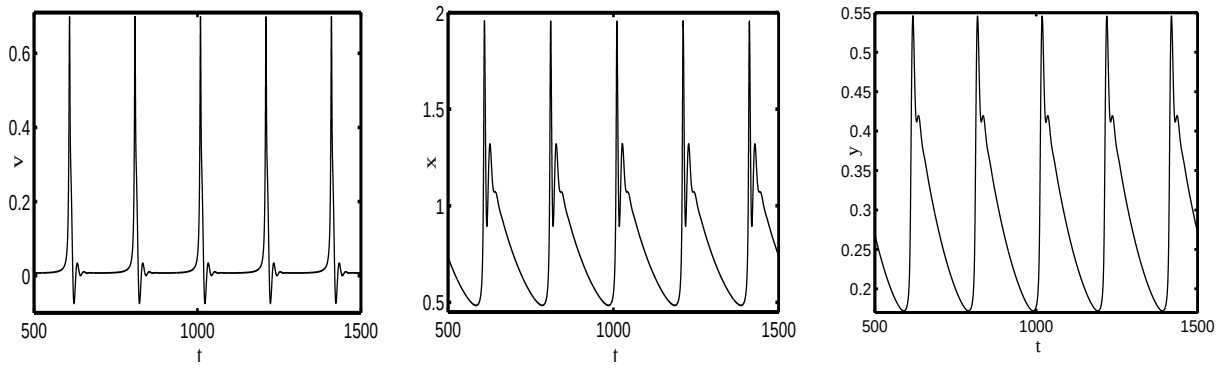

a) b) c)

Figure 3.1: Different waveforms of the system for $i_e = 1.5$ a) junction voltage v, b) current through the winding x and c) displacement of the nanoelectromechanical beam y.

Since the two frequencies are in the same range, both subsystems can affect each other when the Josephon junction is used to power the nano-beam. When the nano-beam and the Josephson junction are connected as shown in the circuit of Figure 2.1, their common frequency is $f = 3.8$ MHz as shown in the curves of Figure 3.1.

3.1.3 Dynamical behavior of the system

At this level, it is interesting to analyze the effect of the input current on the amplitude of the oscillations. Figure 3.2a) shows that the amplitude of the mechanical vibration is an increasing function of i_e.

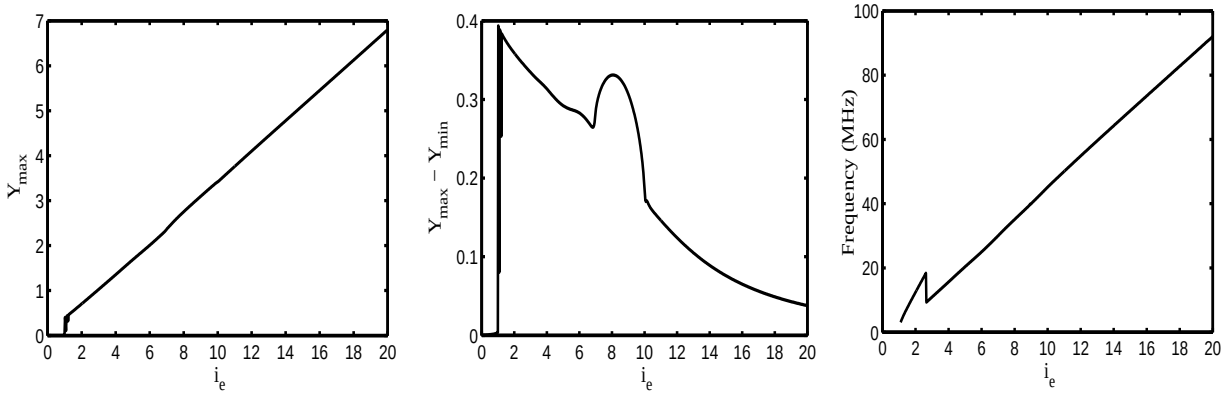

a) b) c)

Figure 3.2: a) Amplitude of the mechanical vibration, b) Peak-peak value of the mechanical vibration and c) frequency of the system, all as function of i_e.

One can notice from the graph that for $i_e \leq 1$, the amplitude is equal to 0 (no oscillation)

while it increases with i_e for i_e greater than 1. It is interesting to note that at just after $i_e = 1$, the amplitude jumps to a finite value and then increases steadily with i_e. Figure 3.2b) shows the behavior of the peak-peak value of y as function of i_e. As the graph reveals, the peak-peak value $(Y_{\max} - Y_{\min})$ of the mechanical vibration is a decreasing function of i_e. We have also found during our investigations that the frequency of the system increases almost linearly with i_e. This effect is illustrated by the graph of Figure 3.2c).

According to all the information just mentioned above, the current x through the winding and the mechanical displacement y converge to a DC signal for large values of i_e. This effect is well visualized in the curves of Figures 3.3a), 3.3b) and 3.3c) where the mechanical displacement y is plotted for three different values of i_e.

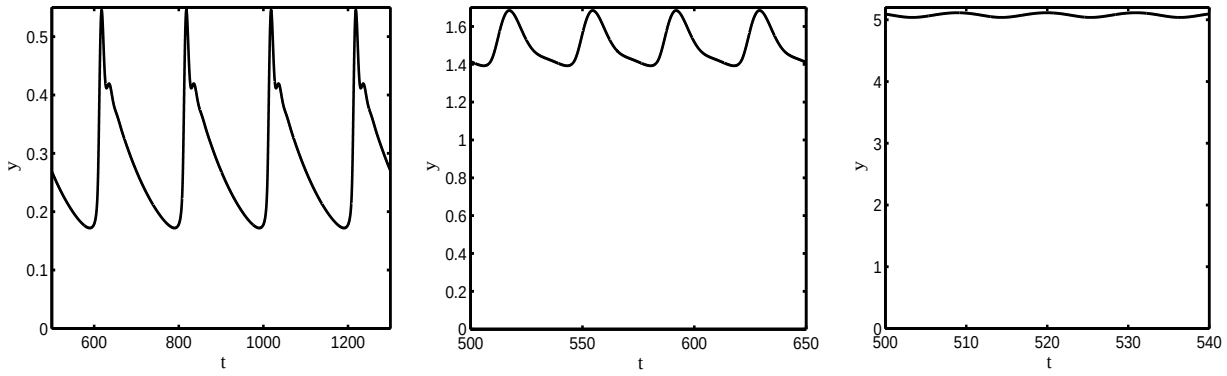

a) b) c)

Figure 3.3: Mechanical displacement y as function of time and for different values of i_e. a) $i_e = 1.5$, b) $i_e = 10.0$ and c) $i_e = 15.0$.

The curves of Figures 3.3a), 3.3b) and 3.3c) are plotted for $i_e = 1.5$, $i_e = 10.0$ and $i_e = 15.0$ respectively. We can notice from the curves that, the corresponding frequencies 3.8 MHz, 20.2 MHz and 75.9 MHz increase with i_e. We can also notice that the peak-peak value is a decreasing function of the input current.

3.2 DYNAMICAL BEHAVIOR OF AN ARRAY OF NANOELECTROMECHANICAL BEAMS DRIVEN BY A DISCRETE ARRAY OF JOSEPHSON JUNCTIONS

This section deals with the array of a nano-beams driven by an array of Josephson Junctions. We analyze numerically the effect of some parameters on the displacement process. As done in the previous section, the values of the physical parameters used in this system are

given in Table 3.1.

3.2.1 Propagation of the signal and motion of the nanoelectromechanical beams

One of the most interesting effects of the discrete Josephson junctions line is its capacity to propagate topological solitons called fluxons (antifluxons) or kinks (antikinks). These topological solitons propagate steadily in the line without changing their shape. The mathematical form of the antikink (or antifluxon) [168] is given by the following expression

$$\phi(n,t) = 4\arctan\exp\left(-\frac{n-\nu t-n_0}{\sqrt{1-\nu^2}}\right), \tag{3.6}$$

where ν is the velocity and n_0 is the initial node where the center of the antikink is located. With $n_0 = 100$ and $\nu = 0.5$, the antikink profile is plotted in Figure 3.4.

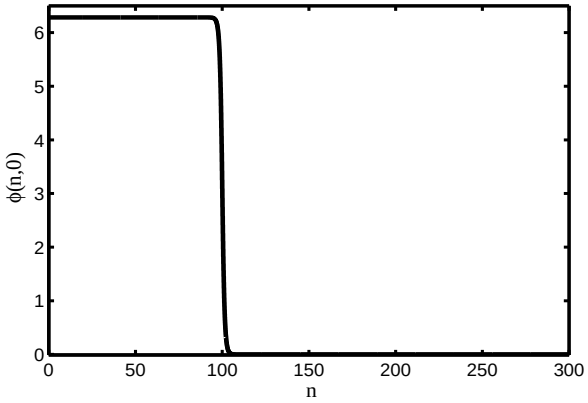

Figure 3.4: The antikink profile centered at $n_0 = 100$.

In this section, the set of discrete differential equations (2.33) is solved numerically using the fourth order Runge-Kutta algorithm with a time step $h_t = 5 \cdot 10^{-3}$ [169]. For the initial conditions, we insert the mathematical form (3.6) in the discrete equation at site $n_0 = 100$.

Periodic boundary conditions are used by setting $\phi(n=0) = \phi(n=N)+2\pi$ and $\phi_n(n=0) = \phi_n(n=N)$, N is the total number of cells and is equal to 300. Figure 3.5 displays the antikink propagation in the discrete line as well as the behavior of the nano-beams when the antikink propagates in the Josephson junction line.

Figures 3.5a), 3.5b) and 3.5c) show respectively the propagation of the antikink, the current x through the winding and the displacement y of the nanoelectromechanical beam as function of the number of cells.

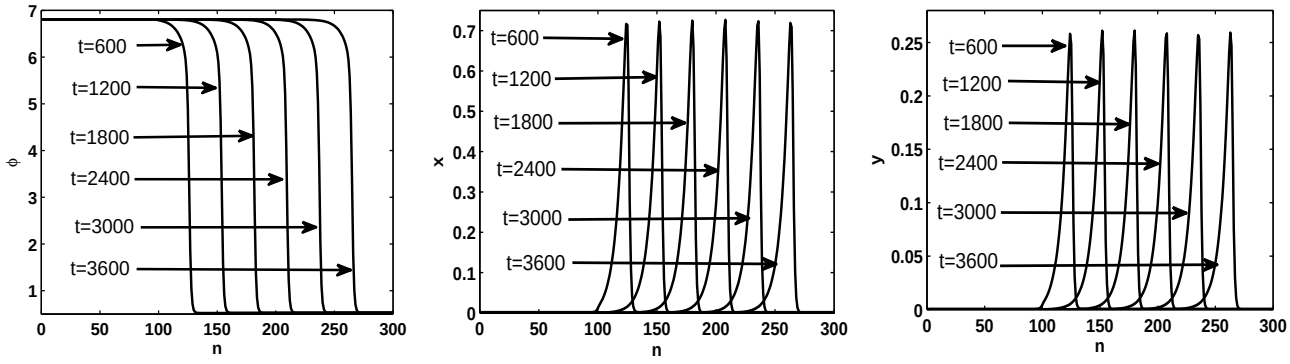

a) b) c)

Figure 3.5: Different waveforms of the system as function of number of cells at different times for $i_e = 0.5$: a) phase ϕ, b) current x through the winding and c) displacement y of the nanoelectromechanical beam.

As it appears in Figure 3.5, the antikink shape is preserved during the propagation and each nano-beam exhibits a pulse-like behavior moving from its rest state, then increases till a maximal value and then decreases to the rest state. This is interesting since it indicates the nano-beam executes an actuation work and then returns back to its rest state.

If the antikink is periodically inserted in the line, the nano-beam will periodically exhibits pulse-like behavior. The periodic insertion of antikinks in the transmission lines is ensured by the periodic boundary conditions which indicates that the kink periodically passes at one point after propagating all over the discrete line. We have found that the amplitude and the frequency of the nano-beam displacement increase with the intensity of the magnetic field as it appears in Figures 3.6a), 3.6b) and 3.6c) plotted respectively for $B = 0.01$ T, $B = 0.05$ T and $B = 0.09$ T.

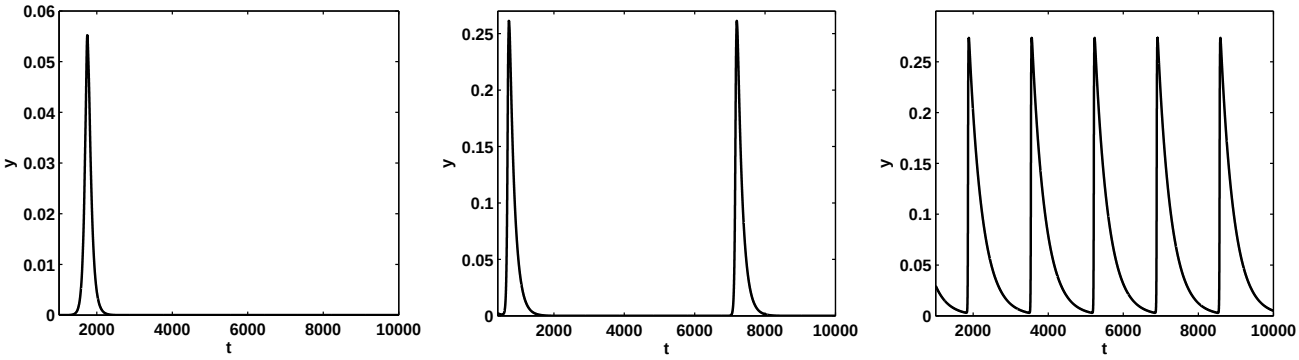

a) b) c)

Figure 3.6: The time evolution of the nanoelectromechanical beam for different values of the magnetic field recorded at the cell $n = 130.a)$ $B = 0.01$ T, b) $B = 0.05$ T and c) $B = 0.09$ T.

3.2.2 Effect of the bias current on the nanoelectromechanical beams dynamics

We have simulated the system for different values of i_e (0.7, 0.8, 1.0). It appears that a given nano-beam periodically exhibits pulse-like behavior as it can be seen in Figure 3.7 where one observes the displacement of the nano-beam at the cell number $n = 130$.

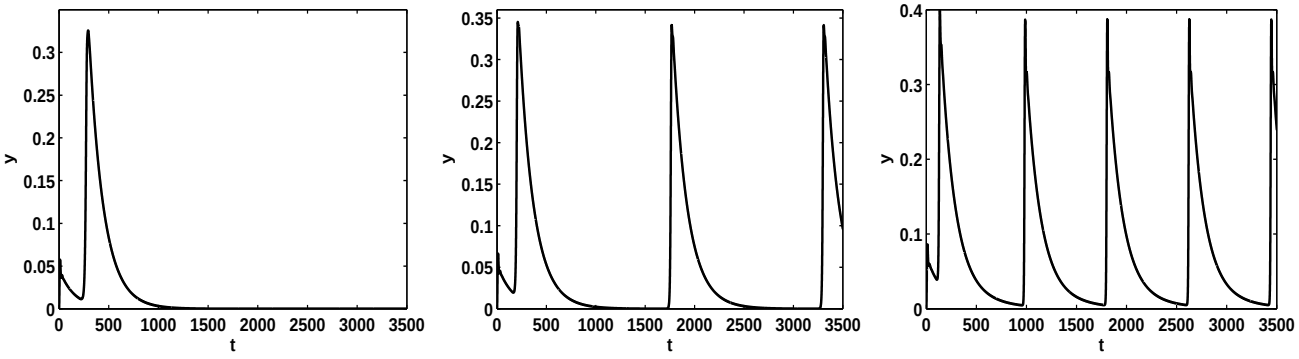

a) b) c)

Figure 3.7: The time evolution of the nanoelectromechanical beam for different values of the bias current recorded at the cell $n = 130$.(a $i_e = 0.5$, (b) $i_e 0.7$ and (c) $i_e = 1.0$.

As i_e increases, the vibration frequency increases moving from almost 208 kHz (for $i_e = 0.5$) to 245 kHz (for $i_e = 0.7$) and then 925 kHz (for $i_e = 1.0$). The increase of the frequency can be understood by the fact the antikink velocity increases proportionally with i_e [170,171]. Because of this increase of velocity and the boundary conditions, the antikink turns round the line as quickly as i_e increases. Consequently, each nano-beam is periodically excited and then delivers periodic pulse-like behavior.

As one observes in Figure 3.7, the amplitude of the nano-beam pulse-like behavior also increases with i_e. Our numerical simulations have also shown that the amplitude depends of the resistance r of the winding. This fact is more detailed in Figure 3.8 where the amplitude of the mechanical displacement is plotted versus i_e and for different values of r.

3.3 DYNAMICAL BEHAVIOR OF AN ELECTROMECHANICAL ARM POWERED BY A FITZHUGH-NAGUMO NEURON

We present in this section the dynamical behavior of one single Fitzhugh-Nagumo neuron coupled magnetically to a mechanical arm. The stability of the system, the oscillation condi-

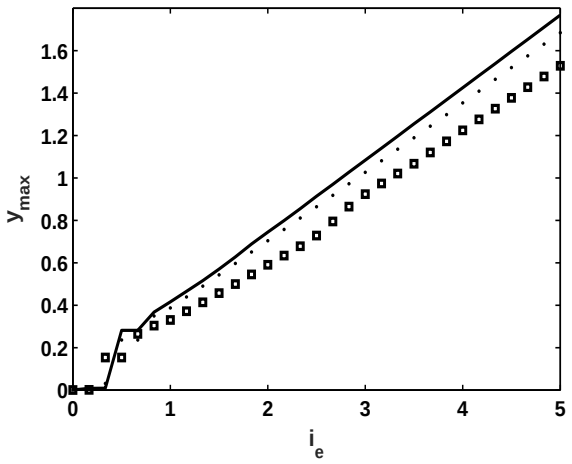

Figure 3.8: Variation of the $n = 120$ nano-beam displacement amplitude as function of the bias current i_e for different values of r: $r = 0.08\ \mu\Omega$ (full line), $r = 0.2\ \mu\Omega$ (dot line) and $r = 0.7\ \mu\Omega$ (square line).

tion and the corresponding frequency are presented. The effects of some parameters on the dynamical behavior of the system are also analyzed.

3.3.1 Stability analysis

Assume $E(v_0,\ w_0,\ z_0,\ u_0,\ y_0,\ x_0)$ is the equilibrium point of the system. From the system of equations (2.31), we have $w_0 = \dfrac{v_0}{r}$, $z_0 = 0$, $u_0 = v_0$, $y_0 = 0$, and $x_0 = 0$ while v_0 is the solution of the following third-order algebraic equation:

$$v_0^3 - (\mu_1 + \mu_2)\, v_0^2 + \left(\mu_1\mu_2 + \frac{1}{\alpha r}\right) v_0 - \frac{I_s}{\alpha} = 0. \tag{3.7}$$

To derive solutions of equation (3.7), let us consider the following parameters δ and σ_1 and determinant Δ:

$$\delta = (\mu_1 + \mu_2)^2 - 3\left(\mu_1\mu_2 + \frac{1}{\alpha r}\right),\ \sigma_1 = (\mu_1 + \mu_2)\left(\frac{9}{2\alpha r} - \mu_1^2 - \mu_2^2 + \frac{5}{2}\mu_1\mu_2\right) - \frac{27 I_s}{2\alpha} \tag{3.8}$$

and $\Delta = \sigma_1^2 - \delta^3$.

As odd degree polynomial, equation (3.8) can have one or three real solutions according to the values of the above parameters, and the sign of Δ.

If $\Delta > 0$, equation (3.8) has one real solution and the system has a single equilibrium point.

$$v_0 = \frac{1}{3}\left(\mu_1 + \mu_2 - \sqrt[3]{\sqrt{\Delta} + \sigma_1} + \sqrt[3]{\sqrt{\Delta} - \sigma_1}\right). \tag{3.9}$$

If $\Delta \leq 0$, equation (3.8) has three real solutions, namely:

$$v_{0n} = \frac{1}{3}\left(\mu_1 + \mu_2 + 2\sqrt{\delta}\cos\left(\frac{\theta + 2n\pi}{3}\right)\right) \text{ with } n = -1,\ 0,\ 1 \text{ and } \theta = \arctan\left(\frac{\sqrt{-\Delta}}{\sigma_1}\right).$$

(3.10)

In this case, the system has three equilibrium points.

The values of the parameters used in this work are the following: $\beta_0 = 0.05$ Ns/m, $m = 20$ mg, $K = 10$ N/m, $B = 0.8$ T, $C = 60$ μF, $L = 240$ mH, $\mu_1 = 0.14$ V, $\mu_2 = 1.0$ V, $r = 2.5$ Ω and $C_m = 4700$ μF. I_s and ℓ are used as control parameters with $0 \leqslant I_s \leqslant 200$ mA and $0 \leqslant \ell \leqslant 10$ m. With the variation of ℓ, the winding resistance (in Ω) and the winding inductance (in mH) are given as: $r_m = 1.5\ell$ and $L_m = 1.25\ell^2$.

Using the parameters given above, the evolution of the equilibrium potential v_0 is plotted as a function of the stimulation current I_s in Figure 3.9, and for two different values of the parameter α.

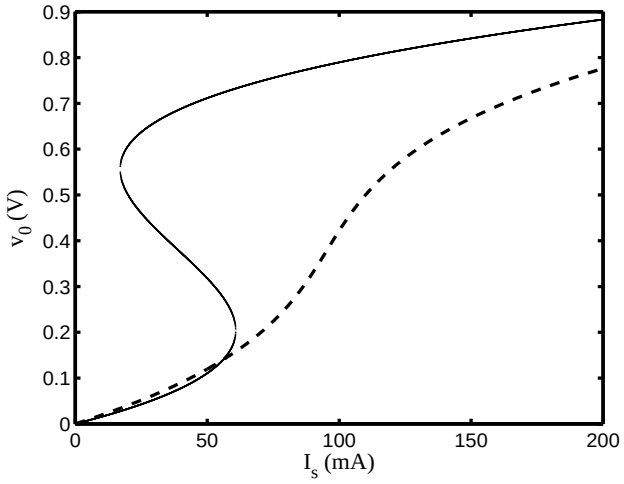

Figure 3.9: Equilibrium potential v_0 as a function of the stimulation current I_s. The curve with dashed line is obtained for $\alpha = 1$, while the curve with full line is obtained for $\alpha = 2$.

For the graph of Figure 3.9, we have considered $\ell = 1$ m. The curve with a dashed line and the curve with a full line are obtained respectively for $\alpha = 1$ and $\alpha = 2$. As predicted analytically, the system can present one equilibrium potential or three equilibrium potentials depending on the values of the parameters. As noticed from the graph, for $\alpha = 2$, the case of three equilibrium points arrives here for values of the stimulation currents between 17.01 mA and 60.815 mA.

The unstable (or stable) branch connecting the two stable (or unstable) states of the hys-

teresis cycle extends from I_{s-} to I_{s+} given respectively as

$$\begin{aligned} I_{s\mp} &= \alpha v_{\mp}\left(v_{\mp}^2 - (\mu_1+\mu_2)\,v_{\mp} + \mu_1\mu_2 + \frac{1}{\alpha r}\right) \\ \text{where } v_{\mp} &= \frac{\mu_1+\mu_2}{3} \mp \sqrt{\left(\frac{\mu_1+\mu_2}{3}\right)^2 - \frac{\mu_1\mu_2}{3} - \frac{1}{3\alpha r}}. \end{aligned} \tag{3.11}$$

From equation (3.10), we can conclude that the system will present three equilibrium points if the parameter α satisfies the following condition:

$$\alpha \geqslant \alpha_{\min} = \frac{3}{r\left(\mu_1^2+\mu_2^2-\mu_1\mu_2\right)}. \tag{3.12}$$

For $\alpha \leqslant \alpha_{\min}$ we have a mono system while for $\alpha \geqslant \alpha_{\min}$ the curve of Figure 3.9 presents a bistable system. According to Tlidi et al., there must be a critical alpha of nascent bistability [172].

The stability of the system is determined by the eigenvalues of the Jacobian matrix at equilibrium points E given by :

$$J = \begin{bmatrix} -a\chi\alpha & -a & 0 & 0 & -a & 0 \\ b & -br & 0 & 0 & 0 & 0 \\ 0 & 0 & 0 & 1 & 0 & 0 \\ 0 & 0 & -\varepsilon & -\beta & \sigma & 0 \\ d & 0 & 0 & -d\gamma & -dr_m & -d \\ 0 & 0 & 0 & 0 & q & 0 \end{bmatrix}, \tag{3.13}$$

with $\chi = 3v_0^2 - 2\left(\mu_1+\mu_2\right)v_0 + \mu_1\mu_2$.

Its eigenvalues are solutions of the characteristic polynomial in λ of the linearization at E, namely:

$$\lambda^6 + a_5\lambda^5 + a_4\lambda^4 + a_3\lambda^3 + a_2\lambda^2 + a_1\lambda + a_0 = 0. \tag{3.14}$$

Here the coefficients a_n, with $0 \leq n \leq 5$ are given respectively as:

$$\begin{aligned} a_5 &= a\alpha\chi + \beta + dr_m + br, \\ a_4 &= (a\alpha\chi+\beta)(br+dr_m) + brdr_m + d\gamma\sigma + \varepsilon + dq + a\alpha\chi\beta + a(b+d), \\ a_3 &= (\varepsilon + a\alpha\chi\beta)(br+dr_m) + a\beta(b+d) + abd(r+r_m) + brdr_m(\beta+a\alpha\chi) + brd\gamma\sigma + \\ &\quad + a\alpha\chi(\varepsilon+d\gamma\sigma) + dq(\beta+br+a\alpha\chi), \\ a_2 &= brdr_m(\varepsilon+a\alpha\chi\beta) + abd\beta(r+r_m) + abd\gamma\sigma + a\alpha\chi\varepsilon(br+dr_m) + bra\alpha\chi d\gamma\sigma + \\ &\quad + a\varepsilon(b+d) + \varepsilon dq + bdrq(\beta+a\alpha\chi) + adq(b+\alpha\chi\beta), \\ a_1 &= abd\varepsilon(r+r_m+\alpha a\chi r r_m) + dqb(\varepsilon r + a\beta) + a\alpha\chi dq(\varepsilon+br\beta), \\ a_0 &= ab\varepsilon dq(1+\alpha r\chi). \end{aligned}$$

We have used the Routh-Hurwitz criterion to analyze the stability of the equilibrium points. Using the parameters given above, the stability boundary of the system is plotted in Figure 3.10a) and Figure 3.10b) for $\alpha = 1$ and $\alpha = 2$ respectively.

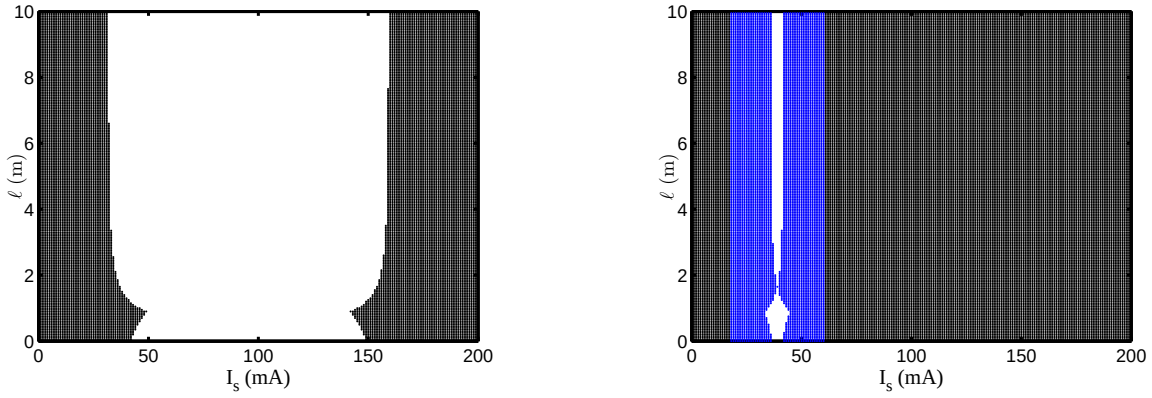

Figure 3.10: Stability domain in the plane (I_s, ℓ). In the Black area, the system is stable around the single equilibrium point while in the white area, the system is unstable. In the blue area, the system has one stable equilibrium point amount three. a) $\alpha = 1$ and b) $\alpha = 2$.

In Figure 3.10a), we have two colored regions, while in Figure 3.10b) we have three colored regions. If a coupled of values I_s and ℓ is chosen in the black regions, the system is stable around the single equilibrium point. However, if a coupled of values I_s and ℓ is chosen in the white regions, the system is unstable. In the blue region of Figure 3.10b), the system has three equilibrium points, and one of these is stable.

3.3.2 Limit cycle prediction

Although precise knowledge of the waveform of a limit cycle is usually not mandatory, knowledge of the existence of a limit cycle, and its approximate amplitude and frequency, is a prerequisite to good system design. The limit cycle phenomenon deserves special attention since it is apt to occur in any nonlinear physical system. A limit cycle is desirable here since it provides a real situation where all the variables are not constant. We will apply the linear theory to the quasi-linearized system, and points of neutral stability are sought. Any undamped oscillations so arrived at are interpreted as limit cycles in the original nonlinear system.

If we consider the solution of equation (3.14) to be of the form of $\lambda = j\omega$, where $j^2 = -1$ and ω is the natural radian frequency of the system, then the following radian frequencies and the condition for self-starting are obtained:

$$\omega_1 = \sqrt{\frac{a_3 - \sqrt{a_3^2 - 4a_1a_5}}{2a_5}} \quad \text{and} \quad \omega_2 = \sqrt{\frac{a_3 + \sqrt{a_3^2 - 4a_1a_5}}{2a_5}}. \tag{3.15}$$

$$a_3^2 - 4a_1a_5 \geqslant 0 \text{ and } \left(a_1a_5 - a_3^2 - a_2a_5^2 + a_3a_4a_5\right)\omega_n^2 + \left(a_0a_5^2 + a_1a_3 - a_1a_4a_5\right) = 0,\ n = 1,\ 2. \tag{3.16}$$

During our investigations, we have found that for large values of the parameter ℓ, the system oscillates with the radian frequency ω_1 while it oscillates with the radian frequency ω_2 for small values of ℓ. With the stimulation current I_s varies from 0 mA up to 200 mA, we have found the corresponding values of ℓ that satisfy the set of equations (3.16) and our result is presented in the graph of Figure 3.11a). The corresponding value of the frequency obtained from equation (3.15) is plotted in Figure 3.11b).

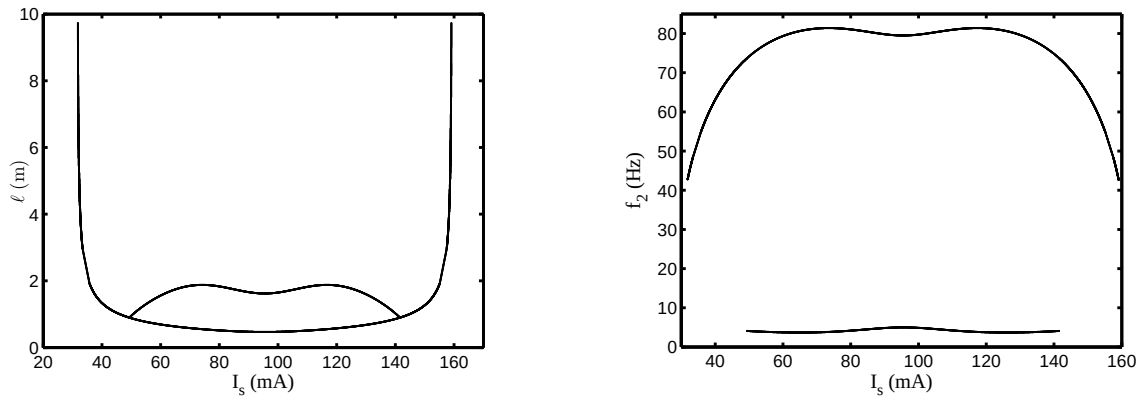

a) b)

Figure 3.11: a) The oscillation condition satisfied by the parameter ℓ as a function of I_s, b) the natural frequency of the system as a function of I_s.

The curves of Figure 3.11 are obtained for $\alpha = 1$ and the values of $\ell < 10$ m have been considered. We can notice from the graph that, as the stimulation current increases, the value of ℓ that satisfies the oscillation condition given by equation (3.16) can be found if 31.83 mA$\leq I_s \leq$ 159.1 mA.

3.3.3 Oscillation boundaries

Using the Routh-Hurwitz coefficients, we have determined the oscillation boundaries of the system and our results are presented in Figure 3.10a). If the values of I_s and ℓ are chosen

in the black areas of Figure 3.10a), the system will converge towards the equilibrium point. Otherwise, the system will fall in the oscillation. For example, with $\ell = 1$ m we find that the system will oscillate for 33.7 mA$\leq I_s \leq$ 154.0 mA. To verify this result, we have consider the following three values of I_s: $I_s = 30$ mA, $I_s = 90$ mA and $I_s = 160$ mA. The corresponding time series of the membrane potential and the mechanical displacement are plotted respectively in Figure 3.12 and Figure 3.13.

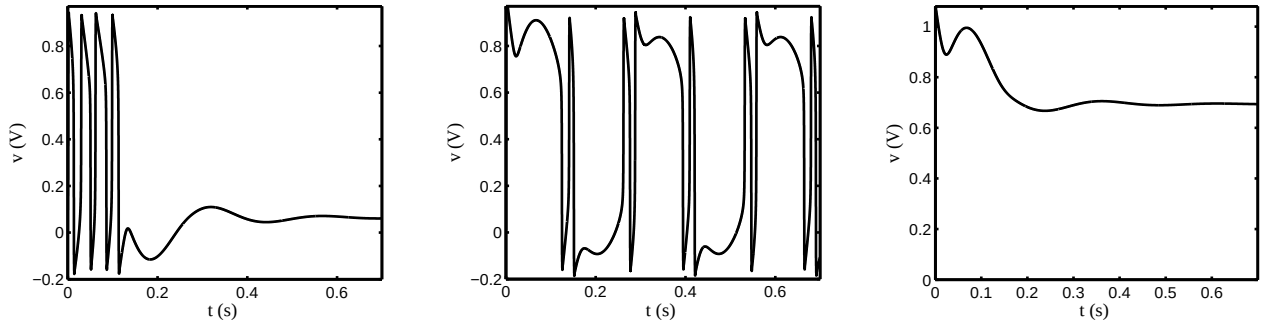

Figure 3.12: Different time series of the membrane potential v for different values of I_s. a) $I_s = 30$ mA, b) $I_s = 90$ mA and c) $I_s = 160$ mA.

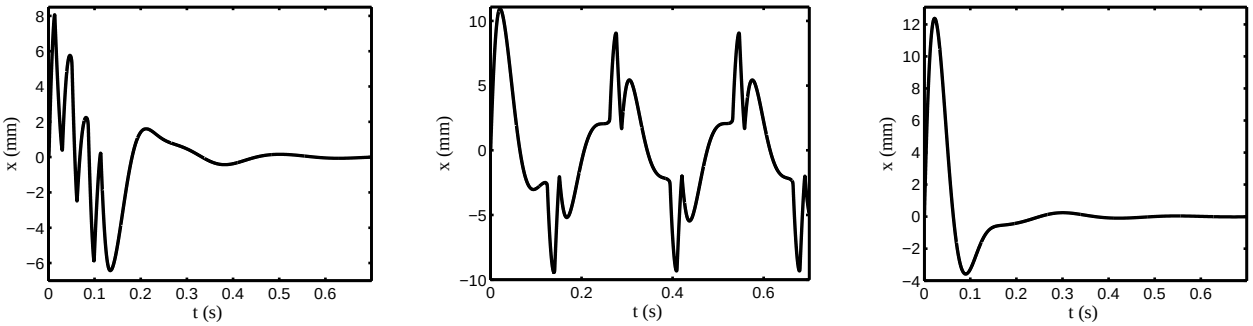

Figure 3.13: Different time series of the mechanical displacement x for different values of I_s. a) $I_s = 30$ mA, b) $I_s = 90$ mA and c) $I_s = 160$ mA.

As shown on the graphs of Figure 3.12 and Figure 3.13, when the stimulation current is less than 33.7 mA or greater than 154.0 mA, the system converges toward the single stable equilibrium point. While if the stimulation current is between 33.7 mA and 154.0 mA, the system provides oscillating signals. The frequency of the signal plotted in the graph of Figures 3.12b) and 3.13b) is 3.704 Hz. The obtained numerical results are in good agreement with our analytical predictions.

3.3.4 Effect of some parameters

It is interesting at this level to see how some parameters affect the dynamics of the system, specially the amplitude and frequency of the mechanical displacement. This element can be important to fix the parameters of the system. We will first analyze the effect of the length ℓ of the conductor used in the winding. Therefore, we plot the amplitudes of the membrane potential and the mechanical displacement as a function of ℓ and this for two different values of the spring constant as presented in Figure 3.14.

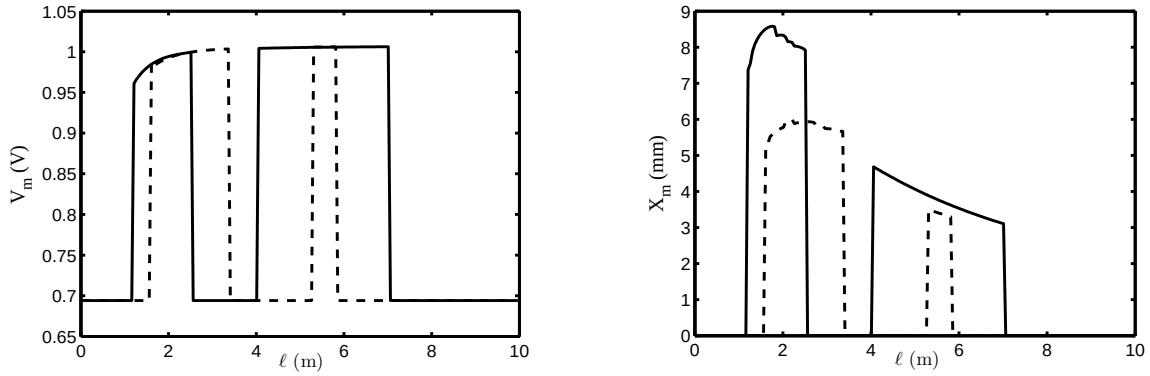

a) b)

Figure 3.14: a) Amplitude of the membrane potential V_m as function of ℓ, b) Amplitude of the mechanical displacement X_m as function of ℓ. Full line ($K = 10$ N/m) and dashed line ($K = 20$ N/m).

For both Figures 3.14a) and 3.14b), the full lines and the dashed lines are plotted respectively for $K = 10$ N/m and $K = 20$ N/m. As revealed by the graphs, when the system oscillates, the amplitude of the membrane potential is closed to unity while the amplitude of the mechanical displacement is a decreasing function of ℓ. Otherwise, the system converges to the equilibrium point. The mechanical displacement reaches its maximum value when $\ell \simeq 2$ m. As mentioned in the previous section and clearly confirmed by these graphs, the system presents large oscillation regions for small values of the spring constants. This is because electromechanical systems generally oscillate at low frequencies, which means small values of the spring constants. We can also notice from the graphs that the equilibrium points are not a function of the spring constant K and the length ℓ of the conductor used in the winding, and this has been observed during our analytical investigations presented previously. Finally, the graphs show that the amplitude of the mechanical displacement and the oscillation domain are decreasing functions of the spring constant.

Furthermore, we analyze the dynamical behavior of the system using the stimulation current

I_s as the control parameter. The amplitude responses of electrical and mechanical subsystems are respectively shown in Figure 3.15a) and Figure 3.15b) for two values of ℓ.

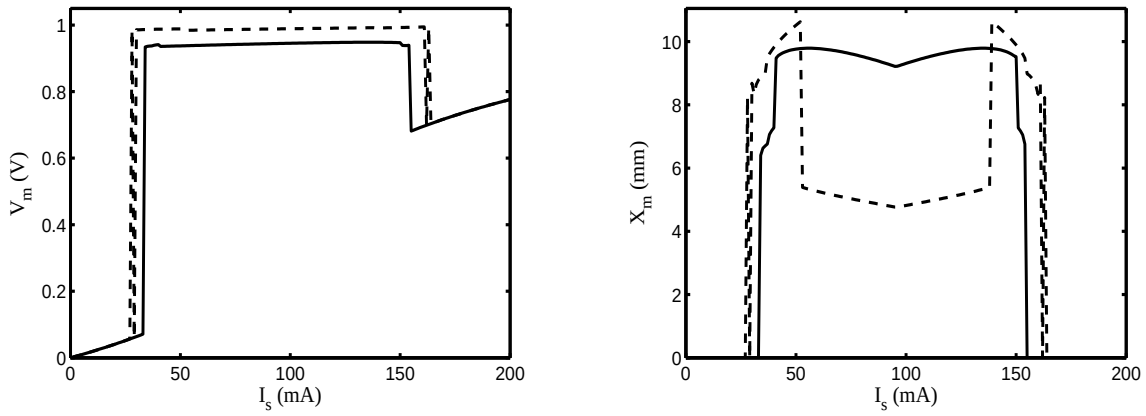

a) b)

Figure 3.15: a) Amplitude of the membrane potential V_m as a function of I_s, b) Amplitude of the mechanical displacement X_m as a function of I_s. Full line ($\ell = 1$ m) and dashed line ($\ell = 2$ m).

For both Figures 3.15a) and 3.15b), the curves with the full line are plotted for $\ell = 1$ m, while the curves with dashed lines are plotted for $\ell = 2$ m. Three regions can be identified in these figures. Firstly, for the stimulation current less than approximatively 30 mA (depending on the length of the conducting wire), the action potential is not produced, hence no oscillation of the mechanical system. Secondly, when 30 mA $\leq I_s \leq$ 162 mA, an action potential is generated and we have oscillation of the mechanical system. In the third region, the mechanical system is at equilibrium even if an action potential has been generated in the electrical system. We can notice from the graphs that when the system falls in the oscillation, the amplitude of the membrane potential and the amplitude of the mechanical displacement are not affected by the input current I_s. The figures also show that the amplitudes remain constant (no oscillation) as the stimulation current I_s increases until a critical value from where both amplitudes increase abruptly.

3.3.5 Transient chaos in the system

The appearance of chaos with finite lifetime is known as transient chaos and provides an example of a "nonequilibrium state" that is different from the asymptotic state, and cannot thus be understood from the asymptotic behavior alone. In such case, one observes a moving around of the system in an apparently chaotic manner and then, often rather suddenly, a settling down to a steady state which is either a periodic or a chaotic motion (but of different type than the

transients). Studying only the asymptotic behavior of such dynamics would mean loosing the interesting, chaotic part contained in the transients. Figure 3.16 shows the phase portraits of the action potential v illustrating the transient chaos in the system.

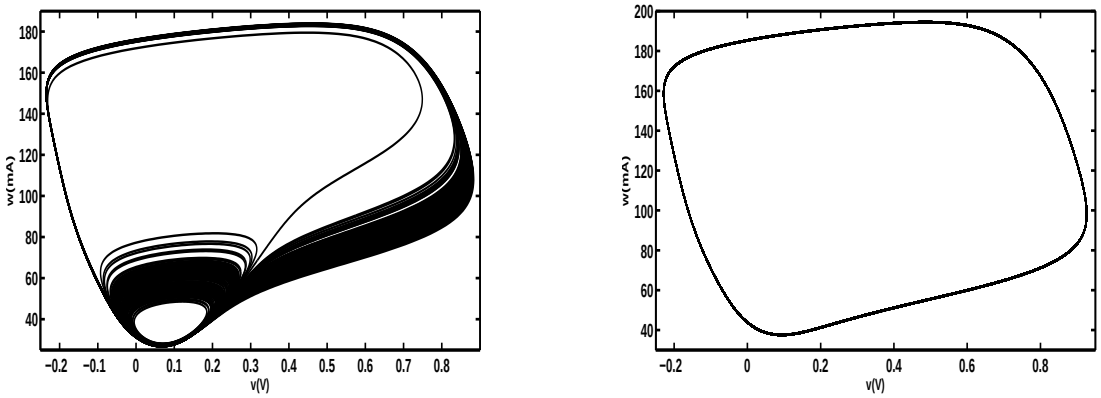

a) b)

Figure 3.16: a) Chaotic attractor in the time interval 28.28 s $\leq t \leq$ 29.7 s. b) Period-one attractor in the time interval 282.84 s $\leq t \leq$ 284.25 s.

The curves of Figure 3.16 are plotted when $C_m = 4700$ mF, $\ell = 4$ m and $L = 6$ mH. We found during our investigation that, the transient chaos appears in the system for high values of the coupling capacitance and for small values of the coil inductance.

3.3.6 Chaotic behavior

The characteristic dynamical behaviors are finally investigated by varying the type of the input current source. We have done many simulations, but a part of transient chaos [173, 174], permanent chaotic behavior has not been found in the autonomous system. Hence, the constant current source is replaced here by a sinusoidal current source of amplitude I_m and frequency f defined as

$$i_s = I_s + I_m \sin(\omega t) \quad \text{where} \quad \omega = \frac{2\pi f}{\omega_0}, \tag{3.17}$$

where I_s represents the DC component and ω is the normalized radian frequency of the external source. We will study the dynamics of the system keeping constant the following parameters: $\ell = 4$ m, $L = 7.0$ mH and $f = 780.72$ Hz. For I_s equals successively 3 mA, -3.4 mA, -5 mA, -7 mA, -12 mA and -15 mA, the bifurcation diagrams v versus I_m and the corresponding Lyapunov exponent versus I_m are shown in Figure 3.17.

In Figures 3.17a), 3.17b), 3.17c) and 3.17d), chaotic states are observed. The system follows a period-doubling route to chaos. The bifurcation diagrams of these figures also undergo a

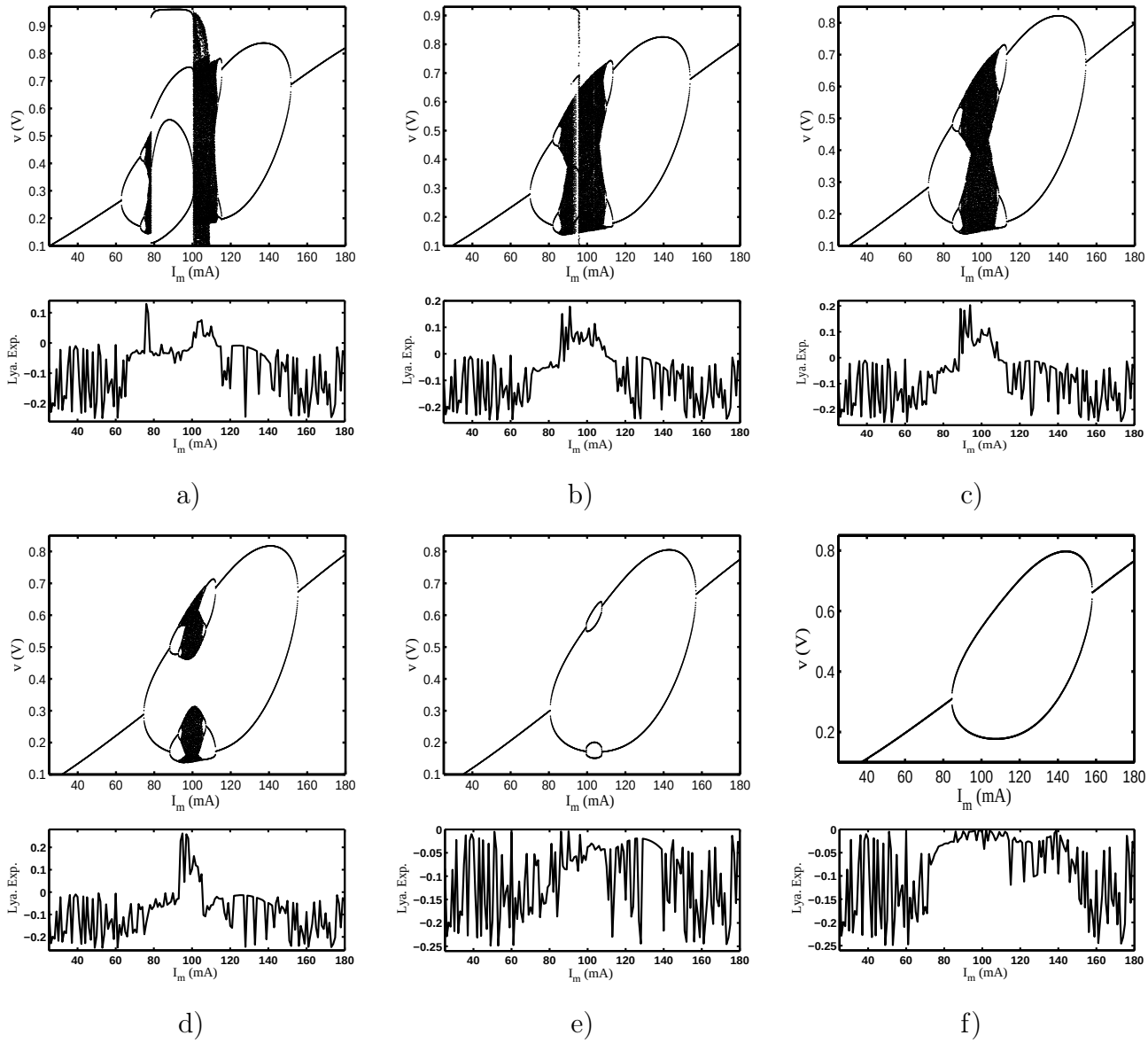

Figure 3.17: Different Bifurcation diagrams v versus I_m and the corresponding Lyapunov exponent versus I_m of the system for different values of the DC component: a) $I_s = 3$ mA, b) $I_s = -3.4$ mA, c) $I_s = -5$ mA, d) $I_s = -7$ mA, f) $I_s = -12$ mA and e) $I_s = -15$ mA.

reverse period-doubling sequence. These forward and reverse period doubling sequences, as a parameter of the system increases in a monotone way, are called antimonotonicity. While in the bifurcation diagrams of Figures 3.17e) and 3.17f), only periodic states are observed. For $I_s = -12$ mA, the system undergoes the sequence: $p_1 \to p_2 \to p_4 \to p_2 \to p_1$. For $I_s = -15$ mA, the system undergoes the sequence: $p_1 \to p_2 \to p_1$. These bifurcation diagrams show the period bubble and the primer bubble respectively.

The study of the system (2.31) with the external current source given by equation (3.17) reveals the existence of chaotic behavior, following the period-doubling route to chaos. Similar

results can be obtained using a current source that provides a square signal with DC component I_s and frequency f. For illustration, phase portraits of the system in the chaotic state are shown in Figures 3.18a) and 3.18b).

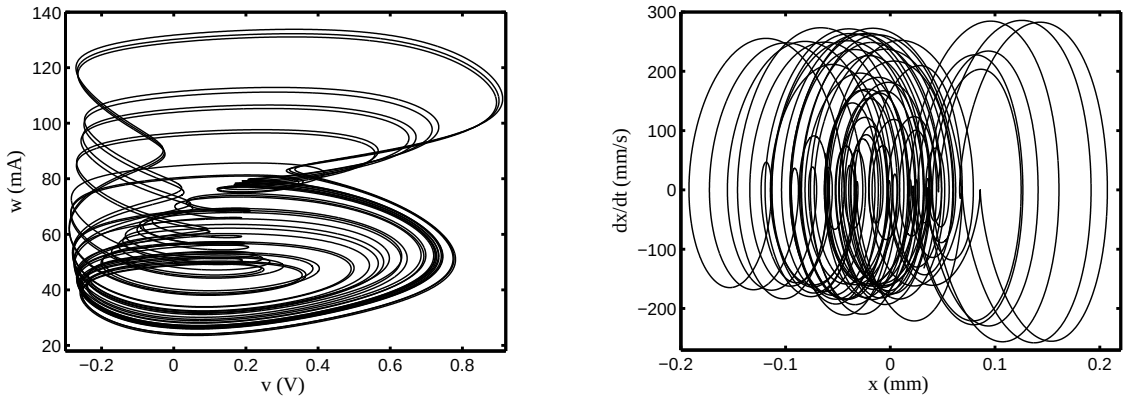

a) b)

Figure 3.18: Phase portraits when $I_s = 3.0$ mA, and $I_m = 102.0$ mA. a) w versus v and b) $\dot{x}$ versus x.

3.4 DYNAMICAL BEHAVIOR OF AN ARRAY OF ELECTROMECHANICAL ARMS POWERED BY AN ARRAY OF FITZHUGH NAGUMO NEURONS

We now analyze the dynamical behavior of an array of electromechanical arms powered by an array of discrete excitable Fitzhugh Nagumo neurons. We present the effect of the coupling strength on the mechanical arms displacement. The parameters used in the system of equations (2.36) have been defined in the above section and we will consider $\ell = 4$ m and $L = 240$ mH.

3.4.1 Propagation of the signal and motion of the electromechanical arms

The set of discrete differential equations describes the propagation of electrical signal and the motion of N mechanical arms. To determine the propagation conditions, numerical solution is obtained using a fourth order Runge-Kutta algorithm with a time step $\Delta t = 10^{-3}$. The initial conditions are chosen as $v_n(0) = 0$, $w_n(0) = 0$, $x_n(0) = 0$, $\dot{x}_n(0) = 0$, $z_n(0) = 0$ and $u_n(0) = 0$ where $n = 1, 2, \cdots, N$. The boundary conditions are considered for the first and last nodes as $v_0 = v_1$, $v_{N+1} = v_N$. The excitation is performed with a constant current source applied just to the first cell, that is $I_{sn} = 0$ mA for $n \neq 1$.

We will first fix the stimulation current $I_{s1} = 10$ mA and analyze the effect of the coupling resistance R_c. After multiple simulations, we have found that the action potential is created in the first cell and propagates through the other cells for $18.7\ \Omega \leqslant R_c \leqslant 123.7\ \Omega$. Figure 3.19 displays the signals propagation in the discrete line and the behavior of the mobile beams when the action potential propagates in the line for $R_c = 20\ \Omega$.

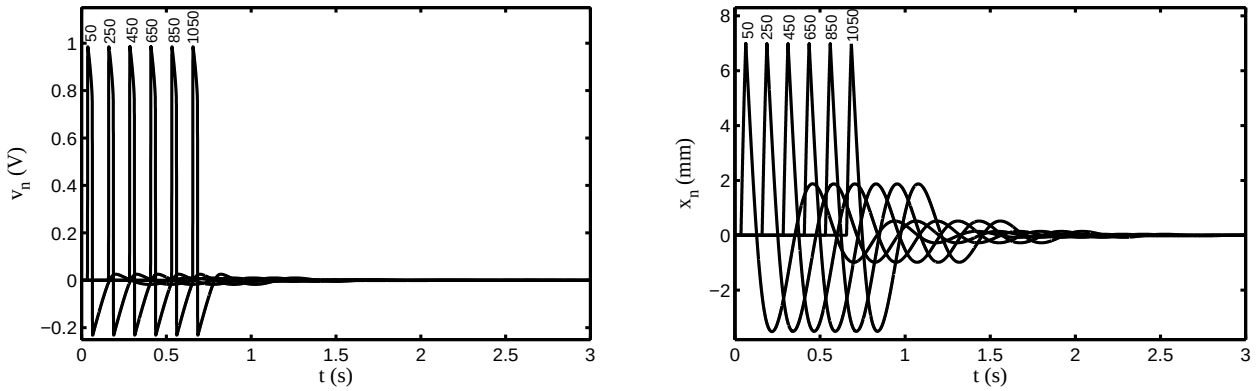

a) b)

Figure 3.19: Time evolution of the system at different cells for I_{s1}=10 mA and $R_c = 20\ \Omega$. a) Membrane potential v_n, b) Displacement of the mechanical arm x_n. The rang of the corresponding cell is indicated in each curve.

Figures 3.19a) and 3.19b) show respectively the propagation of the action potentials v_n and the displacement x_n of the mobile beams as a function of time for different cells such as $n = 50$, $n = 250$, $n = 450$, $n = 650$, $n = 850$, $n = 1050$. As shown in these Figures, the action potential shape is preserved during the propagation and each electromechanical subsystem exhibits a pulse-like behavior moving from its resting state, then increases to a maximal value and then decreases to the resting state. This observation is interesting since it indicates that the mobile beam executes an actuation work and then returns to its resting state. This profile is similar to the use of legs of artificial millipedes.

During our numerical investigations, we found that the traveling wave speed decreases as the coupling resistance increases. This fact is qualitatively in good agreement with the analytical expression of V_0 given in equation (2.39). For verification, the time evolution of the system at different cells is presented in Figure 3.20 for $R_c = 80\ \Omega$.

The graphs in Figures 3.19 and 3.20 are plotted for the same values of the parameters except that the first ones are plotted for $R_c = 20\ \Omega$ and the second ones for $R_c = 80\ \Omega$. We can notice that the traveling wave speed has decreased when the coupling resistance is increased from 20 Ω to 80 Ω. A part of that traveling wave speed, the curves of Figures 3.19 and 3.20 have the same

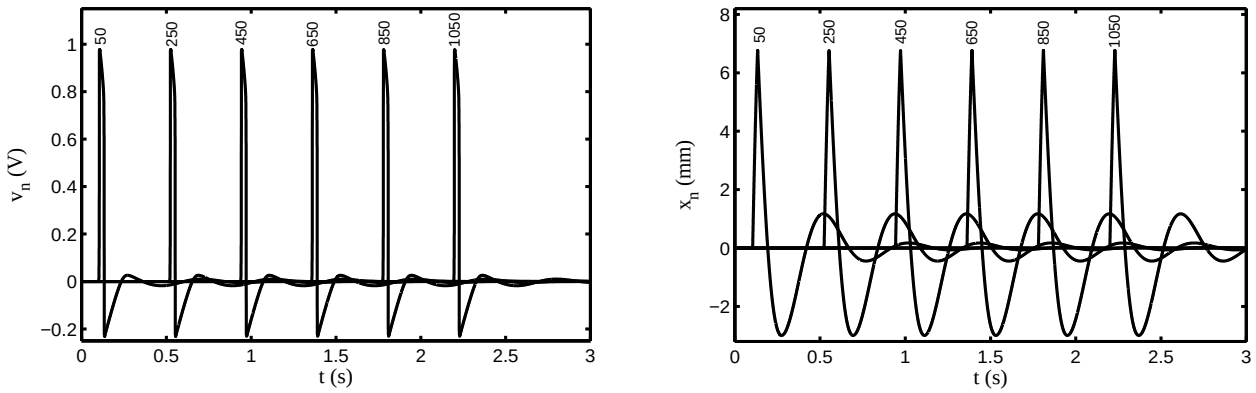

Figure 3.20: Time evolution of the system at different cells for I_{s1}=10 mA and $R_c = 80\ \Omega$. a) Membrane potential v_n, b) Displacement of the mechanical arm x_n. The rang of the corresponding cell is indicated in each curve.

behavior.

3.4.2 Effect of the stimulation current

We continue our investigations by analyzing the behavior of the discrete line when the stimulation current is increased to $I_{s1} = 25$ mA. We have then notice that, for certain values of the coupling resistance, an envelope of action potential propagates in the line. Our results plotted for $R_c = 100\ \Omega$ are shown in Figure 3.21.

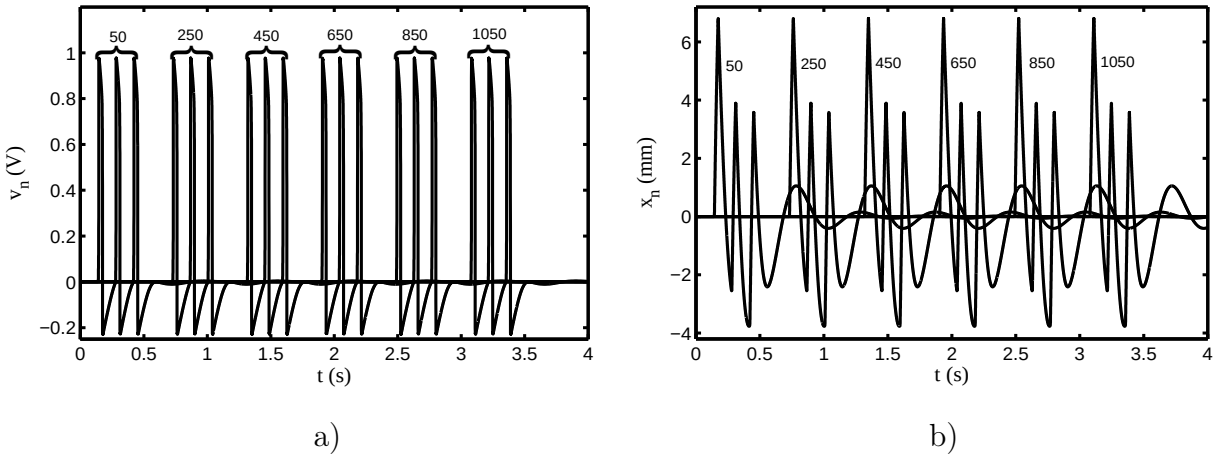

Figure 3.21: Time evolution of the system at different cells for I_{s1}=25 mA and $R_c = 100\ \Omega$. a) Membrane potential v_n, b) Displacement of the mechanical arm x_n. The rang of the corresponding cell is indicated in each curve.

Figure 3.21a) and Figure 3.21b) show respectively the behavior of the nonlinear electrical line and the behavior of some electromechanical systems for different cells such as $n = 50$, $n = 250$, $n = 450$, $n = 650$, $n = 850$, $n = 1050$. A packet of three action potentials is provided by the first cell and propagates through the line. Each mechanical arm exhibits a packet of three pulse-like behavior before returning to rest.

3.4.3 Space-time evolution of mechanical arms

Finally, we present respectively in figure 3.22a) and 3.22b) the spatiotemporal evolution of the mechanical arm and the spatiotemporal variation between displacements of the arm of nearest-neighbor defined as shift(t)=$x_i(t) - x_{i+1}(t)$.

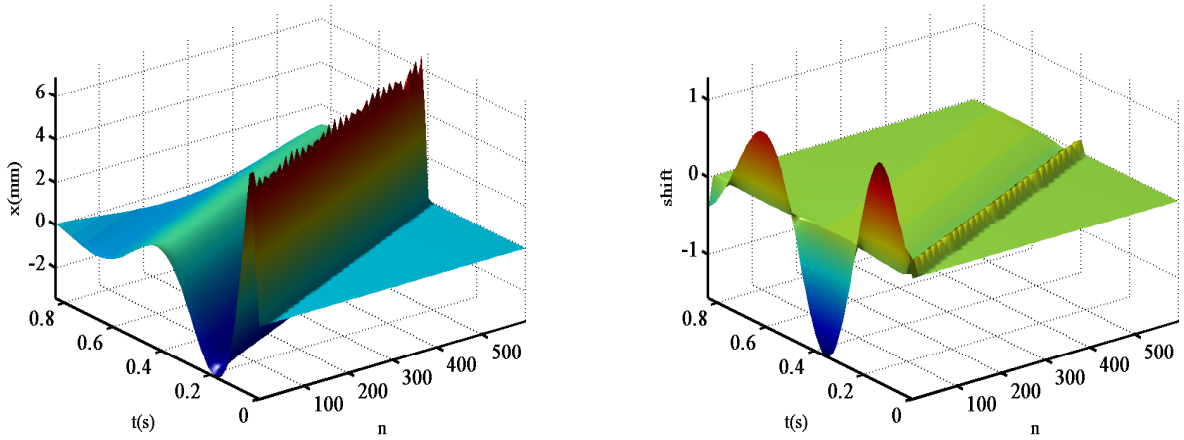

a) b)

Figure 3.22: a) Spatiotemporal evolution of the mechanical arm and b) spatiotemporal variation of dynamical shift.

3.5 EXPERIMENTAL RESULTS

We present in this section the experimental results obtained when an electromechanical arm is powered by a Fitzhugh-Nagumo neuron. The objective here is to verify if a Fitzhugh-Nagumo neuron model can be practicaly used to power an electromechanical arm. In this case, the used electromechanical arm is a loudspeaker with some specific parameters. The comparison between our theoretical results and the experimental ones are then given here.

3.5.1 Implementation of the nonlinear Fitzhugh-Nagumo resistance

In this subsection, we aim to implement the nonlinear Fitzhugh-Nagumo resistance. As mentioned in chapter 2, the smooth cubic $i - v$ characteristic of the nonlinear resistor of the circuit of Figure 2.2a) is given by the following equation:

$$i = \alpha v \left(v - \mu_1\right)\left(v - \mu_2\right), \tag{3.18}$$

where i and v are the current through and voltage across the nonlinear resistance respectively. μ_1, μ_2 and α are normalization parameters.

Our proposed circuit to simulate the nonlinear resistance is shown in Figure 3.23 using rectified diodes as nonlinear elements.

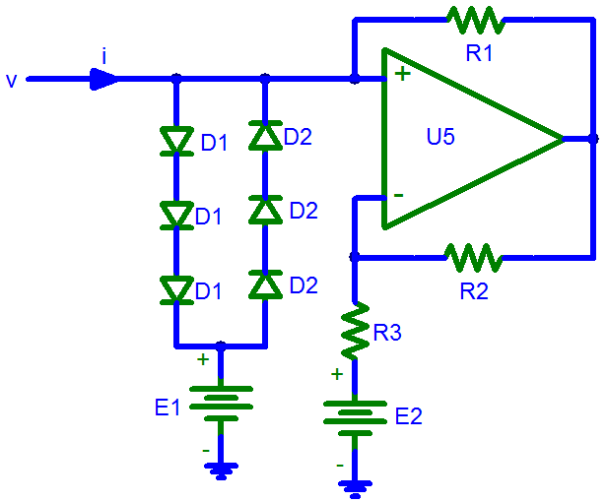

Figure 3.23: Equivalent circuit of the nonlinear Fitzhugh-Nagumo resistance.

The circuit of Figure 3.23 shows two blocks of three diodes connected in series. But in our analysis, we will consider a number of N_d diodes connected in series. We model the $i - v$ characteristic of diodes D_1 and D_2 with an exponential function, namely

$$i_d = I_0 \left[\exp\left(\frac{v_d}{V_0}\right) - 1\right], \tag{3.19}$$

where v_d is the voltage across the diode and i_d the current through. I_0 is the reverse saturation current and $V_0 = 65$ mV. Using the Kirchhoff laws and the above relation (3.19), it is found that the circuit in Figure 3.23 is described by the following equation:

$$i = 2I_0 \sinh\left(\frac{v - E_1}{N_d V_0}\right) - \frac{R_2}{R_1 R_3}(v - E_2). \tag{3.20}$$

For weak values of voltage v, and fixing the reversed saturation current I_0, the voltage sources E_1 and E_2 and the resistance R_3 as

$$I_0 = \alpha V_0^2 \sqrt{9V_0^2 - (\mu_1 + \mu_2)^2}, \tag{3.21}$$

$$E_1 = \frac{V_0}{2} \ln\left(\frac{3V_0 + \mu_1 + \mu_2}{3V_0 - \mu_1 - \mu_2}\right), \tag{3.22}$$

$$E_2 = \frac{2V_0^2 (\mu_1 + \mu_2)}{6V_0^2 - \mu_1\mu_2}, \tag{3.23}$$

$$R_3 = \frac{R_2}{\alpha R_1 (6V_0^2 - \mu_1\mu_2)}. \tag{3.24}$$

equation (3.20) gives the following current-voltage characteristic:

$$i = \alpha v (v - \mu_1)(v - \mu_2). \tag{3.25}$$

The current-voltage characteristic is represented in Figure 3.24a). It was obtained by experimental simulation on Pspice software and the values of the components used are as follows: $R_1 = 10\ \Omega$, $R_2 = 1000\ \Omega$, $R_3 = 41.75\ \Omega$, $E_1 = 435.14$ mV, $E_2 = 402.21$ mV and a rectified diode of type IN4007. For comparison, the analytical result obtained by representing the relation (3.25) is given in Figure 3.24b).

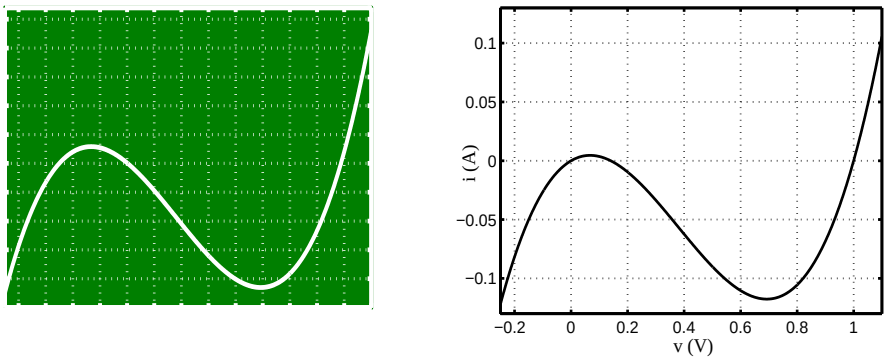

a) b)

Figure 3.24: Current-voltage- characteristic of nonlinear Fitzhugh-Nagumo resistance. a) Pspice simulation obtained, b) numerical plot

As revealed by the curves of Figure 3.24, a good agreement is found between the theoretical and experimental current-voltage characteristics, specially in the case where voltage has small values. The point is that such a resistor can take both positive and negative values according to the characteristics of the signal. This element acts like a normal resistor when the voltage is high, but acts like a negative resistor if the voltage is low. Therefore the circuit pumps up small oscillations (negative resistor effect) and drags down large oscillations (normal resistor effect).

3.5.2 The experimental set-up.

The circuit was built according to the complete scheme shown in Figure 3.25 using (LF356) operational amplifiers, (IN4007) diodes, resistors, inductors and capacitors.

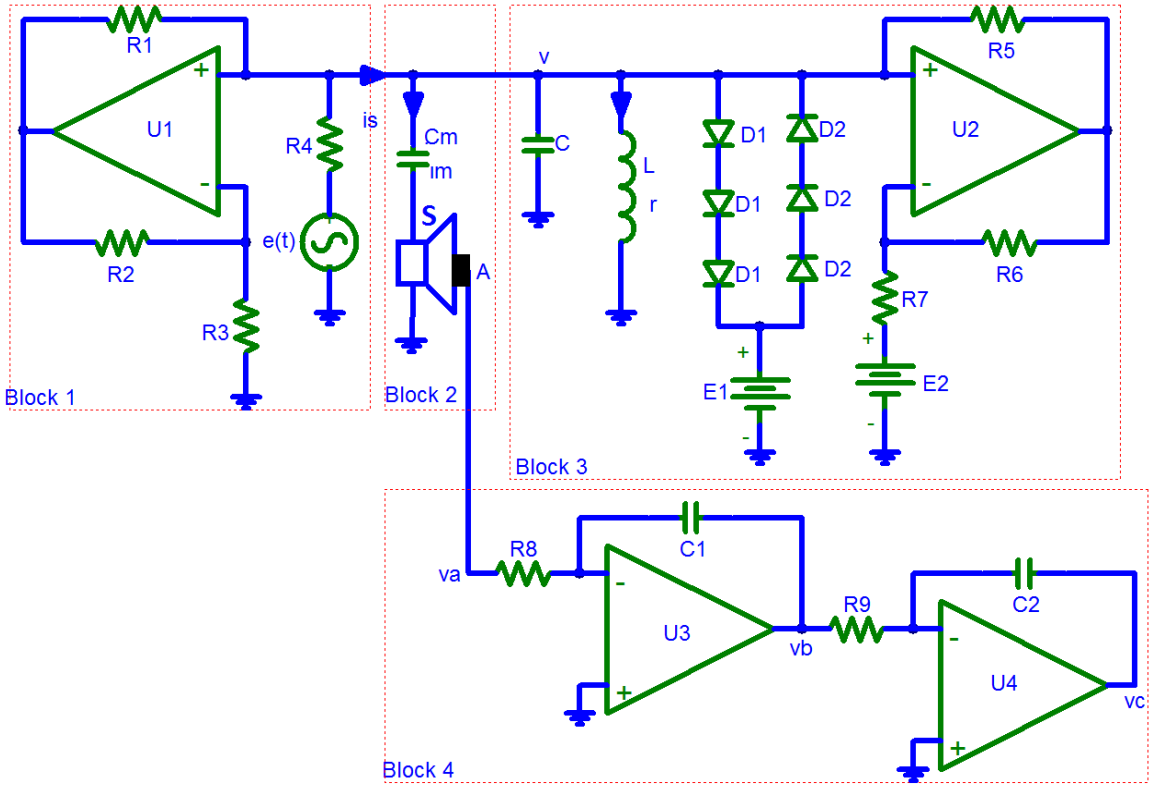

Figure 3.25: Complete circuit diagram of the Fitzhugh-Nagumo neuron coupled magnetically to a mechanical arm and forced with a current source.

The overall circuit of the system presents four different blocks. The first block named **Block 1** is our voltage to current converter circuit. **Block 2** represents the mechanical subsystem, while **Block 3** and **Block 4** represent respectively the Fitzhugh-Nagumo neuron and the integrator network. **S** is the electrodynamic loudspeaker and represents our mechanical arm. The internal inductance and the corresponding series internal resistance are respectively L_m and r_m. The membrane and the spider of the loudspeaker have an equivalent spring constant K. An shown in the diagram, an accelerometer **A** is fixed on the membrane of the loudspeaker to measure the acceleration $v_a = f_1(\ddot{x})$ of its movement. A cascade of two integrator circuits is connected at the output of the accelerometer to determine respectively the velocity $v_b = f_2(\dot{x})$ and the position $v_c = f_3(x)$ of the membrane as a function of time. To well observe $\dot{x}$ and x, the parameters of each have been chosen in such a way that at the resonant radian frequency,

we have $R_8C_1\omega_0 \simeq 1$ and $R_9C_2\omega_0 \simeq 1$.

An experimental setup consisting of the Fitzhugh-Nagumo neuron coupled magnetically to a mechanical arm (speaker) is shown in Figure 3.26.

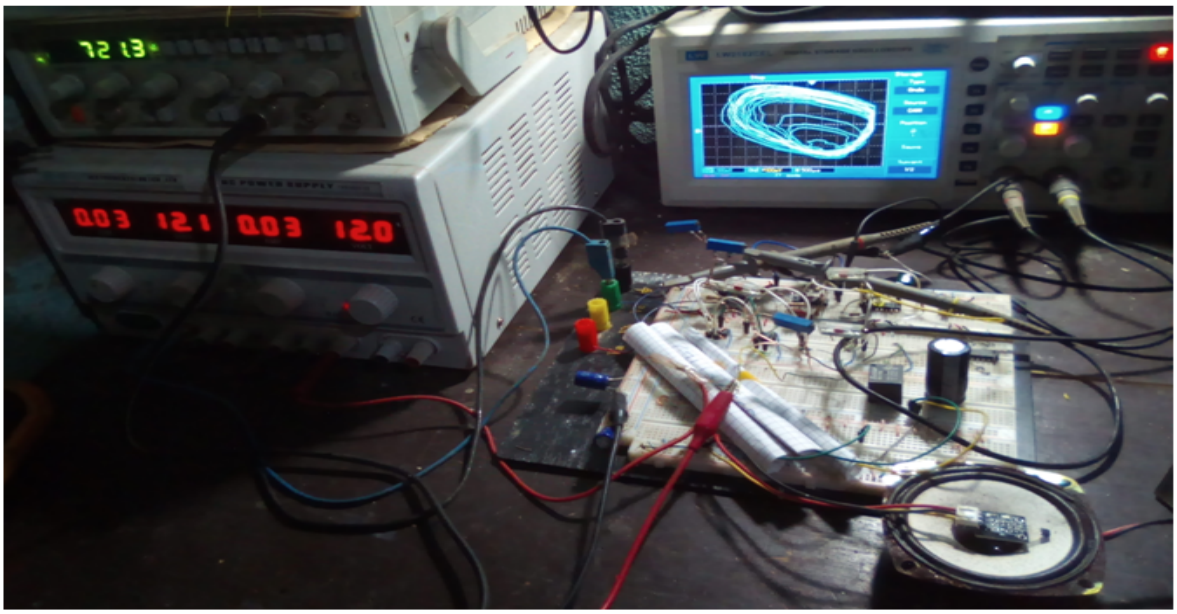

Figure 3.26: Complete experimental setup of the Fitzhugh-Nagumo neuron coupled magnetically to a mechanical arm.

To occupy less space, the ten diodes of each block are packed inside the isolated paper as shown on the picture. The power supply is used as polarization voltage of the operational amplifiers. The digital oscilloscope allows immediate viewing of the time series and phase space plots of the membrane motion. The values of all the parameters are given in Table 3.2.

Parameters	Values	Parameters	Values	Parameters	Values
U_1, U_2, U_3, U_4,	LF356	Diodes	IN4007	R_1	10 Ω
R_2	1000 Ω	R_3	41.75 Ω	R_4	10 Ω
R_5	922.19 Ω	R_6	1.66 Ω	R_7	3.25 Ω
r	2.5 Ω	L	7 mH, 240 mH	L_m	40.58 mH
r_m	7.5 Ω	C	60 μF	C_m	4700 μF
E_1	435.14 mV	E_2	402.21 mV	N_d	10
$B\ell$	0.2 Tm	K	10 N/m	B	0.8 T

Table 3.2: Values of the physical parameters used in the circuit of Figure 3.25.

3.5.3 System forced by a DC source

In this case, the input voltage source is a constant voltage source as $e(t) = E$ and $L = 240$ mH. The relation between the numerical parameter and the experimental one is given as $E = R_4 I_s$. In this subsection, we aim to visualize the dynamical behavior of the system as the experimental control parameter E increases from 0 V up to 5 V.

We found during our experimental investigations that the system oscillates for 0.8 V $\leqslant E \leqslant$ 4.6 V. To verify this result, we have consider the following three values of the control parameter E: $E = 0.5$ V, $E = 1.5$ V and $E = 5$ V. The corresponding time series of the membrane potential and the mechanical displacement of the membrane are plotted respectively in Figure 3.27, Figure 3.28 and Figure 3.29.

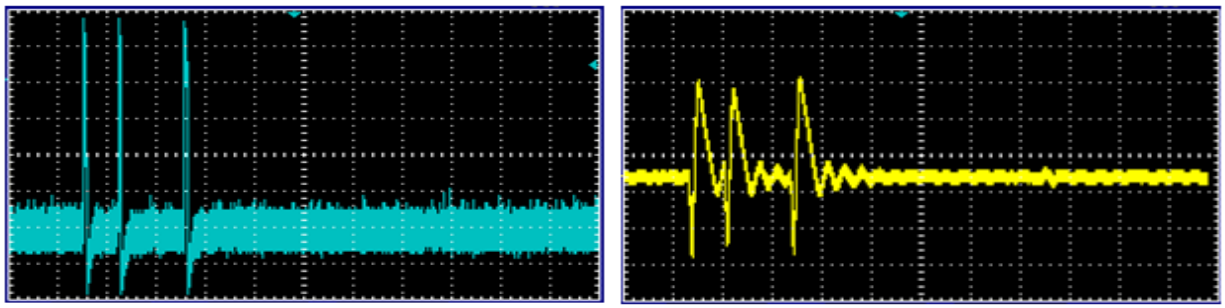

a) b)

Figure 3.27: Time series of the system for $E = 0.5$ V. a) membrane potential v and b) mechanical displacement x.

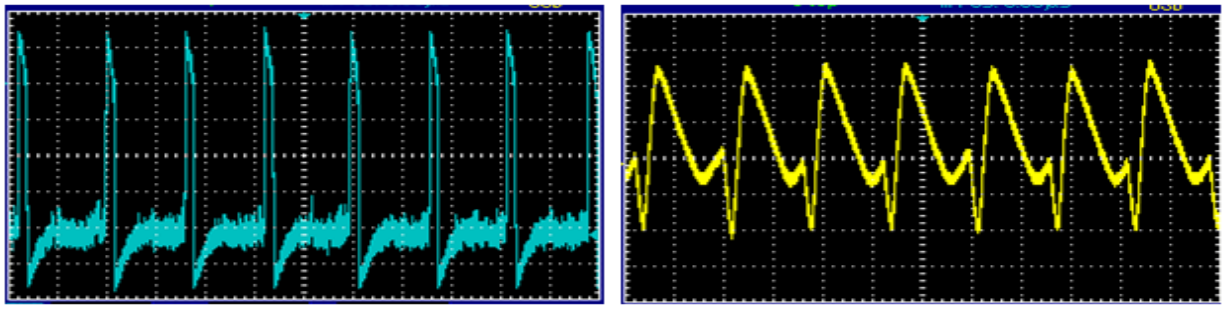

a) b)

Figure 3.28: Time series of the system for $E = 1.5$ V. a) membrane potential v and b) mechanical displacement x.

When the input voltage is less than 0.8 V or greater than 4.6 V, the system converges toward the single stable equilibrium point. Otherwise, if the control voltage is between 0.8 V

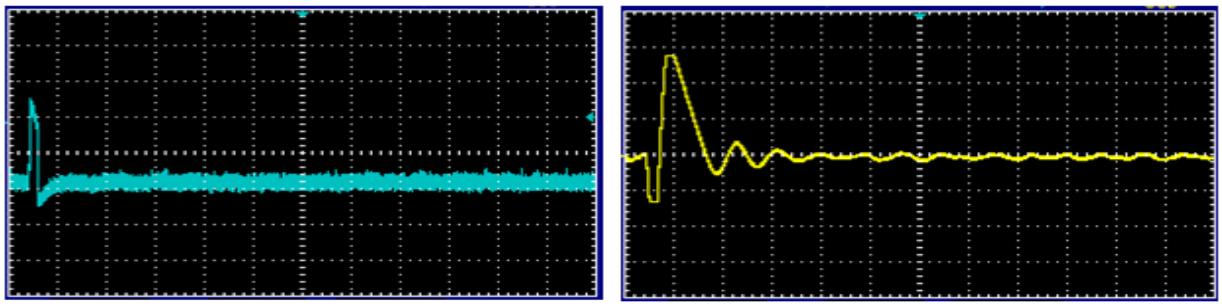

a) b)

Figure 3.29: Time series of the system for $E = 5.0$ V. a) membrane potential v and b) mechanical displacement x.

and 4.6 V, the system under analysis provides oscillating signals. The frequency of the signal presented in the graph of 3.28)a) and 3.28b) is 8.57 Hz.

Even if we have not succeeded to determine some experimental parameters of the system such as the magnetic field intensity B, the length of the conductor winding in the magnetic filed ℓ and the damping coefficient β, we can find good qualitative agreements between the numerical results presented in Figure 3.12 and Figure 3.13, and the experimental ones given in Figure 3.27, Figure 3.28 and Figure 3.29.

3.5.4 System forced by a series combination of DC and AC sources

We aim is this subsection to verify if the chaotic state obtained in subsection 3.3.6 can be confirmed experimentally. For that purpose, the inductance L equals 7.0 mH and the input voltage is a series combination of the DC and AC sources as $e(t) = E + E_m \sin\left(\frac{2\pi f}{\omega_0} t\right)$. The relation between the experimental parameters and the numerical ones are given as $E = R_4 I_s$ and $E_m = R_4 I_m$.

The experimental investigations of the systems showed that it can also exhibit regular and irregular behaviors. To illustrate the chaotic behavior of the system, we choose $E = 0.2$ V and $E_m = 1.0$ V and the phase portrait of the electrical subsystem is shown in Figure 3.30a) while the phase portrait of the mechanical subsystem is presented in Figure 3.30b).

The experimental frequency of the alternating source if $f = 721$ Hz. As revealed by the graphs, the chaotic state of the system is confirmed by the experimental results. Nevertheless, the chaotic signatures of the experimental results and the chaotic signatures of the theoretical results shown in Figure 3.18 are different, explained by the fact that the parameters used in experiment are not precisely those used theoretically. However, according to the periodicity,

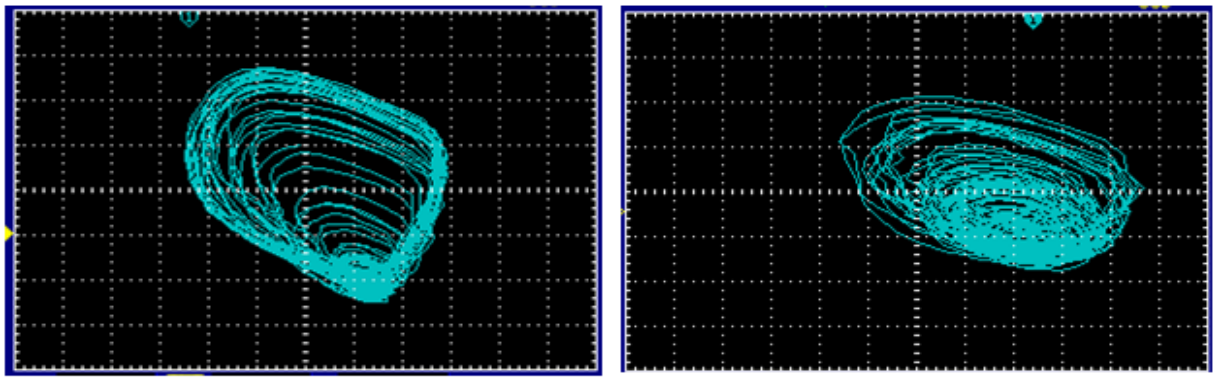

a) b)

Figure 3.30: Phase portraits when $E = 0.2$ V, and $E_m = 1.0$ V. a) w versus v and b) $\dot{x}$ versus x

they are confirmed quantitatively very well by the developed mathematical model and its numerical simulations.

Conclusion

This chapter has presented and discussed the principal results obtained in this thesis. The effects on input current on a single and an array of nanoelectromechanical beam driven by a single and an array of Josephson junction are given. It appears that each nanobaem coupled a each node of an array of coupled Josephson junction deliver a pulse like motion. Indeed, we have noticed the effect of magnetic field on the amplitude of the beam. We have also analyzed the effects of some parameters on the system concerning the case of a single device and the case of an array devices. The experimental results are finally presented and the comparisons with the theoretical results are given.

GENERAL CONCLUSION AND PERSPECTIVES

GENERAL CONCLUSION

The dynamics of electromechanical devices powered by nonlinear electrical transmission lines have been investigated theoretically and experimentally. We have first presented some generalities on networks of electromechanical systems. We have also presented discrete Josephson junction transmission lines and Fitzhugh-Nagumo neuron.

Secondly, we have analyzed the dynamical behavior of a single nano-beam powered by a Josephson junction and an array of nano-beams coupled to an array of discrete coupled Josephson junctions. It has been demonstrated that a nano-beam powered by a Josephson junction can deliver periodic vibration when a critical value of the DC bias current powering the junction is attained. The amplitude of the beam vibration increases with the DC bias current. In the case of an array of discrete Josephson junctions having a nano-beam at each node, it has been seen that when the topological soliton (antikink) propagates in the discrete line, each beam exhibits a pulse-like behavior whose amplitude increases with the magnitude of the magnetic field. Because of the periodic boundary conditions and the fact that the antikink velocity is proportional to the DC bias current, one observes that each nano-beam periodically executes pulse-like displacement shape. The period of vibration of the beam decreases when the DC bias current increases while the amplitude of the pulse-like nano-beam displacement increases with the DC bias current. This constitutes an interesting dynamical electromechanical system which can be used in nano-actuation processes.

We have thirdly analyzed theoretically and experimentally the dynamics of one single Fitzhugh-Nagumo neuron coupled to a mechanical arm. In the theoretical case, we have presented the oscillation boundaries where we have shown that for certain values of stimulation current, the system can converge towards the equilibrium point and for other values, the system can fall in oscillation or display a limit cycle behavior. The oscillation frequency and the oscillation conditions were determined. Forward period-doubling bifurcation sequences followed by reverse period-doubling sequences, as a parameter is varied in a monotone way, antimonotonic-

ity is observed in the system. During our experimental investigations, when we have forced our system by a *DC* source, we have found that the system oscillates with a frequency for certain values of experimental control parameter and converges toward the single stable equilibrium point for other values. Furthermore, the experimental study has showed chaotic behavior when we forced the system by a series combination of *DC* and *AC* sources. The comparison between theoretical and experimental results has revealed a good qualitative agreements when the input voltage source is a constant. Nevertheless, they are different when the input voltage is a series combination of the *DC* and *AC* sources. That has been explained by the fact the parameters which have been used in experiment are not precisely those which have been used theoretically. Finally, the investigations of an array of electromechanical arms powered by an array of discrete excitable Fitzhugh-Nagumo have been done. When the first cell is excited, the nerve impulse propagates in the electrical line, and each mechanical arm displays a pulse-like behavior. It was found that the train of three pulses can also propagate through the line according to the coupling strength.

PERSPECTIVES

This work has opened interesting perspectives for future investigations:

− It would be interesting to study experimentally a single electromechanical system and an array of electromechanical systems constituted of a series of coupled discrete Josephson junction/ Fitzhugh-Nagumo neurons with a nanobeam/rigid arm placed at each node.

− It would be interesting to investigate later the study of the control of electromechanical legs when those are in a wet environment.

− It would be interesting to investigate later the study on the rotational movement of the legs.

Bibliography

[1] M. Darula, T. Doderer and S. Beuven, Millimetre and sub-mm wavelength radiation sources based on discrete Josephson junction arrays, Supercond. Sci. Technol., **12**, PP. R1-R25, (1999).

[2] G. Filatrella, N. F. Perdersen, C. J. Lobb and P. Barbara, Synchronization of underdamped Josephson-junction arrays, Eur. Phys. J. B **34**, PP. 3-8, (2003).

[3] A. Uchida, H. Iida, N. Maki, M. Osawa and S. Yoshimori, Chaotic oscillations in Josephson tetrode, IEEE Trans. Applied Supercond. **14**, PP. 2064-2070, (2004).

[4] R. Kleiner, P. Muller, H. Kohlstedt, N. F. Pedersen and S. Sakai, Dynamic behavior of Josephson-coupled layered structures, Phys. Rev. B, **50**, PP. 3942-3952, (1994).

[5] D. Dominguez and H. A. Cerdeira, Order and turbulence in rf-driven Josephson junction series arrays, Phys. Rev. Lett., **71**, PP. 3359-3362, (1993).

[6] K. K. Likharev, Dynamics of Josephson junctions and Circuits-Gordon and Breach Science Publishers, New-York, (1986).

[7] J. Cosp, S. Binczak, J. Madrenas and D. Fernandez, Realistic model of compact VLSI FitzHughŰNagumo oscillators, Inter. J. Electr., **101**, PP. 220-230, (2013).

[8] M. Armanyos and A. G. Radwan, 13th International Conference on Electrical Engineering/Electronics, Computer Telecommunications and information Technology (2016).

[9] J. P. Keener, Analog circuitry for the van der Pol and FitzHugh-Nagumo equations, IEEE Trans. Syst. Man. Cybern., **13**, PP. 1010-1014, (1983).

[10] J. G. Alford, Models of unidirectional propagation in heterogeneous excitable media, Applied Maths. Comput., **216**, PP. 1337-1348, (2010).

[11] A. Cattani, FitzHugh-Nagumo equations with generalized diffusive coupling, Maths. Biosciences $\propto$ Engin., **11**, PP. 203-215, (2014).

[12] J. G. Ojalvo, R. Bascones, F. Sagues, J. M. Sancho and L. S. Geier, Pulse Propagation in Bistable Neural Models via noise induced resetting ,AIP Conference Proc., **665**, PP. 35-42, (2003).

[13] D. L. Sekulic, M. V. Sataric, M. B. Zivanov and J. S. Bajic, Soliton-like Pulses along Electrical Nonlinear Transmission Line, Electron. Electric. Engin., **121**, PP. 53-58, (2012).

[14] M. Nguimdo, S. Noubissie and P. Woafo, Waves amplification in discrete nonlinear electrical lines: direct numerical simulation, J. Phys. Soc. Jpn., **77**, PP. 124006-1240010, (2008).

[15] F. Kenmogne and D. Yemélé, Exotic modulated signals in a nonlinear electrical transmission line: Modulated peak solitary wave and gray compacton, Chaos Solitons Fract., 45, PP. 21-34, (2012).

[16] F. B. Pelap, J. H. Kamga, S. B. Yamgoue, S. M. Ngounou and J. E. Ndecfo, Dynamics and properties of waves in a modified Noguchi electrical transmission line Phys. Rev. E, **91**, PP. 022925-022934, (2015).

[17] T. Kuusela, J. Hietarinta, K. Kokko and R. Laiho, Soliton experiments in a nonlinear electrical transmission line, Eur. J. Phys., **8**, PP. 27-33, (1987).

[18] A. Mboussi Nkomidio, S. Noubissie and P. Woafo, Dynamics of arrays of legs powered by a discrete electrical model of nerve, Phys. Lett. A, **378**, PP. 857-862, (2014).

[19] N. Vogt, R. Schafer, H. Rotzinger, W. Cui, A. Feibig, A. Shairman and A. V. Ustinov, One-dimensional Josephson junction arrays: Lifting the Coulomb blockade by depinning, Phys. Rev. B, **92**, PP. 045435-0454312, (2015).

[20] V. K. Kaplumenko, J. Mygind, N. F. Pedersen and A. V. Ustinov, Radiation detection from phase-locked serial dc SQUID arrays, J. Applied. Phys., **73**, PP. 2019-2023, (1993).

[21] B. H. Larsen and S. P. Benz, Stable phase locking in a two-cell ladder array of Josephson junctions, Appl. Phys. Lett., **66**, PP. 3209-3211, (1995).

[22] Y. Braiman, W. L. Ditto, K. Wiesenfeld and M. L. Spano, Disorder-enhanced synchronization, Phys. Lett. A, **206**, PP. 54-60, (1995).

[23] C. B. Whan, A. B. Cawthorne and C. J. Lobb, Synchronization and phase locking in two-dimensional arrays of Josephson junctions, Phys. Rev. B, **53**, PP. 12340-12345, (1996).

[24] S. Z. Lin, X. Hu and L. Bulaevsku, Synchronization in a one-dimensional array of point Josephson junctions coupled to a common load, Phys. Rev. B, **84**, PP. 104501-1045012, (2011).

[25] G. Fautso Kuiate and P. Woafo, Fiske and Satellite Steps in a Twofold Stack Josephson Junction, Physica. Scr., **71**, PP. 556- 560, (2005).

[26] G. Fautso Kuiate and P. Woafo, IŰV Characteristics of an array of discrete Josephson junction and effect of a localized defect, Physica C, **440**, PP. 59-65, (2006).

[27] Z. Zheng and M. C. Cross, Defect-induced propagation, Internat. J. Bifur. Chaos, **13**, PP. 3125-3133, (2003).

[28] C. E. Elmer and E. S. Van Vleck, Spatially discrete Fitzhugh-Nagumo equations, Siam J. Appl. Math., **65**, PP. 1153-1174, (2005).

[29] Y. Klofa$\ddot{i}$, B. Z. Essimbi and D. J*ä*ger, An MMIC implementation of Fitzhugh-Nagumo neurons using a resonant tunneling diode nonlinear transmission line, Phys. Scr. **90**, PP. 025002-025007, (2015).

[30] J. P. Keener, Propagation and its failure in coupled systems of discrete excitable cells, Siam J. Appl. Math., **47**, PP. 556-572, (1987).

[31] S. P. Hopkin and H.J. Read, The Biology of millipedes, Oxford University Press, Oxford, (1992).

[32] J. G. E. Lewis, The biology of Centipedes, Cambridge University press, Cambridge, (1981).

[33] H. Simo and P. Woafo, Bursting oscillations in electromechanical systems, Mechanics Research Commun., **38**, PP. 537-541, (2011).

[34] V. Y. Taffoti Yolong and P. Woafo, The complete synchronization condition in a network of piezoelectric micro-beams, Nonlinear Dyn., **57**, PP. 261-274, (2009).

[35] K. Chembo Kouomou and P. Woafo, Stability and chaos control in electrostatic tranducers, Physica Scripta, **62**, PP. 255-260, (2000).

[36] C. A. Kitio Kwuimy and P. Woafo, Experimental realization and simulations a self-sustained macro electromechanical system, Mechanics Research commun., **37**, PP. 106-110, (2010).

[37] U. Simo Domguia, L. T. Abobda and P. Woafo, Dynamical behavior of a capacitive microelectromechanical system powered by a Hindmarsh-Rose electronic oscillator, J. Comput. Nonlinear Dyn., 11, PP. 051006-051013, (2016).

[38] M. P. Blencowe, Nanoelectromechanical systems, Comtemp. Phys., **46**, PP. 249-264, (2005).

[39] J. B. Mogo and P. Woafo, Dynamics of a cantilever arm actuated by a nonlinear electrical circuit, Nonlinear Dyn., **63**, PP. 807-818, (2011).

[40] J. C. Chedjou, P. Woafo and S. Domngang, Shilnikov chaos and dynamics of a self-sustained electromechanical transducer. J. Vibrat. Acoust., **123**, PP. 170-174, (2001).

[41] C. A. Kitio Kwuimy, B. Nana and P. Woafo, Experimental bifurcations and chaos in a modified self-sustained macroelectromechanical system, J. Sound Vibrat., **329**, PP. 3137-3148, (2010).

[42] C. A. Kitio Kwuimy and P. Woafo, Modeling and dynamics of a self-sustained electrostatic microelectromechanical system, J. Comput. Nonlinear Dyn., 5, PP. 021010-021017, (2010).

[43] R. Yamapi and P. Woafo, Dynamics and synchronization of coupled self-sustained electromechanical devices, J. Sound Vibrat., **285**, PP. 1151-1170, (2005).

[44] R. Yamapi, Dynamics of an electromechanical damping device with magnetic coupling, Commun. Nonlinear Sci. Numer. Simulat., **11**, PP. 907-921, (2006).

[45] R. Yamapi, J. B. Chabi Orou and P. Woafo, Harmonic Dynamics and transition to chaos in a nonlinear electromechanical system with parametric coupling, Physica Scripta, **67**, PP. 269-275, (2003).

[46] R. Yamapi, J. B. Chabi Orou and P. Woafo, Harmonic oscillations, stability and chaos control in a nonlinear electromechanical system, J. Sound Vibrat., **259**, PP. 1253-1264, (2003).

[47] R. Yamapi and S. Bowong, Dynamics and chaos control of the self sustained electromechanical device with and without discontinuity, commun. Nonlinear Sci. Numer. Simulat., **11**, PP. 355-375, (2006).

[48] G. S. Mbouna Ngueuteu and P. Woafo, Dynamics and synchronization analysis of coupled fractional order nonlinear electromechanical systems, Mechanics Research Commun., **46**, PP. 20-25, (2012).

[49] M. G. Rosemblum and A. S. Pikovsky, controlling synchronization in an ensemble of globally coupled oscillators, Phys. Rev. Lett., **92**, PP. 114102-114106, (2004).

[50] P. AShwin, O. Burylko, Y. Maistrenko and O. Popvych, Extreme sensitivily to deturning for globally coupled phase oscillators, Phys. Rev. Lett., **96**, PP. 114102-114106, (2004).

[51] V. Anishchenko, S. Astakhov and T. Vadivasova, Phase dynamics of two coupled oscillators under external periodic force. Europhys. Lett., 86, PP. 30003-P1-30003-P5, (2009).

[52] J. Simonovic, Synchronization in coupled systems with different type of coupling elements, Differ Equ Dyn Syst **21**, PP. 141-148, (2013).

[53] G. S. Mbouna Ngueuteu, R. Yamapi and P. Woafo, Stability of synchronized network of chaotic electromechanical devices with nearest and all-to-all couplings, J. Sound Vibrat., **318**, PP. 1119-1138, (2008).

[54] R. Yamapi and P. Woafo, Synchronized states in a ring of four mutually coupled self-sustained electromechanical devices, Commun. Nonlinear Sci. Numer. Simulat., **11**, PP. 186-202, (2006).

[55] V. Y. Taffoti Fondjo and P. Woafo, Synchronization in a ring of mutually coupled electromechanical devices, Physica Scripta, **74**, PP. 591-598, (2006).

[56] M. V. Tchakui, V. Y. Taffoti Fondjo and P. Woafo, Bifurcation structured in three unidirectionally coupled electromechanical systems with no external signal and with regeneratrice process, nonlinear Dyn., **84**, PP. 1961-1972, (2016).

[57] G. S. Mbouna Ngueuteu, Rings and networks of elelctromechanical systems, PhD. Thesis, Faculty of science, University of Yaoundé 1, Cameroon (2014).

[58] M. V. Tchakui, Complex behaviors, signal propagation and amplification in chaos of autonomous electromechanical systems with unidirectional coupling, P.h.D. Thesis, Faculty of science, University of Yaoundé 1, Cameroon (2019).

[59] M. V. Tchakui, P. Woafo and P. Colet, Signal bi-amplification in networks of unidirectionally coupled MEMS, Eur. Phys. J. B, **89**, PP. 1-9, (2016).

[60] R. Hirota and K. Suziki, Studies on lattice solitons by using electrical networks, J. Phys. Soc. Jpn., **28**, pp. 1366-1367, (1970).

[61] M. Toda, wave propagation in anharmonic lattices, J. Phys. Soc. Jpn., **23**, pp. 501-506, (1967).

[62] P. Marque, J. M. Bilbault and M. Remoissenet, Generation of envelope and hole solitons in an experimental transmission line, Phys. Rev. E, **49**, pp. 828-835, (1994).

[63] D. Yemélé, P. Marquié and J. Marie Bilbault, long time dynamics of modulated waves in a nonlinear discrete LC Transmission line, Phys. Rev. E, **68**, pp. 016605-016615, (2003).

[64] L. Q. English, R. Basu Thakur and R. Stearrett, Patterns of traveling intrinsic localized modes in a driven electrical lattice, Phys. Rev. E, **77**, pp. 066601-066605, (2008).

[65] B. Z. Essimbi and I. V. Barashenkov, Spatially localized voltage oscillations in an electrical lattice, J. Phys. D: Appl. Phys., **35**, pp. 1438-1441, (2002).

[66] L. Leon and M. Manna, Discrete instability in nonlinear lattices, Phys. Rev. Lett., **83**, pp. 2324-2327, (1999).

[67] F. Ndzana, A. Mohamadou, T. C. Kofané, Modulational instability in the cubic quintic nonlinear Schrödinger equation through the variational approach, J. Phys., **40**, pp. 3254-3262, (2007).

[68] H. Nagashima and Y. Amagashi, Experiment on the Toda lattice using nonlinear transmission lines, J. Phys. Soc. Jpn., **45**, pp. 680-688, (1978).

[69] K. Muroya, N. Saitoh and S. Watanabe, Experiment on lattice soliton by nonlinear LC Circuitobservation of a dark soliton, J. Phys. Soc. Jpn., **51**, pp. 1024-1029, (1982).

[70] E. Kengne, B. A. Malomed, S. T. Chui and W. M. Liu, Solitary signals in electrical nonlinear transmission line, J. Maths. Phys., **48**, pp. 013508-0135013, (2007).

[71] P. Marquie, J. M. Bilbault and M. Remoissenet, Generation of enveloppe and hole solitons in an experimental transmission line, Phys. Rev. E, **49**, pp. 828-835, (1994).

[72] J. M. Bilbault, P. Marquié and B. Michaux, Modulational instability of two counter-propagating waves in an experimental transmission line, Phys. Rev. E, **51**, pp. 817-820, (1995).

[73] D. L. Sekulic, M. V. Sataric, M. B. Zivanov and J. B. Bajic, Soliton-like pulse along electrical nonlinear transmission lines electron, Electric. Engin., **121**, pp. 53-58, (2012).

[74] F. Kenmogne and D. Yemélé, Exotic modulated peak solitary wave and gray compacton, Chaos, Solitons and Fractals, **45**, pp. 21-34, (2012).

[75] M. Remoissenet, waves called solitons, Springer-Verlag, Berlin, (1999).

[76] M. G. Case, Nonlinear transmission lines for picosecond pulse, Impulse and millimeter wave harmonic generation, Santa Barbara: University of California, (1993).

[77] D.S. Ricketts, X. Li and D. Ham, Electrical soliton oscillator, IEEE Trans. Microw. Theory Tech., **54**, pp. 373-382, (2006).

[78] D. Ham, X. Li, S. A. Denenberg, T. H. Lee and D. S. Ricketts, Ordered and chaotic electrical solitons: Communication perspectives, IEEE Communicat. Magaz., **44**, pp. 126-135, (2006).

[79] M. V. Sataric, N. Bednar, B. MO Sataric and G. Stofanovic, Actin filaments as nonlinear RLC transmission lines, Inter. J. Modern. Phys. B, **23**, pp. 4697-4711, (2009).

[80] E. Afshari and A. Hajimiri, Nonlinear transmission lines for pulse shaping in silicon, IEEE J. Solid-State Circuits, **40**, pp. 744-752, (2005).

[81] E. Kengne and W. M. Liu, Exact solutions of the derivative nonlinear *Schrödinger* equation for a nonlinear transmission line, Phys. Rev. E, **73**, pp. 026603-0266010, (2006).

[82] A. Houwe, M. Justin, D. Jerome, G. Betchewe, S. Y. Doka and T. C. Kofané, Wave propagation of the perturbed nonlinear *Schrödinger* equation in the nonlinear left-handed transmission line, Asian Europ. J. Maths., **12**, pp. 2050035-2050048, (2020).

[83] T. Kuusela, J. Hietarinta, K. Kokko and R. Laiho, Soliton experiments in a nonlinear electrical transmission line, Eur. J. Phys., **8**, pp. 27-33, (1987).

[84] S. Abdoulkary, L. Q. English and A. Mohamadou, Envelope solitons in a left-handed nonlinear transmission line with Josephson Junction, Chaos, Solitons and Fractals, **85**, pp. 44-50, (2016).

[85] M. J. Rempe and D. L. Chop, A predictor-corrector algorithm for reaction diffusion equations associated with neural activity on branched strucrures, Siam. J. Sci. Comput., **28**, pp. 2139-2161, (2006).

[86] C. Zhang and A. Ke, B. Zheng, Patterns of interaction of coupled reaction-diffusion systems of the Fitzhugh-Nagumo type, Nonlinear Dyn., **97**, pp. 1451-1476, (2019).

[87] K. Keplinger and R. Wacherbauer, Transient spatiotemporal chaos in the Morris-Lecar ring network, Chaos Interdisci. J. Nonlinear Science, **24**, pp. 013126-0131215, (2014).

[88] B. D. Josephson, possible new effects in superconductive tunnelling, Phys. Lett., **1**, pp. 251-253, (1962).

[89] J. R. Anderson and J. M. Rowell. probable Observation of the Josephson superconducting tunnel effect, Phys. Rev. Lett., 10, pp. 230-232, (1963).

[90] R. L. Kautz, Noise, chaos, and the Josephson voltage standard, Rep. Prog. Phys., **59**, pp. 935-992, (1996).

[91] K. K. Likharev, Superconducting weak links, Rev. of modern Phys., **51**, pp. 101-159, (1979).

[92] A. Ergul, Nonlinear dynamics of Josephson junction chains and superconducting resonators, Stockholm, Sweden, (2013).

[93] M. Tinkham, Introduction to superconductivity, new york, 2nd edition, (1996).

[94] L. Yu, R. Gandikota, R. K. Singh, L. Gu, D. J. Smith, X. Meng, X. Zeng, T. V. Duzer, J. M. Rowell and N. Newman, Internally shunted Josephsons with barriers tuned near the metal insulator transition for RSFQ logic applications, Supercond. Sci. Technol., **19**, pp. 719-731, (2006).

[95] K. K. Likharev, Dynamics of Josephson junctions and Circuits, New york, Gordon and Breach Science, (1986).

[96] A. Barone and G. Paterno, Physics and aplications of the Josephson effect, New york, John Wiley and Sons, (1982).

[97] C. B. Whan and C. J. Lobb, effect of inductance in externally shunted Josephson tunnel junctions, J. Appl. Phys., **77**, PP. 382-389, (1995).

[98] Y. Lei and R. Fu, Heteroclinic chaos in a Josephson junction system perturbed by dichotomous noise excitation, Lett. J. Exp., **112**, PP. 60005-600013, (2015).

[99] S. K. Dana, D. C. Sengupta and K. D. Edoh, Chaotic dynamics in Josephson junction, IEEE Trans. Circuits Syst., **48**, PP. 990-996, (2001).

[100] E. M. Shahverdiev, L. H. Hashimova, P. A. Bayramov and R. A. Nuriev, Chaos synchronization Between Josephson junctions coupled with time delays, J. Supercon. Nov. Magn. **27**, PP. 2225-2229, (2014).

[101] T. V. Duzer and C. W. Turner, Principles of superconductive devices and circuits, second ed. Prentice Hall PTR, Upper Saddle River, NJ. USA, (1998).

[102] T. A. Fulton and L. N. Dunkleberger, Lifetime of the zero- voltage state in Josephson tunnel junctions, Phys. Rev. B, **9**, pp. 4760-4769, (1974).

[103] W. C. Stewart, Current voltage characteristics of Josephson junctions, Appl. Phys. Lett., **12**, pp. 277-280, (1968).

[104] D. E. Mc Cumber, tunneling and weak-link superconductor phenomena having potential device applications, J. Appl. Phys., **39**, pp. 2503-2508, (1968).

[105] C. B. Whan and C. J. Lobb, Complex dynamical behavior in RCL-Shunted Josephson tunnel junctions, Phys. Rev. E, **53**, pp. 405-413, (1996).

[106] A. B. Cawthorne, C. B. Whan and C. J. Lobb, Complex dynamics of resistively and inductively shunted Josephson junctions, J. Appl. Phys., **84**, pp. 1126-1132, (1998).

[107] Y. Mizugaki and K. Nakajima, Numerical investigation and model approximation for the hysteretic current-voltage characteristics of Josephson junctions with nonlinear quasiparticle resistance, Jpn. J. Appl. Phys., **36**, pp. 110-113, (1997).

[108] S. Sancho and A. Swarez, Frequency domain analysis of the periodically-forced Josephson-Junction circuit, IEEE trans. on circuits and systems, **61**, pp, 512-521, (2014).

[109] T. P. Valkering, C. L. A. Hooijer and M. F. Kroon, Dynamics of two capacitively coupled Josephson junctions in the overlamped limit, Physica D, **135**, PP. 137-153, (2000).

[110] M. Cirillo and N. F. Pederson, On bifurcation and transition to chaos in a Josephson junction, Phys. Lett., **90**, PP. 150-152, (1982).

[111] D. R. Gulevich and F. V. Kusmartsev, Flux cloning in Josephson transmission lines, Phys. Rev. Lett., **97**, PP. 017004-017008, (2006).

[112] N. F. Pedersen, Solitons in Josephson transmission lines modern Prob. Cond. Matter Sciences, **17**, pp. 469-501, (1986).

[113] T. Visser, Modelling and analysis of long Josephson Junctions, Twente University press, Netherlands, (2002).

[114] H. S. Newman and K. L. Davis, fluxon propagation in Josephson junction transmission lines coupled by resistive networks, J. Applied Phys., **53**, PP. 7026-7032, (1982).

[115] T. A. Fulton, R. C. Dynes, P. W. Anderson, A Josephson junction shift register employing single flux quanta, Proc. IEEE, 61, PP. 28-35 (1973).

[116] T. A. Fulton, R. C. Dynes, Single vortex propagation Josephson tunnel junctions, Solid State Commun., **12**, PP. 57-61, (1973).

[117] K. Nakajima, Y. Onodera and Y. Ogawa, Logic design of Josephson network, J. Applied Phys., **47**, PP. 1620-1627, (1976).

[118] N. F. Pedersen and A. V. Ustinov, Fluxons in Josephson transmission lines: new developments, supercond. Sci. Technol., **8**, PP. 389-401, (1995).

[119] A. C. Scott, Y. F. Flora and S. A. Reible, Magnetic flux propagation on a Josephson transmission line, J. Applied. Phys., **47**, PP. 3272-3286, (1976).

[120] K. K. Likharer and U. K. Semenov, RSFQ logic/memory family: A new Josephson junction technology for sub-Terahertz-clock-frequency digital systems, IEEE Trans. Appl. Supercond., **1**, PP. 3-28, (1991).

[121] A. V. Ustinov and M. Cirillo, Fluxon dynamics in one-dimensional Josephson-junction arrays, Phys. Rev. B, **47**, PP. 8357-8360, (1993).

[122] H. S. J. Van der Zant, D. Berman and T. P. Orlando, Fiske modes in one-dimensional parallel Josephson junction arrays, Phys. Rev. B, **49**, PP. 12945-12952, (1994).

[123] A. V. Ustinov, M. Cirillo, B. H. Larsen, V. A. Obozvov, P. Carelli and G. Rotoli, Experimental and numerical study of dynamic regimes in a discrete Sine-Gordon lattice, Phys. Rev. B, **51**, PP. 3081-3091, (1995).

[124] G. Fautso Kuiate and P. Woafo, I-V Characteristics of an array of discrete Josephson junction and effect of a localized defect, Physica C, 440, PP. 59-65, (2006).

[125] H. R. Mohebbi and A. H. Majedi, Analysis of series connected discrete Josephson transmission line, IEEE Trans. Microwave Theory Techn., **57**, PP. 1865-1873, (2009).

[126] H. S. J. Van der Zant, M. Barahona, A. E. Duvel, E. Trias, T. P. Orlando, S. Watanabe, S. Strogatz, Dynamics of one dimensional Josephson junction arrays, Physics D, **119**, PP. 219-226, (1998).

[127] A. V. Ustinov, B. A. Malomed, S. Sakai, Bunched fluxon states in one-dimensional Josephson junction arrays, Phys. Rev. B, **57**, PP. 11691-11691, (1998).

[128] K. Nakajima, Y. Onodera, Logic design of Josephson network. II, J. Appl. Phys., **49**, PP. 2958-2963, (1978).

[129] R. Lent, A. C. Azevedo, C. H. Andrade Moraes and V. O. Ana pinto, How many neurons do you have? some dogmas of quantitative neuroscience under revision, European J. neuroscience., **35**, pp. 1-9, (2012).

[130] D. Johnston and S. M. Wu, Foundations of cellular neurophysiology, the MIT press, (1994).

[131] S. K. Fisher and B. B. Boycott, Synaptic connexions made by horizontal cells within the outer plexiform layer of the retina of the cat and the rabbit, Proc. R. Soc. Lond. B, **186**, pp. 317-331, (1974).

[132] R. F. Schmidt, Fundamentals of neurophysiology, Springer- Verlag, Heidelberg Berlin New York, (1977).

[133] M. W. Barnett and P. M. Larkman, the action potential, Pract. Neurol., **7**, pp. 192-197, (2007).

[134] G. F. Striedter, Neurobiology: a functional approach, Oxford University press, (2016).

[135] R. Fitzhugh, Impluses and physiological state in theoretical models of nerve membrane, J. Biophys., **1**, pp. 445-466, (1961).

[136] J. Nagumo, S. Arimoto and S. Yoshizawa, An active pulse transmission line simulating nerve axon, proceedings of the IRE., **50**, pp. 2061-2070, (1962).

[137] E.M. Izhikevich, Neural excitability, spiking and bursting, Int. J. Bifurcation and Chaos., **10**, pp. 1171-1266, (2000).

[138] J. Rinzel and B. Ermentrout, Methods of Neural Modeling : From Synapses to Networks, chapter Analysis of neural excitability and oscillations, MIT Press., **50**, pp. 135-169, (1989).

[139] Z. He, C. Li, L. Chen and Z. Cao, Dynamic behaviors of the Fitzhugh-Nagumo neuron model with state-dependent impulsive effects, **121**, PP. 497-511, (2020).

[140] A. Hoff, J. V. dos santos, C. Manchein and H. A. Albuquerque, Numerical bifurcation analysis of two coupled Fitzhugh Nagumo oscillators, Eur. Phys. J. B, **87**, PP. 1-9, (2014).

[141] M. Aqil, K. S. Hong and M. Y. Jeong, Synchronization of coupled chaotic Fitzhugh-Nagumo systems, Commun Nonlinear Sci. Numer. Simulat., **17**, PP. 1615-1627, (2012).

[142] D. Hu, J. Yang and X. Liu, Delay-induced vibrational multiresonance in Fitzhugh-Nagumo system, Commun Nonlinear Sci. Numer. simulat., **17**, PP. 1031-1035, (2012).

[143] D. Valenti, G. Augello and B. Spagnolo, Dynamics of a Fitzhugh-Nagumo system subjected to autocorrelated noise, Eur. Phys. J. B, **65**, PP. 443-451, (2008).

[144] A. L. Hodgkin and A. Huxley, A quantitative description of membrane current and its application to conduction and excitation in nerve, J. Physiol., **117**, pp. 500-544, (1952).

[145] S. Binczack and J. M. Bilbault, experimental propagation failure in a nonlinear electrical lattice, Inter. J. Bifurc. Chaos, **14**, PP. 1819-1830, (2004).

[146] J. Engelbrecht, T. Peets, K. Tamn, M. Laasmaa and M. Vendelin, on the complexity of signal propagation in nerve fibres, proceedings of the estonian academy of sciences, **67**, PP. 28-38, (2018).

[147] I. Ratas and K. Pyragas, Effect of high-frequency stimulation on nerve pulse propagation in the Fitzhugh-Nagumo model, Nonlinear Dyn., **67**, PP. 2899-2908, (2012).

[148] A. Talidou, A. Burchard and I. M. Signal, Near pulse solutions of the Fitzhugh-Nagumo equations on cylindrical surfaces, J. Nonlinear Sci., **57**, PP. 1-39, (2021).

[149] L. A. Ranvier, Lecons sur l'histologie du système nerveux, par M. L. Ranvier, Recueillies par M. Ed. Weber. F. savy, Paris (1878).

[150] I. Ratas and K. Pyragas, Pulse propagation and failure in the discrete FitzHugh-Nagumo model subject to high-frequency stimulation, Phys. Rev. E **86**, PP. 046211-046220, (2012).

[151] T. Erneux and G. Nicolis, propagating waves in discrete bistable reaction-diffusion systems, Physica D, **67**, PP. 237-244, (1993).

[152] V. Booth and T. Erneux, mechanisms for propagation failure in discrete reaction-diffusion systems, Physica A, **188**, PP. 206-209, (1992).

[153] Z. J. Qian, H. Z. Huai and X. H. Wen, Neural signal Tuned by random long-range coonctions in coupled FitzHugh Nagumo neurons systems, Chin. Phys. Lett. **23**, PP. 2364-2367, (2006).

[154] A. A. Karim, T. Gaudin, A. Meyer, A. Buendia and S. Bouakaz, Procedural locomotion of multi-legged characters in dynamic environments, Université de Lyon, CNRS, (2012).

[155] M. Shibata, T. Hoshizaki and M. Ito, development of multi-legged locomotion for fast walking, IEEE, The International Power Electronics Conference, **15**, pp. 2204-2209, (2010).

[156] V. Y. Taffoti Yolong and P. Woafo, Dynamics of electrostatically actuated micro- electromechanical systems: single device and arrays of devices, Int. J. Bifur., Chaos **19**, pp. 1007-1022, (2009)

[157] G. Filatrella, V. Pierro, N.F. Pedersen and M.P. Sorensen, Negative Differential Resistance due to Nonlinearities in Single and Stacked Josephson Junctions, IEEE Trans. Appl. Supercond., **24**, pp. 1800407, (2014).

[158] A. H. Nayfeh and D.T. Mook, Nonlinear oscillation, Wiley-Interscience, New York, (1979)

[159] S. P. Timoshenko, Theorie de la stabilité élastique, Dunod, Paris, (1966).

[160] J. C. Chedjou, P. Woafo and S. Domngang, Shilnikov chaos and dynamics of a self-sustained electromechanical transducer, J. Vib. Acoust., **123**, pp. 170-174, (2001).

[161] C. A. Kitio Kwuimy and P.Woafo, Dynamics, chaos and synchronization of self-sustained electromechanical systems with clamped-free flexible arm, Nonlinear Dyn., **53**, pp. 201-214, (2008).

[162] R. Yamapi and M. A. Aziz-Alaoui, Vibration analysis and bifurcations in the self-sustained electromechanical system with multiple Functions, Commun. Nonlinear Sci. Numer. Simul., **12**, pp. 1534-1549, (2007).

[163] F. He, R. Ribas, C. Lahuec and M. Jézéquel, Discussion on the general oscillation startup condition and the Barkhausen criterion, Analog Integr. Circ. Sig. Process., **5**, pp. 1-7, (2008).

[164] J. D. Hoffman and S. Frankel, Numerical methods for engineers and scientists, New York: CRC Press, (2001).

[165] R. B. Bhat and S. Chakraverty, Numerical Analysis in engineering. London: Alpha Science International Ltd, (2007).

[166] S. E. Hebdoul and J. C. Garland, Radio-frequency spectral response of two-dimensional Josephson-junction arrays, Phys. Rev. B, **43**, pp. 13703-13706, (1991).

[167] S. E. Hebdoul and J. C. Garland, rf power dependence of subharmonic voltage spectra of two-dimensional Josephson-junction arrays, Phys. Rev. B, **47**, pp. 5190-5195, (1993).

[168] A. Scott, Nonlinear Science: emergence and dynamics of coherent structures. 2nd edition, Oxford University Press Inc, New York, (2003).

[169] P. Woafo, Kink dynamics in the highly discrete and coupled sine-Gordon system, Phys. Rev. B, **52**, pp. 6170-6173, (1995).

[170] Y.S. Kivshar and B.A. Malomed, Dynamics of solitons in nearly integrable systems, Rev. Mod. Phys., **61**, pp. 763-915, (1989).

[171] R. Fokoua Tiwang, P. Woafo and T.C. Kofane, Dynamics of fluxons in a system of two coupled Josephson transmission lines with local defects, J. Phys. Condens. Matter **6**, pp. 9745-9753, (1994).

[172] M. Tlidi, P. Mandel and R. Lefever, Localized structures and localized patterns in optical bistability. Physical review letters, **73**, pp. 640-644, (1994).

[173] J.J. Shen, H. W. Yin, and J. H. Dai, Dynamical behavior, transient chaos, and riddled basins of two charged particles in a Paul trap, Phys. Rev. A, **55**, pp. 2159-2164, (1997).

[174] T. Tal, The joy of transient chaos. Chaos, **25**, pp. 097619, (2015).

LIST OF PUBLICATIONS

1) **N. M. Kouami,** B. Nana and P. Woafo.: Analysis of nanoelectromechanical beams driven by an electrical line of Josephson junctions, Physica C: Superconductivity and its applications, **574**, PP. 1353658,(2020).

2) **N. M. Kouami**, B. Nana and P. Woafo.: Dynamics of array mechanical arms coupled each to a Fitzhug Nagumo neuron. Chaos soliton and fractals, **55**, PP. 111484, (2021).

Physica C: Superconductivity and its applications 574 (2020) 1353658

Contents lists available at ScienceDirect

Physica C: Superconductivity and its applications

journal homepage: www.elsevier.com/locate/physc

Analysis of array nanoelectromechanical beams driven by an electrical line of Josephson junctions

N.M. Kouami[a], B. Nana[b], P. Woafo[a,*]

[a] Laboratory of Modelling and Simulation in Engineering, Biomimetics and Prototypes, Faculty of Science, University of Yaounde I, PO Box 812 Yaounde, Cameroon
[b] Department of Physics, Higher Teacher Training College, University of Bamenda, PO Box 39 Bamenda, Cameroon

ARTICLE INFO

Keywords:
Nanoelectromechanical systems
Josephson transmission lines
Nano-actuation
Fluxons

ABSTRACT

An array of nanoelectromechanical beams driven by an electrical line of Josephson junctions equivalent models is studied. It is found that a single electromechanical system displays oscillations under a critical value of the DC bias current. In the case of an array of electromechanical system constituted of a series of coupled discrete Josephson junction with a beam place at each node, the numerical simulation shows that as the electric signal flows in the discrete array, each beam executes a pulse-like motion coming at each rest state as the electrical signal passes the node. When the bias current increases, the amplitude and period of the pulse-like shapes increase. One also notes the increase of the amplitude of the pulse-like shape when the magnetic field increases. The electromechanical system analyzed can be seen as a model for periodic nano-actuation processes or as a model of legs in a millipede system.

1. Introduction

Josephson junctions are theoretical and applied devices extensively studied in the field of nonlinear dynamics and materials sciences [1–8]. One particular interest in the Josephson Junction is its potential to generate high-frequency signals from the order of Gigahertz and Terahertz range [9,10]. Thus, it is considered as microwave radiation source and can be used for practical applications such as Superconducting Quantum Interference Devices (SQUIDs), detectors, digital logic circuits and voltage standards [11–14]. In order to appreciate the power outputs, contrary to a single Josephson junction which is not able to provide high power, many research activities have considered arrays of Josephson junctions [10,15–20].

Because of its large range of frequency variation and the high values of the frequencies, one can think of commanding some actuation processes at the nano level using a Josephson junction. This will lead to high frequency nanoelectromechanical systems. In the same line, as the nano-actuation is concerned, scientists and engineers are interested in the design of a large ensemble of nano-actuators. This can be obtained by coupling several nanoelectromechanical systems through their mechanical parts or through the electrical parts with different types of coupling. In this case, one can be interested by the synchronization criteria [21].

Another way is to consider an electrical line in which electrical signal propagates steadily with constant shape. This requires some special electrical lines such as nonlinear electrical transmission lines which are able to propagate special electrical signals such as solitons [22–26]. In these electrical transmission lines, the signal can be inserted periodically at one entrance node. Each signal introduced in the line will propagate along the line. An example of such electrical transmission lines, representing a discrete model of myelinated nerve fibers has been used recently to power an array of electromechanical systems [27].

It is known that long Josephson junctions and arrays of discrete Josephson point junctions exhibit soliton -like excitations, one of which is of the topological nature [28,29]. Thus, following the idea of Ref. [27], we consider in this work the behavior of an array of nano-beams, each of which is placed at a node of the discrete array. As it is indicated in Ref. [27], such an electromechanical system can be as models for nano-actuation, but also model for the legs of artificial millipedes. Indeed, millipedes move their legs in a wave like undulation along their body propelling themselves forward (or backward) against the substrate [30,31]. The study conducted here will also complement those considered in Ref. [32] where the authors studied the dynamics of nano-beam coupled to two Josephson junctions.

Thus, the aim of this work is to study the dynamical behavior of

* Corresponding author: P. Woafo, Laboratory of Modelling and Simulation in Engineering, Biomimetics and Prototypes, Faculty of Science, University of Yaounde I, PO Box 812 Yaounde, Cameroon. url:
E-mail address: pwoafo1@yahoo.fr (P. Woafo).
URL: http://www.lamsebp.org (P. Woafo).

https://doi.org/10.1016/j.physc.2020.1353658
Received 21 October 2019; Received in revised form 7 April 2020; Accepted 20 April 2020
Available online 11 May 2020
0921-4534/ © 2020 Elsevier B.V. All rights reserved.

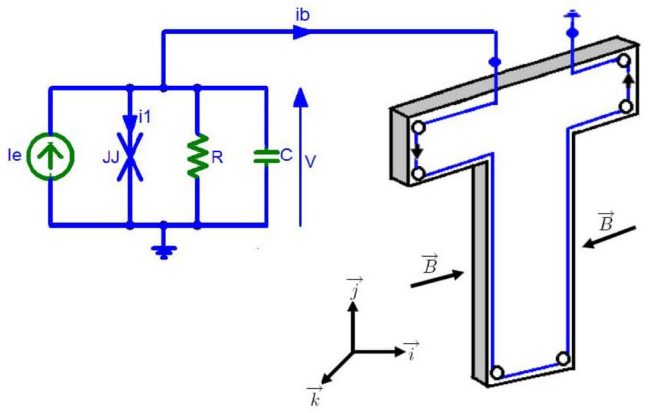

Figure 1. A single Josephson junction coupled to a nanoelectromechanical beam and its corresponding symbol

nano-beams motion in an array constituted of coupled discrete Josephson junctions. But, before considering the array, the dynamics of a single nanoelectromechanical beam powered by the electric equivalent of Josephson junction through a magnetic field will be considered. In section 2, we describe the system constituted of one single Josephson junction coupled magnetically to a nano- beam. The mathematical model and the dynamical behavior of such unit cell are presented. Section 3 deals with the array of nano-beams driven by an array of Josephson Junctions. We analyze numerically the effect of some parameters on the displacement process. Finally, a summary is given in the last section.

2. Nanoelectromechanical beam driven by a single Josephson junction

2.1. Description of the system

The schematic circuit of the Josephson junction model coupled magnetically to a nano-beam is shown in Figure 1.

It is made of an electrical part which is constituted by a Josephson junction circuit model whose components are respectively: *JJ* denotes the Josephson junction element, *C* the junction capacitance and *R* the junction resistance. I_e is an external current source necessary to bias the junction. The mechanical part is made of a nano-beam (parallel to $\vec{k}$) on which is placed a winding and the whole is in magnetic field $\vec{B}$ (parallel to $\vec{i}$).

2.2. Equations of a single system

Let *V* be the voltage across the Josephson junction and i_1 the current through the junction. The relations between *V*, the phase difference φ across the Josephson barrier and i_1 are given as [33]:

$$V = \frac{\hbar}{2e}\frac{d\phi}{d\tau} \tag{1}$$

$$i_1 = I_c \sin(\phi) \tag{2}$$

where *e* is the electron charge, ħ denotes the reduced Plank's constant and I_c is the critical current of the junction. The application of the Kirchhoff laws leads to the following differential equations:

$$C\frac{dV}{d\tau} + \frac{V}{R} + i_1 + i_b = I_e \tag{3}$$

$$L\frac{di_b}{d\tau} + ri_b = V + e_f \tag{4}$$

In equation (4), i_b is the current flowing through the winding located on the surface of the nano-beam. *L* and *r* are respectively the inductance and resistance of the winding and e_f is the induced electromotive voltage provided by the winding moving in the magnetic field, τ is the time. To obtain the equation of the nano-beam, let *U* be the deflection of nano-beam and ℓ the length of the wire loop located on the surface of the nano-beam. If we assume the nano-beam to be isotropic, uniform and flexible, then equation (5) describes the transversal vibration of the Euler-Bernoulli beam [34,35]:

$$\rho S\frac{\partial^2 U}{\partial \tau^2} + \lambda\frac{\partial U}{\partial \tau} + EI\frac{\partial^4 U}{\partial Z^4} = F_L\,, \tag{5}$$

where *S* is the cross-sectional area of the beam, ρ, λ, *E*, *I* and F_L are respectively the density, damping coefficient, Young's modulus, the second moment of area and the Laplace force. We have considered a thin beam and we neglect the axial and torsional vibrations compared to the flexible vibrations. The induced electromotive voltage and the Laplace force acting on the whole nano-beam due to the magnetic coupling are given as:

$$e_f = -B\ell\frac{\partial U}{\partial \tau}, \tag{6}$$

$$F_L = B\ell i_b. \tag{7}$$

Introducing equations (1), (2) and (6) into equations (3) and (4), and equation (7) into equation (5), it comes that the system is described by the following three coupled differential equations:

$$\frac{C\hbar}{2e}\frac{d^2\phi}{d\tau^2} + \frac{\hbar}{2eR}\frac{d\phi}{d\tau} + I_c sin\phi + i_b = I_e, \tag{8}$$

$$L\frac{di_b}{d\tau} + ri_b - \frac{\hbar}{2e}\frac{d\phi}{d\tau} + B\ell\frac{dU}{d\tau} = 0, \tag{9}$$

$$\rho S\frac{\partial^2 U}{\partial \tau^2} + \lambda\frac{\partial U}{\partial \tau} + EI\frac{\partial^4 U}{\partial Z^4} - B\ell i_b = 0. \tag{10}$$

For the cantilever beam, the following boundary conditions are added to the equation (10):

i) the fixed end ($Z = 0$) must have zero displacement and zero slope because of the clamp:

$$U(0,\tau) = 0 \text{ and } \frac{\partial U(0,\tau)}{\partial Z} = 0, \tag{11}$$

ii) ii) the free end ($Z = L_1$) cannot have a shearing force nor a bending moment:

$$\frac{\partial^2 U(L_1,\tau)}{\partial Z^2} = 0 \text{ and } \frac{\partial^3 U(L_1,\tau)}{\partial Z^3} = 0. \tag{12}$$

L_1represents the length of the nano-beam. One now introduces a set of dimensionless variables *u*, *x* and *z*. We normalize the variables as $u = \frac{U}{L_1}$, $x = \frac{i_b}{i_c}$ and $z = \frac{Z}{L_1}$. The time τ is normalized as $t = \omega_c\tau$, where ω_c is the characteristic radian frequency of the junction. The set of equations (8) to (10) can then be rewritten in the following dimensionless form:

$$\beta_c\frac{d^2\varphi}{dt^2} + \frac{d\varphi}{dt} + sin\varphi + x = i_e, \tag{13}$$

$$\frac{dx}{dt} + \mu x - \eta\frac{d\varphi}{dt} + \varepsilon_1\frac{\partial u}{\partial t} = 0, \tag{14}$$

$$\frac{\partial^2 u}{\partial t^2} + \alpha\frac{\partial u}{\partial t} + \omega_1^2\frac{\partial^4 u}{\partial z^4} = \gamma_1 x. \tag{15}$$

With the new introduced parameters defined as

$$\omega_c = \frac{2eRI_c}{\hbar},\ \beta_c = \frac{2eI_cR^2C}{\hbar},\ i_e = \frac{I_e}{I_c},\ \mu = \frac{r}{L\omega_c},\ \eta = \frac{\hbar}{2eLI_c},$$
$$\varepsilon_1 = \frac{B\ell L_1}{LI_c},$$
$$\alpha = \frac{\lambda}{\rho S\omega_c},\ \omega_1 = \frac{1}{L_1^2\omega_c}\sqrt{\frac{EI}{\rho S}} \quad \text{and} \quad \gamma_1 = \frac{B\ell I_c}{\rho SL_1\omega_c^2}. \tag{16}$$

β_c represents the Stewart-McCumber parameter. The dimensionless boundary conditions become

$$u(0,\ t) = 0 \text{and} \frac{\partial u(0,\ t)}{\partial z} = 0, \tag{17}$$

$$\frac{\partial^2 u(1,\ t)}{\partial z^2} = 0 \text{and} \frac{\partial^2 u(1,\ t)}{\partial z^3} = 0 \tag{18}$$

Equation (15) is a partial differential equation. In order to obtain an equivalent ordinary differential equation, one uses the Galerkin's method to have the modal equations [34]. For that purpose, the deflection of the nano-beam can be written as:

$$u(z,\ t) = \sum_{p=1}^{\infty} \varphi_p(z) y_p(t) \tag{19}$$

where $y_p(t)$ is the function of time at p^{th} mode and $\phi_p(z)$ is the spatial function. Resolving equation (15) without damping force and Laplace force and also taking into account the boundary conditions, the spatial function $\phi_p(z)$ is given by:

$$\phi_p(z) = \frac{sin(K_p) + sinh(K_p)}{cos(K_p) + cosh(K_p)}[cosh(K_pz) - cos(K_pz)] + [sin(K_pz) - sinh(K_pz)]. \tag{20}$$

Substitute equation (20) into equation (19) which is then multiplied by $\phi_m(z)$ and integrate from 0 to 1 for the first mode of vibration, see below.

$$\int_0^1 \varphi_m\varphi_p dz = 1,\ \int_0^1 \varphi_m(z)dz = c_1,\ \int_0^1 \varphi_m(z)\frac{\partial^4\varphi_p}{\partial z^4}dz = c_2 \tag{21}$$

After some mathematical manipulations, one obtains $K_p = 1.8751$, where K_p is the solution of the equation $cosK_p coshK_p = -1$, $c_1 = 1.066$ and $c_2 = 22.939$. As consequence, the set of equations (13) to (15) is reduced to the following system of three ordinary differential equations where the third equation is the modal equation of the nano-beam with y the displacement of the nanoelectromechanical beam at the first mode.

$$\begin{cases} \beta_c\ddot{\phi} + \dot{\phi} + sin\phi + x = i_e, \\ \dot{x} + \mu x - \eta\dot{\phi} + \varepsilon\dot{y} = 0, \\ \ddot{y} + \alpha\dot{y} + \omega^2 y - \gamma x = 0, \end{cases} \tag{22}$$

where $\omega = \omega_1\sqrt{c_2}$, $\gamma = c_1\gamma_1$ and $\varepsilon = \frac{\varepsilon_1}{c_1}$. The set of equations (22) can be transformed to five first order differential equations convenient for numerical simulation as follows:

$$\begin{cases} \dot{\phi} = v \\ \dot{v} = -\frac{1}{\beta_c}(v + \sin\phi + x - i_e) \\ \dot{x} = \eta v - \mu x - \varepsilon z \\ \dot{y} = z \\ \dot{z} = \gamma x - \omega^2 y - \alpha z \end{cases} \tag{23}$$

The values of the physical parameters used in this work are given in Table 1.

From the values of parameters given in Table 1, the following dimensionless numerical parameters are abtained: $\beta_c = 11.39 \times 10^{-3}$, $\eta = 94.07 \times 10^{-2}$, $\mu = 37.36 \times 10^{-3}$, $\varepsilon = 9.38$, $\gamma = 14.65 \times 10^{-3}$, $w = 2028 \times 10^{-2}$, $\alpha = 0.183$

The current $I_e(i_e)$ is a control or variable parameter.

Table 1
: Values of the physical parameters.

Parameters	Symbols	Values
Junction capacitance	C	$3.0\mu F$
Junction resistance	R	$5\mu\Omega$
Critical current of the junction	I_c	50mA
Young's modulus of the nano-beam	E	$200Gpa$
Density of the nano-beam	ρ	$8050kg/m^3$
Area of the nano-beam	S	$0.224{\cdot}10^{-18}m^2$
Second moment of area	I	$14{\cdot}10^{-46}m^4$
Length of the nano-beam	L_1	3.5nm
Damping coefficient	λ	$2.5{\cdot}10^{-7}Ns/m$
Magnetic flux intensity	B	0.5T
Resistance of the winding	r	$0.2\mu\Omega$
Inductance of the winding	L	$7.0{\cdot}10^{-15}H$
Length of the wire in the magnetic field	ℓ	2μm
Coupling inductance (in the array in section 3)	L_c	$6.0{\cdot}10^{-15}H$

2.3. Dynamical behavior of the system

The form of the differential equations reveals that the system can have two equilibrium points$G_1(\arcsin i_e,\ 0,\ 0,\ 0,\ 0)andG_2(\pi - \arcsin i_e,\ 0,\ 0,\ 0,\ 0)$ if the condition $i_e \leq 1$ is satisfied. Otherwise, there is no equilibrium point. The Jacobian matrix of the system (23) at $G = (\Phi_0,\ 0,\ 0,\ 0,\ 0)$where $\Phi_0 = \arcsin i_e$ or $\Phi_0 = \pi - \arcsin i_e$is expressed as

$$J = \begin{pmatrix} 0 & 1 & 0 & 0 & 0 \\ -\frac{\cos\Phi_0}{\beta_c} & -\frac{1}{\beta_c} & -\frac{1}{\beta c} & 0 & 0 \\ 0 & \eta & -\mu & 0 & -\varepsilon \\ 0 & 0 & 0 & 0 & 1 \\ 0 & 0 & \gamma & -\omega^2 & -\alpha \end{pmatrix} \tag{24}$$

The eigenvalues of the Jacobian matrix J are solutions of the following fifth order algebraic equation in s:

$$s^5 + a_4s^4 + a_3s^3 + a_2s^2 + a_1s + a_0 = 0, \tag{25}$$

where

$$a_4 = \alpha + \mu + \frac{1}{\beta_c},\ a_3 = \alpha\mu + \gamma\varepsilon + \omega^2 + \frac{\cos\Phi_0 + \alpha + \mu + \eta}{\beta_c}$$
$$a_2 = \mu\omega^2 + \frac{\alpha\mu + \varepsilon\gamma + \alpha\eta + \omega^2 + (\alpha + \mu)\cos\Phi_0}{\beta_c},$$
$$a_1 = \frac{(\mu + \eta + \cos\Phi_0)\omega^2 + (\alpha\mu + \varepsilon\gamma)\cos\Phi_0}{\beta_c},\ a_0 = \frac{\mu\omega^2\cos\Phi_0}{\beta_c} \tag{26}$$

The determinants of all Hurwitz matrices using the coefficients a_i of the characteristic equation (25) are given as:

$$d_1 = a_4,\ d_2 = a_4a_3 - a_2,\ d_3 = -a_4^2a_1 + a_4a_3a_2 + a_4a_0 - a_2^2$$
$$d_4 = -a_4^2a_1^2 - a_4a_3^2a_0 + a_4a_3a_2a_1 + 2a_4a_1a_0 + a_3a_2a_0 - a_2^2a_1 - a_0^2$$
$$d_5 = -a_4^2a_1^2a_0 - a_4a_3^2a_0^2 + a_4a_3a_2a_1a_0 + 2a_4a_1a_0^2 + a_3a_2a_0^2 - a_2^2a_1a_0 - a_0^3 \tag{27}$$

According to the Routh-Hurwitz criteria, the system is stable if and only if the coefficients a_i andd_i are all positive. That is, the eigenvalues of the characteristic polynomial have strictly negative real part [36]. After analysis, we found that the equilibrium point G_1 is unconditionally stable while the point G_2 is unstable. For $i_e$greater than 1, the Josephson junction circuit coupled to the electromechanical block provides asymmetric oscillations shown in Figure 2.

From the given values in Table 1; one can find that the natural frequency f_b of the nano-beam and the natural frequency f_j of the Josephson junction can be approximated as follows:

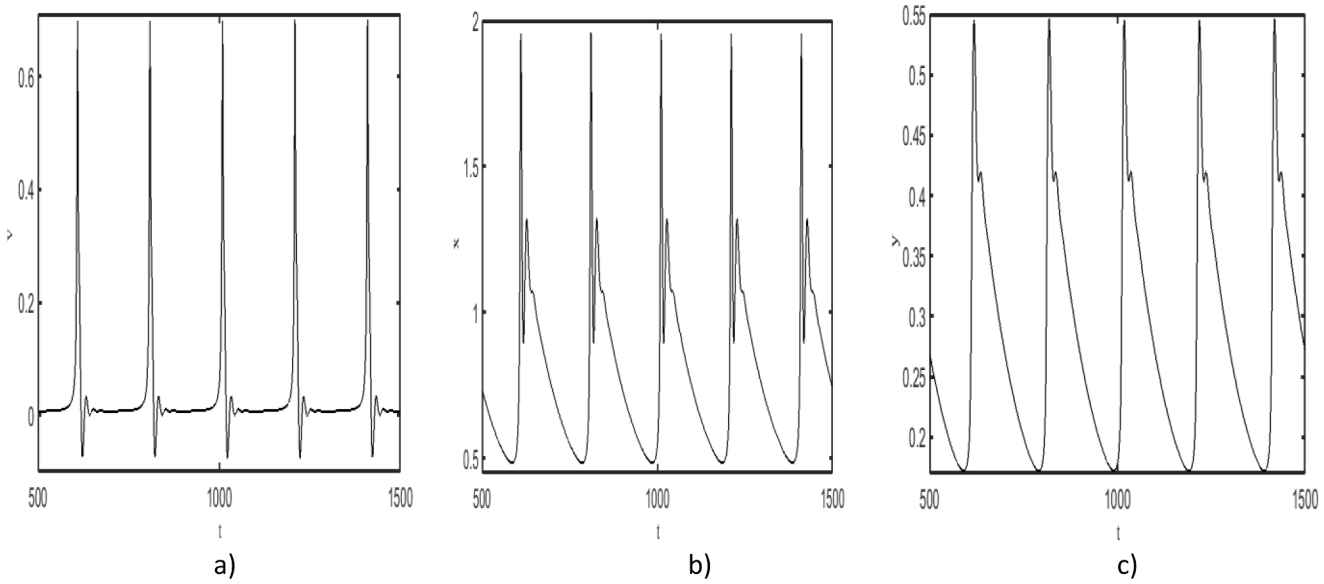

Figure 2. Different waveforms of the system for $i_e = 1.5$ a) Junction voltage v, b) current through the winding x and c) displacement of the nanoelectromechanical beam y.

$$\begin{aligned} f_b &= \frac{1}{2\pi}\left(\frac{1.8751}{L_1}\right)^2\sqrt{\frac{EI}{\rho S}} = 18.0MHz \\ f_b &= \frac{2eRI_c}{2\pi\hbar}\bar{\nu} = 135.23MHz \end{aligned} \tag{28}$$

These given values are of the order of MHz. The characteristic frequency of the Josepshon junction circuit used here is compatible with those of Nb-Au-Nb Josephson junctions [37,38]. Although they are not very close to induce resonant oscillations, it is observed that the oscillations amplitudes have values of the order of nanometer. The coupling between the two subsystems leads to oscillations with the frequency $f = 3.8\,MHz$ (see the curves of Figure 2).

At this level, it is interesting to analyse the effect of the input current on the amplitude of the oscillations. Figure 3 shows that the amplitude of the mechanical vibration is an increasing function of i_e. One can notice from the graph that for i_e<1, the amplitude is equal to 0 (no oscillation) while it increases with i_e for i_e greater than 1. It is interesting to note that at just after i_e=1, the amplitude jumps to a finite value and then increases steadily with i_e.

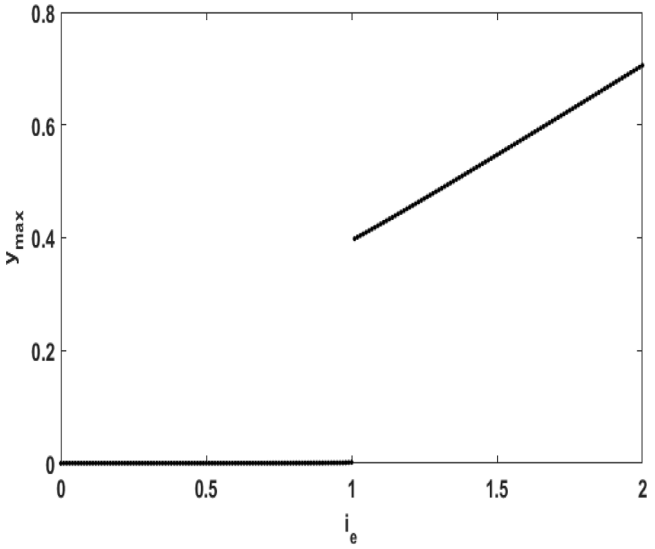

Figure 3. Amplitude curve of nano electromechanical beam as function of bias current i_e

3. Array of nanoelectromechanical beams driven by a discrete array of Josephson Junctions

3.1. Description of the system and equations

As indicated in the introduction, the other goal of this manuscript is to analyze the behavior of a system consisting of nano-beams fixed at each node of a discrete line of coupled Josephson junctions. The coupling between two neighborhood elements is made by an inductance L_c as illustrated in Figure 4.

Let ϕ_n, V_n, i_{bn} and U_n be respectively the phase, the junction voltage, the current through the winding and the deflection of the n^{th} nano-beam.

Using the Kirchhoff's laws, the circuit equations for the line are given by:

$$\begin{cases} \frac{C\hbar}{2e}\frac{d^2\phi_n}{d\tau^2} + \frac{\hbar}{2eR}\frac{d\phi_n}{d\tau} + I_c\sin\phi_n + i_{bn} = I_e + \frac{\hbar}{2eL_c}(\phi_{n+1} - 2\phi_n + \phi_{n-1}), \\ L\frac{di_{bn}}{d\tau} = \frac{\hbar}{2e}\frac{d\phi_n}{d\tau} - ri_{bn} - Bl\frac{\partial U_n}{\partial\tau}, \\ \rho s\frac{\partial^2 U_n}{\partial\tau^2} + \lambda\frac{\partial U_n}{\partial\tau} + EI\frac{\partial^4 U_n}{\partial Z_n^4} = Bli_{bn}. \end{cases} \tag{29}$$

Using the dimensionless parameters and the Galerkin transformations presented in the above section, it is found that the line circuit is described by the following system of coupled ordinary differential equations:

$$\begin{cases} \beta_c\ddot{\phi}_n + \dot{\phi}_n + \sin\phi_n + x_n = i_e + k(\phi_{n+1} - 2\phi_n + \phi_{n-1}), \\ \dot{x}_n + \mu x_n - \eta\dot{\phi}_n + \varepsilon\dot{y}_n = 0, \\ \ddot{y}_n + \alpha\dot{y}_n + \omega^2 y_n - \gamma x_n = 0. \end{cases} \tag{30}$$

This is the set of differential equations describing the propagation of electrical signal and the motion of Nnano-beams. In this set of equations, the coupling parameter k between neighboring nodes is defined as $k = \sqrt{\frac{\hbar}{2eL_cI_c}}$. The other parameters are defined as in equation (16).

3.2. Propagation of the signal and motion of the nanoelectromechanical beams

One of the most interesting effects of the discrete Josephson

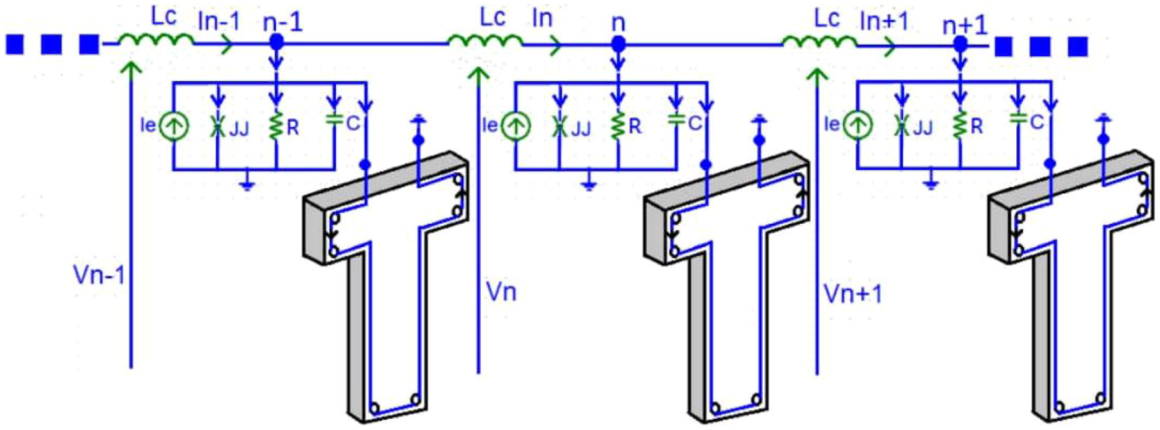

Figure 4. Schematic representation of the array of Josephson junctions coupled to nanoelectromechanical beams.

junctions line is its capacity to propagate topological solitons called fluxons (antifluxons) or kinks (antikinks). These topological solitons propagate steadily in the line without changing their shape. The mathematical form of the antikink (or antifluxon) is given by the following expression

$$\phi(n,\, t) = 4\arctan\exp\left(-\frac{n - \upsilon t - n_o}{\sqrt{1-\upsilon^2}}\right) \tag{31}$$

where υ is the velocity and n_0 is the initial node where the center of the antikink is located. With $n_0 = 100$ and $\upsilon = 0.5$, the antikink profile is plotted in Figure 5.

In this section, the set of discrete differential equations (30) is solved numerically using the fourth order Runge-Kutta algorithm with a time step $h_t = 5.\ 10^{-3}$[39]. For the initial conditions, we insert the mathematical form (31) in the discrete equation at site $n_0 = 100$. Periodic boundary conditions are used by setting $\phi(n=0) = \phi(n=N) + 2\pi n_a$ and $\phi_n(n=0) = \phi_n(n=N)$, $N$is the total number of cells and is equal to 300. Figure 6 displays the antikink propagation in the discrete line as well as the behavior of the nano-beams when the antikink propagates in the Josephson junction line.

Figures 6a), 6b) and 6c) show respectively the propagation of the antikink, the current x through the winding and the displacement $y$of the nanoelectromechanical beam as function of the number of cells.

As it appears in Figure 6, the antikink shape is preserved during the propagation and each nano-beam exhibits a pulse-like behavior moving from its rest state, then increases till a maximal value and then decreases to the rest state. This is interesting since it indicates the nano-beam executes an actuation work and then returns back to its rest state.

If the antikink is periodically inserted in the line, the nano-beam will periodically exhibits pulse-like behavior. The periodic insertion of antikinks in the transmission lines is ensured by the periodic boundary conditions which indicates that the kink periodically passes at one point after propagating all over the discrete line (see section 3.3). We have found that the amplitude and the frequency of the nano-beam displacement increase with the intensity of the magnetic field as it appears in Figures 7a), 7b) and 7c) plotted respectively for $\gamma = 0.008$, γ=0.0147 and γ=0.07.

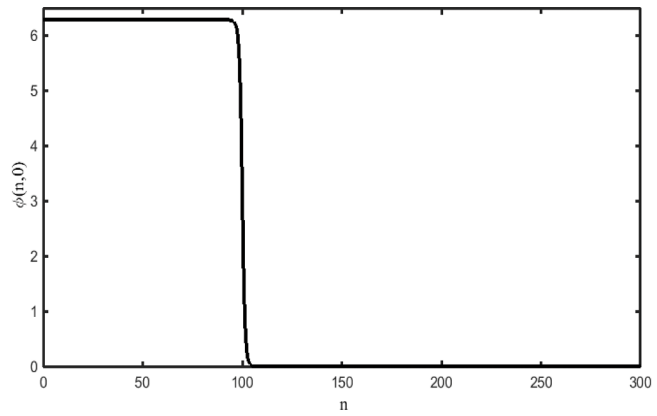

Figure 5. The antikink profile centered at $n_0 = 100$.

3.3. *Effect of the bias current on the nanoelectromechanical beams dynamics*

We have simulated the system for different values of i_e (0.7, 0.8, 1.0). It appears that a given nano-beam periodically exhibits pulse-like behavior as it can be seen in Figure 8 where one observes the displacement of the nano-beam at the cell number $n = 130$.

As i_e increases, the vibration period decreases moving from almost 3949.0 (for $i_e = 0.7$) to 1769.0 (for $i_e = 0.8$) and then 987.3 (for $i_e = 1.0$). The decrease of the period can be understood by the fact the antikink velocity increases proportionally with i_e [40,41]. Because of this increase of velocity and the boundary conditions, the antikink turns round the line as quickly as i_e increases. Consequently, each nano-beam is periodically excited and then delivers periodic pulse-like behavior.

As one observes in Figure 8, the amplitude of the nano-beam pulse-like behavior also increases with i_e. Our numerical simulations have also shown that the amplitude depends of the resistance r of the winding. This fact is more detailed in Figure 9 where the amplitude of the mechanical displacement is plotted versus i_e and for different values of r.

4. Conclusion

The aim of this work was first to analyze the dynamical behavior of a single nano-beam powered by a Josephson junction and second to analyze an array of nano-beams coupled to an array of discrete coupled Josephson junctions. It has been demonstrated that a nano-beam powered by a Josephson junction can deliver periodic vibration when a critical value of the DC bias current powering the junction is attained. The amplitude of the beam vibration increases with the DC bias current.

In the case of an array of discrete Josephson junctions having a nano-beam at each node, it has been seen that when the topological soliton (antikink) propagates in the discrete line, each beam exhibits a pulse-like behavior whose amplitude increases with the magnitude of the magnetic field. Because of the periodic boundary conditions and the fact that the antikink velocity is proportional to the DC bias current, one observes that each nano-beam periodically executes pulse-like displacement shape. The period of vibration of the beam decreases when the DC bias current increases while the amplitude of the pulse-like nano-beam displacement increases with the DC bias current. This constitutes an interesting dynamical electromechanical system which

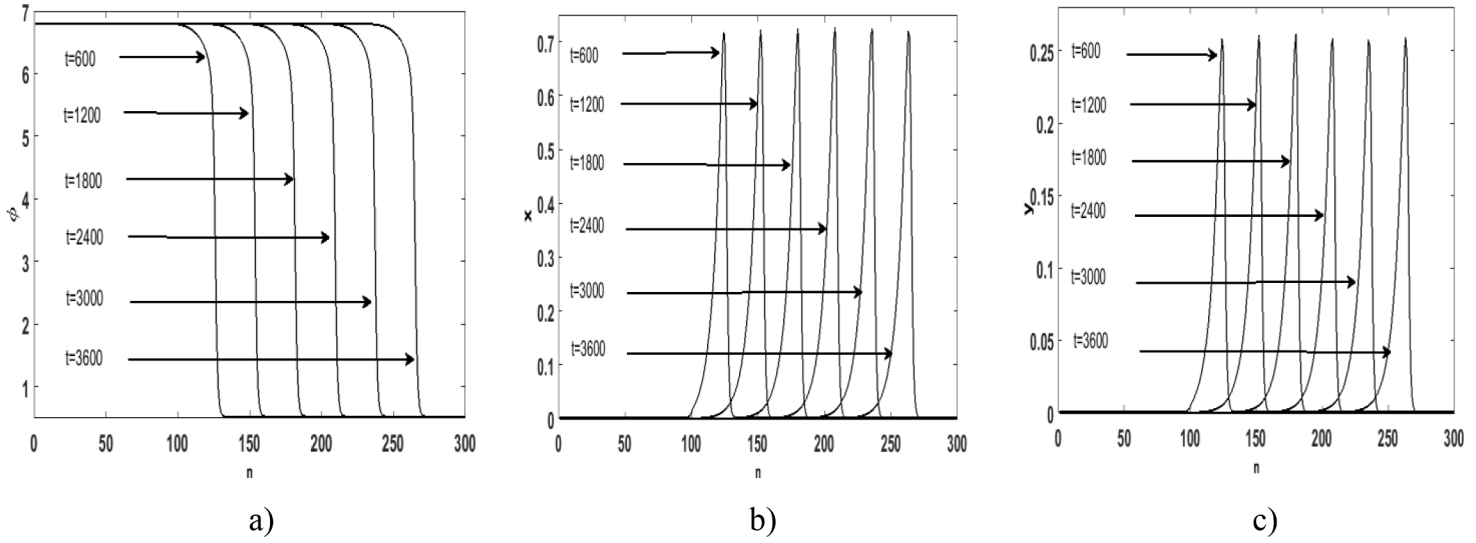

Figure 6. Different waveforms of the system as function of number of cells at different times for $i_e = 0.5$: a) phase ϕ, b) current x through the winding and c) displacement y of the nanoelectromechanical beam.

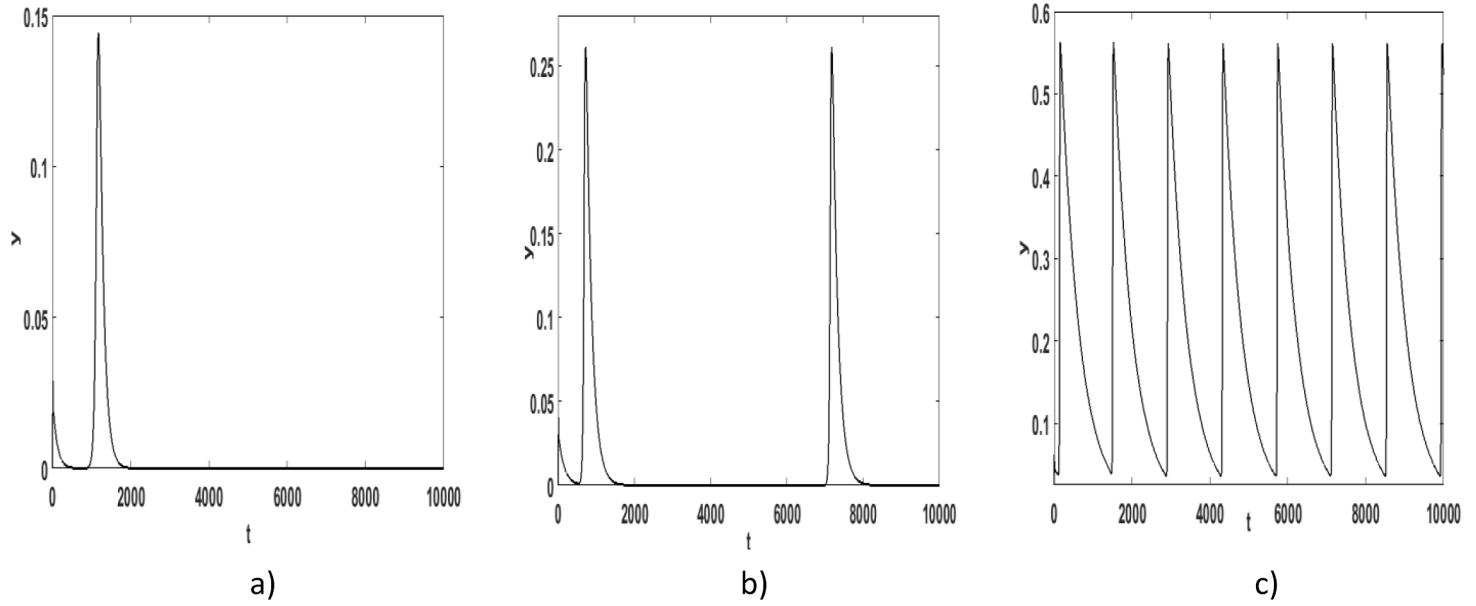

Figure 7. Effect of γ on the dynamics of nanoelectromechanical beam. We plot at $n = 130$ and we maintain the initial position $n_o = 100$. a) $\gamma = 0.008$, b) and c) γ=0.07

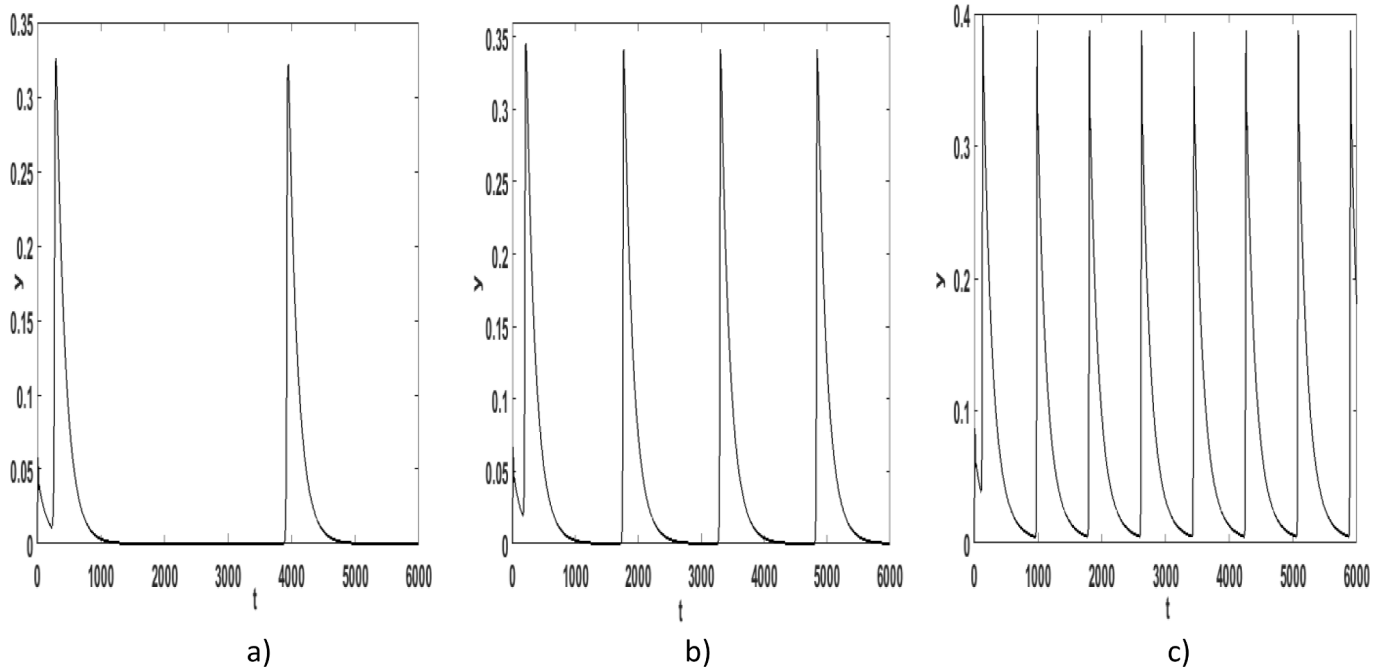

Figure 8. The time evolution of the nanoelectromechanical beam for different values of the bias current recorded at the cell $n = 130$. a) $i_e = 0.7$, b) $i_e = 0.8$ and c) $i_e = 1.0$.

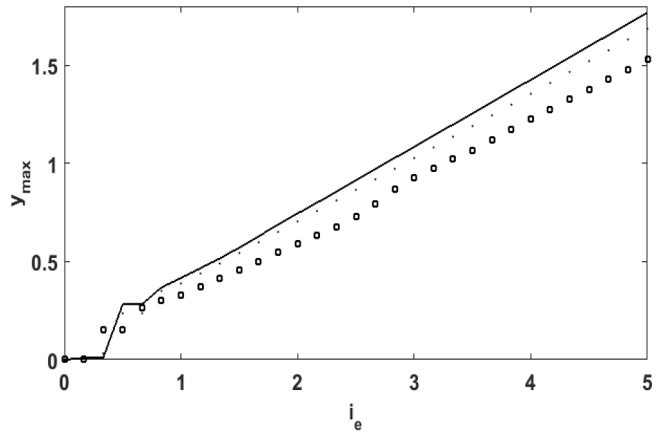

Figure 9. Variation of the $n = 120$nano-beam displacement amplitude as function of the bias current $i_e$for different values of r $r = 0.08\mu\Omega$ (full line), $r = 0.2\mu\Omega$ (dot line) and $r = 0.7\mu\Omega$ (square line).

can be used in nano-actuation processes.

However, the work was undertaken using a particular Josephson junction showing characteristic frequency of the range of MHz. But, it is known that most of the Josephson junctions present characteristic frequency of the order of GHz or THz. The coupling to mechanical structure whose natural frequency is of the order of MHz will not give rise to appreciable vibrations. Moreover, as it is known, superconducting materials exist at very low temperature. At this range of temperature, there might be a question on the mechanical properties of the mechanical beam. Consequently, a challenge will be to see how the device presented in Figure 1 behaves at very low temperature.

References

[1] S.K. Dana, D.C. Sengupta, K.D. Edoh, IEEE Trans. Circuits Syst 48 (2001) 990.
[2] M. Canturk, I.N. Askerzade, J. Supercond, Nov. Magn 26 (2013) 839.
[3] E.M. Shahverdiev, L.H. Hashimova, P.A. Bayramov, R.A. Nuriev, J. Supercon. Nov. Magn 27 (2014) 2225.
[4] A.B. Cawthorne, C.B. Whan, C.J. Lobb, J. Appl. Phys 84 (1998) 1126.
[5] T.P. Valkering, C.L.A. Hooijer, M.F. Kroon, Physica D<b> 135 (2000) 137.
[6] S. Sancho, A. Suarez, IEEE Trans. Circuits syst 61 (2014) 512.
[7] R.Fu Y.Lei, Lett. J. Exp 112 (2015) 60005–600p1.
[8] C.B. Whan, C.J. Lobb, M.G. Forrester, J. Appl. Phys 77 (1995) 382.
[9] M. Darula, T. Doderer, S. Beuven, Supercond. Sci. Technol (1999) R1.
[10] G. Filatrella, N.F. Perdersen, C.J. Lobb, P.Barbara, Eur. Phys. J. B34 (2003) 3.
[11] A. Uchida, H. Iida, N. Maki, M. Osawa, S. Yoshimori, IEEE Trans. Applied Supercond 14 (2004) 2065.
[12] R. Kleiner, P. Muller, Phys. Rev. B50 (1994) 3942.
[13] D. Dominguez, H.A. Cerdeira, Phys. Rev. Lett 71 (1993) 3359.
[14] K.K. Likharev, Dynamics of Josephson junctions and Circuits- Gordon and Breach Science Publishers, 1986.
[15] N. Vogt, R. Schafer, H. Rotzinger, W. Cui, A. Feibig, A. Shairman, A.V. Ustinov, Phys. Rev. B92 (2015) 045435-1.
[16] V.K. Kaplunenko, J. Mygind, N.F. Pedersen, A.V. Ustinov, J. Applied. Phys 73 (1993) 2019.
[17] B.H. Larsen, S.P. Benz, Appl. Lett 66 (1995) 3209.
[18] Y. Braiman, W.L. Ditto, K. Wiesenfeld, M.L. Spano, Phys. Lett. A206 (1995) 54.
[19] C.B. Whan, A.B. Cawthorne, C.J. Lobb, Phys. Rev. B53 (1996) 12340.
[20] S.Z. Lin, X. Hu, L. Bulaevsku, Phys. Rev. B84 (2011) 104501-1.
[21] S. Ngueuteu Mbouna, R. Yamapi, P. Woafo, J. Sound Vib.<b> 318 (2008) 1119.
[22] D.L. Sekulic, M.V. Sataric, M.B. Zivanov, J.S. Bajic, Electron. Electric. Engin 121 (2012) 1.
[23] M. Nguimdo, S. Noubissie, P. Woafo, J. Phys. Soc. Jpn 77 (2008) 124006.
[24] F. Kenmogne, D. Yemélé, Chaos Solitons Fract. 45 (2012) 21.
[25] F.B. Pelap, J.H. Kamga, S.B. Yamgoue, S.M. Ngounou, J.E. Ndecfo, Phys. Rev. E91 (2015) 022925.
[26] T. Kuusela, J. Hietarinta, K. Kokko, R. Laiho, Eur. J. Phys 8 (1987) 27.
[27] A. Mboussi Nkomidio, S. Noubissie, P. Woafo, Phys. Lett. A378 (2014) 857.
[28] G. Fautso Kuiate, P. Woafo, Phys. Scr 71 (2005) 556.
[29] G. Fautso Kuiate, P. Woafo, Physica C 440 (2006) 59.
[30] S.P. Hopkin, H.J. Read, The Biology of Millipedes, Oxford University Press, Oxford, 1992.
[31] J.G.E. Lewis, The Biology of Centipedes, Cambridge University Press, Cambridge, 1981.
[32] G.N. Koudafoke, G.H. Miwadinou, A.L. Hinvi, A.V. Monwanou, J.B. Chabi Orou, Physica Scripta<b> 59 (2019) 1.
[33] G. Filatrella, V. Pierro, N.F. Pedersen, M.P. Sorensen, IEEE Trans. Applied Supercond 24 (2014) 1800407.
[34] A.H. Nayfeh, D.T. Mook, Nonlinear Oscillation, Wiley-Interscience, New York, 1979.
[35] S.P. Timoshenko, Théorie de la stabilité élastique, Dunod, Paris, 1966.
[36] C. Hayashi, Nonlinear Oscillations in Physical Systems, Princeton University Press, 1986.
[37] S.E. Hebdoul, J.C. Garland, Phys. Rev. B 43 (1991) 13703.
[38] S.E. Hebdoul, J.C. Garland, Phys. Rev. B 47 (1993) 5190.
[39] P. Woafo, Phys. Rev. B52 (1995) 6170.
[40] Y.S. Kivshar, B.A. Malomed, Rev. Mod. Phys 61 (1989) 763.
[41] R. FokouaTiwang, P. Woafo, T.C. Kofane, J. Phys.:Condens. Matter 6 (1994) 9745.

Chaos, Solitons and Fractals 153 (2021) 111484

Contents lists available at ScienceDirect

Chaos, Solitons and Fractals

Nonlinear Science, and Nonequilibrium and Complex Phenomena

journal homepage: www.elsevier.com/locate/chaos

Frontiers

Dynamics of array mechanical arms coupled each to a Fitzhugh-Nagumo neuron

N.K. Mbeunga [a], B. Nana [b,*], P. Woafo [a]

[a] Laboratory of Modelling and Simulation in Engineering, Biomimetics and Prototypes, Faculty of Science, University of Yaounde I, Yaounde PO Box 812, Cameroon

[b] Department of Physics, Higher Teacher Training College, University of Bamenda, Bamenda PO Box 39, Cameroon

ARTICLE INFO

Article history:
Received 19 April 2021
Revised 13 September 2021
Accepted 19 September 2021

Keywords:
Fitzhugh-Nagumo neuron
Electromechanical
Antimonotonicity
Pulse-like motion

ABSTRACT

In this work, an array of electromechanical systems driven by an electrical line of Fitzhugh-Nagumo neurons is analyzed. It is shown that a single electromechanical system can display different dynamical behaviors such as single and multiple pulse generation, transient and permanent chaos, and antimonotonicity according to the system parameters. In the case of an array of the electromechanical system constituted of a series of coupled discrete Fitzhugh-Nagumo neurons, the numerical simulation shows that as the action potential flows in the discrete array, each electromechanical system executes a pulse-like motion coming at each resting state as the electrical signal passes the node. The electromechanical system analyzed can be seen as a model for multi-periodic actuation processes or a leg model in a millipede system. Furthermore, this line can also carry an envelope of action potential and can be useful for various kinds of information processing systems.

© 2021 Elsevier Ltd. All rights reserved.

1. Introduction

The study of wave propagation in systems of excitable biological cells is an important aspect of today's cardio-physiology and neurophysiology [1]. One typical example is propagation failure, leading to failure of these systems; this can be fatal in the case of the cardiac action potential. Biological neurons can produce a voltage in the forms of spikes due to their membranes which have voltage-dependent ionic channels [2]. It is shown that biological neurons can function either excitatory or inhibitory depending on the excitability threshold of the ion channels [3,4].

Inspired by the biological process, scientists have made efforts in neuroscience to understand through numerical simulations the electrical behavior of a real biological neuron. Among these models used, Hodgkin-Huxley [5,6], Hindmarsh Rose [7,8], Morris Lecar [9,10], and Fitzhugh Nagumo models [11,12], to name a few, exhibit an interesting dynamics investigation neurons. Being most used because of its simplicity and small equivalent circuit [13], Fitzhugh-Nagumo model is a relaxation oscillator [14]. It is also well known as a generalization of the Van der pol equations that are used to model the behavior of excitable systems [15]. The excitability represents the fact that from its resting state, if an excitable cell receives a stimulus (small perturbation) at a brief time interval, the membrane potential of the cell reaches a threshold value and generates an action potential before returning to its resting state [16–18]. Generally, in their dynamical behavior, Fitzhugh-Nagumo displays a solution that converges to a fixed point or a limit cycle [19,20].

The investigation of the behavior of the limit cycle has become an ongoing research topic [21–24]. For the actuation tasks, we will analyze a system where the Fitzhugh Nagumo neuron is used to control a mechanical arm. This is similar to the coupling between a biological neuron and a muscle. In fact, when the brain decides to put in motion a part of the body and gives the command to the motor neurons to execute this movement, it is the muscles at the end of the chain of command that ultimately contract to move the body part concerned. The axons of these motor neurons, emerging from the spinal cord, form a nerve that extends to the muscles to transmit this command. Where the tip of each axon comes into proximity with a muscle fibre, it forms a synapse with that fibre.

This device can be used to explain the mechanical movement of the arm or the leg for example. Similarly, the legs of millipedes or centipedes can be viewed as an array of Fitzhugh-Nagumo neurons coupled each to an electromechanical system. It can also be used for the legs of artificial millipedes where they move their legs in a wave-like motion from the front to the back. For this reason, the excitable Fitzhugh-Nagumo neuron has been widely studied as an electrical nonlinear transmission line for the propagation wave

* Corresponding author.
E-mail address: na1bo@yahoo.fr (B. Nana).

https://doi.org/10.1016/j.chaos.2021.111484
0960-0779/© 2021 Elsevier Ltd. All rights reserved.

phenomena [25–28] in which the nerve impulse during its propagation evolves from cell to cell by keeping its shape. It is mentioned that the electrical Fitzhugh-Nagumo line can be viewed as a discrete medium [29–31] or as a continuous medium [32–34]. In our work, we will consider the discrete medium.

Inspired by the topics of ref [35,36], the main objective of this work is to analyze the dynamical behavior of an array of electromechanical systems powered by an array of Fitzhugh-Nagumo neurons. The outline of the paper is organized as follows. Section 2 is devoted to the system constituted of one single Fitzhugh-Nagumo neuron coupled magnetically to a mechanical arm. The corresponding equations and their dynamical behavior are presented. Section 3 is concerned with the array of electromechanical arms powered by an array of discrete excitable Fitzhugh Nagumo neurons. We analyzed the effect of the coupling strength on the mechanical arms displacement. The paper ends with the conclusions presented in Section 4.

2. Electromechanical arm powered by a Fitzhugh-Nagumo neuron

2.1. Description and mathematical model

We consider an equivalent circuit of Fitzhugh-Nagumo neuron coupled magnetically to a mechanical arm, as shown in Fig. 1.

In the equivalent circuit of Fig. 1a), I_s represents the external electrical stimulation current source, C is the membrane capacitance, G is the membrane conductance, L and r represent respectively the inductance and resistance of the membrane. In this model, the conductance G is the only nonlinear element, and its voltage-current characteristics is given in Eq. (1):

$$i_G = \alpha v(v-\mu_1)(v-\mu_2), \tag{1}$$

where i_G and v are the current through and voltage across the conductance respectively. μ_1 and μ_2 are respectively the threshold voltage and the diffusion potential of the neuron. Finally, α is a fitting parameter and is a function of the potentials of different ions present in the neuron. The Fitzhugh-Nagumo model of nonlinear conductance shown in Eq. (1) can be simulated by a different nonlinear electric circuit, using a tunnel diode or a nonlinear resistor with a smooth cubic $v-i$ characteristic.

The block MS represents our mechanical arm and its internal structure is shown in Fig. 1b). The coil is positioned in the air gap of the magnet and a beam is rigidly attached to the coil. Besides, one spring is added to avoid the movement of the mobile beam away from the balanced position established when the system was assembled. The interaction of the current through the windings and the magnetic field produces mechanical vibrations of the mobile beam.

Two different strategies are responsible for electrical communication between neurons. One is the consequence of low resistance intercellular pathways, called “gap junctions”. The second occurs in the absence of cell-to-cell contacts and is a consequence of the extracellular electrical fields generated by the electrical activity of neurons. In the same manner, the capacitance C_m is used to realize the coupling between the neuron and the electromechanical system.

The application of the Kirchhoff laws to the circuit shown in Fig. 1a) leads to the following differential equations:

$$C\frac{dv}{dt} + i + i_m + \alpha v(v-\mu_1)(v-\mu_2) = I_s, \tag{2}$$

$$L\frac{di}{dt} + ri = v, \tag{3}$$

$$L_m\frac{di_m}{dt} + r_m i_m + u - v = -B\ell\frac{dx}{dt}, \tag{4}$$

$$C_m\frac{du}{dt} = i_m. \tag{5}$$

L_m and r_m are respectively the inductance and resistance of the windings, v represents the membrane potential of the cell, namely the voltage across the membrane capacitance C, i is the current through the inductance L, and represents biologically the recovery variable related to the inactivation of the sodium channels. i_m is the current flowing through the winding, u is the voltage across the capacitance C_m and represents the electrical synaptic potential or coupling potential, and t is the time.

Since there is no contact between the magnet and the moving windings, the friction effects are neglected here. The mechanical subsystem used in this work has been modeled mathematically by many authors [37–39] and the experimental verification of the theoretical results has been made using a motion detector and an accelerometer [40,41]. During their experimental works, Kitio et al. found excellent agreement between the experimental and theoretical results when the friction forces are not taken into account [40,41]. The equation of motion of the mobile beam of mass m is given by:

$$m\frac{d^2x}{dt^2} + \beta_0\frac{dx}{dt} + Kx = B\ell i_m, \tag{6}$$

where β_0 is the damping coefficient, and K is the spring constant. ℓ is the total length of the conductor used in the winding. The term $-B\ell\frac{dx}{dt}$ represents the induced voltage in the winding, while the

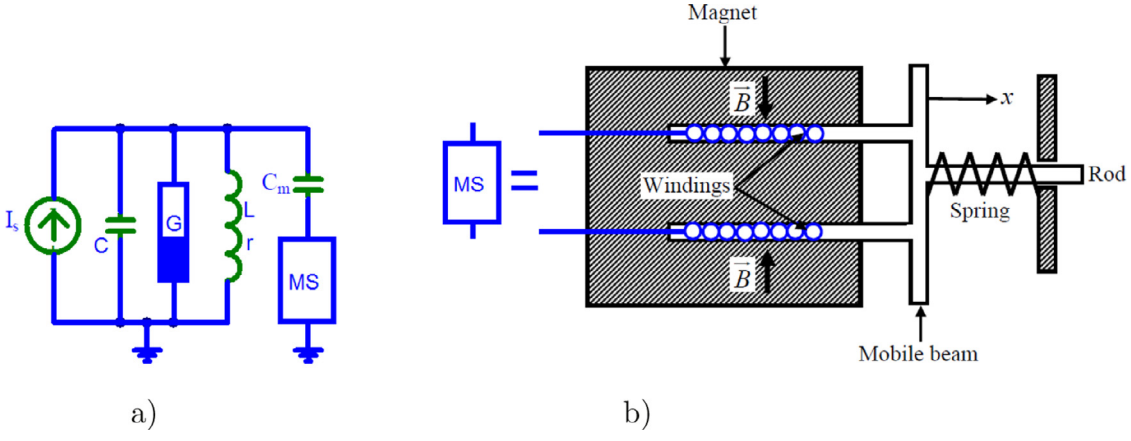

Fig. 1. a) Equivalent circuit of Fitzhugh-Nagumo neuron coupled to an electromechanical arm. b) Internal structure of the electromechanical subsystem.

term $B\ell i_m$ represents the Laplace force acting on the conducting wire in the magnetic field. Equation (6) is valid for displacements of small amplitudes in the mechanical subsystem. In case of high magnitude displacements, it is necessary to take into account the nonlinear response of the spring [37,38].

Introducing the news variables and the following dimensionless parameters:

$$i = w,\ i_m = z,\ \tau = \omega_0 t,\ a = \frac{1}{C\omega_0},\ b = \frac{1}{L\omega_0},\ d = \frac{1}{L_m\omega_0},\ \gamma = B\ell\omega_0,$$
$$\beta = \frac{\beta_0}{m\omega_0}, \varepsilon = \frac{K}{m\omega_0^2},\ \sigma = \frac{B\ell}{m\omega_0^2},\ \text{and}\ q = \frac{1}{C_m\omega_0}, \tag{7}$$

we obtain that the dimensionless equations governing the dynamics of the whole system are thus:

$$\begin{cases} \dot{v} = a(I_s - w - z - \alpha v(v-\mu_1)(v-\mu_2)), \\ \dot{w} = b(v - rw), \\ \ddot{x} = -\beta\dot{x} - \varepsilon x + \sigma z, \\ \dot{z} = d(v - u - r_m z - \gamma\dot{x}), \\ \dot{u} = qz. \end{cases} \tag{8}$$

The action of the electrical subsystem on the electromechanical part is visualized through the parameter σ while the effect of the electromechanical system in the electrical block is measured through the product $d\gamma$. If $\sigma \gg d\gamma$, the electrical subsystem is viewed as a voltage source by the mechanical part. In contrast, if $\sigma \ll d\gamma$, the power provided by the electrical part will be less than the power required by the mechanical part. The moderated values of σ and $d\gamma$ are then required for the subsystems to influence each other.

2.2. Stability analysis

Assume $E(v_0, w_0, z_0, u_0, y_0, x_0)$ is the equilibrium point of the system. From the system of Eqs. (8), we have $w_0 = \frac{v_0}{r}$, $z_0 = 0$, $u_0 = v_0$, $y_0 = 0$, and $x_0 = 0$ while v_0 is the solution of the following third-order algebraic equation:

$$v_0^3 - (\mu_1+\mu_2)v_0^2 + \left(\mu_1\mu_2 + \frac{1}{\alpha r}\right)v_0 - \frac{I_s}{\alpha} = 0. \tag{9}$$

To derive solutions of Eq. (9), let us consider the following parameters δ and ν and determinant Δ:

$$\delta = (\mu_1+\mu_2)^2 - 3\left(\mu_1\mu_2 + \frac{1}{\alpha r}\right),$$
$$\sigma = (\mu_1+\mu_2)\left(\frac{9}{2\alpha r} - \mu_1^2 - \mu_2^2 + \frac{5}{2}\mu_1\mu_2\right) - \frac{27I_s}{2\alpha}$$
$$\text{and}\ \Delta = \sigma^2 - \delta^3. \tag{10}$$

As odd degree polynomial, Eq. (9) can have one or three real solutions according to the values of the above parameters, and the sign of Δ.

If $\Delta \geq 0$, Eq. (9) has one real solution and the system has a single equilibrium point.

$$v_0 = \frac{1}{3}\left(\mu_1+\mu_2 - \sqrt[3]{\sqrt{\Delta}+\sigma} + \sqrt[3]{\sqrt{\Delta}-\sigma}\right). \tag{11}$$

If $\Delta < 0$, Eq. (9) has three real solutions, namely:

$$v_{0n} = \frac{1}{3}\left(\mu_1+\mu_2 + 2\sqrt{\delta}\cos\left(\frac{\theta+2n\pi}{3}\right)\right)$$
$$\text{with}\, n = -1,\ 0,\ 1\,\text{and}\,\theta = \arctan\left(\frac{\sqrt{-\Delta}}{\sigma}\right). \tag{12}$$

In this case, the system has three equilibrium points.

The values of the parameters used in this work are the following: $\beta_0 = 0.05$ Ns/m, $m = 20$ mg, $K = 10$ N/m, $B = 0.8$ T, $C = 60\,\mu$F, $L = 240$ mH, $\mu_1 = 0.14$ V, $\mu_2 = 1.0$ V, $r = 2.5\,\Omega$ and $C_m = 4700\,\mu$F.

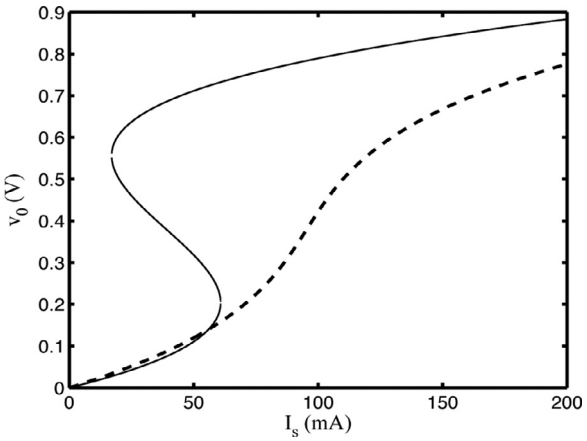

Fig. 2. Equilibrium potential v_0 as a function of the stimulation current I_s. The curve with dashed line is obtained for $\alpha = 1$, while the curve with full line is obtained for $\alpha = 2$.

I_s and ℓ are used as control parameters with $0 \leqslant I_s \leqslant 200$ mA and $0 \leqslant \ell \leqslant 10$ m. With the variation of ℓ, the winding resistance (in Ω) and the winding inductance (in mH) are given as: $r_m = 1.5\ell$ and $L_m = 1.25\ell^2$.

Using the parameters given above, the evolution of the equilibrium potential v_0 is plotted as a function of the stimulation current I_s in Fig. 2, and for two different values of the parameter α.

For the graph of Fig. 2, we have considered $\ell = 1$ m. The curve with a dashed line and the curve with a full line are obtained respectively for $\alpha = 1$ and $\alpha = 2$. As predicted analytically, the system can present one equilibrium potential or three equilibrium potentials depending on the values of the parameters. As noticed from the graph, for $\alpha = 2$, the case of three equilibrium points arrives here for values of the stimulation currents between 17.01 mA and 60.815 mA.

The unstable (or stable) branch connecting the two stable (or unstable) states of the hysteresis cycle extends from I_{s-} to I_{s+} given respectively as

$$I_{s\mp} = \alpha v_\mp\left(v_\mp^2 - (\mu_1+\mu_2)v_\mp + \mu_1\mu_2 + \tfrac{1}{\alpha r}\right)$$
$$\text{where}\, v_\mp = \tfrac{\mu_1+\mu_2}{3} \mp \sqrt{\left(\tfrac{\mu_1+\mu_2}{3}\right)^2 - \tfrac{\mu_1\mu_2}{3} - \tfrac{1}{3\alpha r}}. \tag{13}$$

From Eq. (13), we can conclude that the system will present three equilibrium points if the parameter α satisfies the following condition:

$$\alpha \geqslant \alpha_{\min} = \frac{3}{r\left(\mu_1^2+\mu_2^2-\mu_1\mu_2\right)}. \tag{14}$$

For $\alpha \leqslant \alpha_{\min}$ we have a mono system while for $\alpha \geqslant \alpha_{\min}$ the curve of Fig. 2 presents a bistable system. According to Tlidi et al., there must be a critical alpha of nascent bistability [42].

The stability of the system is determined by the eigenvalues of the Jacobian matrix at equilibrium points E given by :

$$J = \begin{bmatrix} -a\chi\alpha & -a & 0 & 0 & -a & 0 \\ b & -br & 0 & 0 & 0 & 0 \\ 0 & 0 & 0 & 1 & 0 & 0 \\ 0 & 0 & -\varepsilon & -\beta & \sigma & 0 \\ d & 0 & 0 & -d\gamma & -dr_m & -d \\ 0 & 0 & 0 & 0 & q & 0 \end{bmatrix}, \tag{15}$$

with $\chi = 3v_0^2 - 2(\mu_1+\mu_2)v_0 + \mu_1\mu_2$.

Its eigenvalues are solutions of the characteristic polynomial in λ of the linearization at E, namely:

$$\lambda^6 + a_5\lambda^5 + a_4\lambda^4 + a_3\lambda^3 + a_2\lambda^2 + a_1\lambda + a_0 = 0. \tag{16}$$

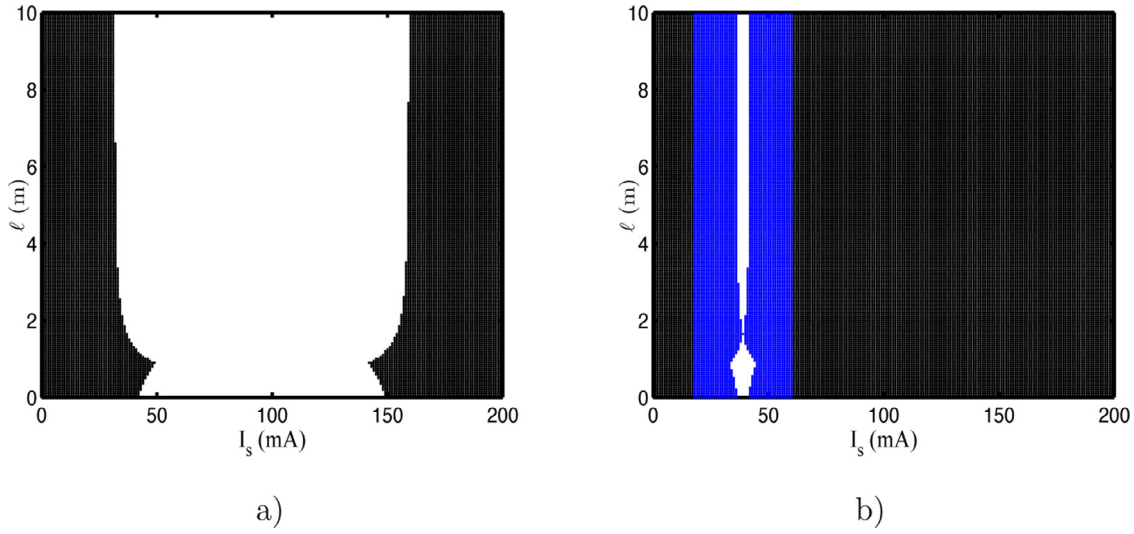

Fig. 3. Stability domain in the plane (I_s, ℓ). In the Black area, the system is stable around the single equilibrium point while in the white area, the system is unstable. In the blue area, the system has one stable equilibrium point amount three. a) $\alpha = 1$ and b) $\alpha = 2$. (For interpretation of the references to colour in this figure legend, the reader is referred to the web version of this article.)

Here the coefficients a_n, with $0 \leq n \leq 5$ are given respectively as:

$$
\begin{aligned}
a_5 &= a\alpha\chi + \beta + dr_m + br,\\
a_4 &= (a\alpha\chi + \beta)(br + dr_m) + brdr_m + d\gamma\sigma + \varepsilon + dq + a\alpha\chi\beta + a(b+d),\\
a_3 &= (\varepsilon + a\alpha\chi\beta)(br + dr_m) + a\beta(b+d) + abd(r + r_m)\\
&\quad + brdr_m(\beta + a\alpha\chi) + brd\gamma\sigma + a\alpha\chi(\varepsilon + d\gamma\sigma)\\
&\quad + dq(\beta + br + a\alpha\chi),\\
a_2 &= brdr_m(\varepsilon + a\alpha\chi\beta) + abd\beta(r + r_m) + abd\gamma\sigma + a\alpha\chi\varepsilon(br + dr_m)\\
&\quad + bra\alpha\chi d\gamma\sigma + a\varepsilon(b+d) + \varepsilon dq + bdrq(\beta + a\alpha\chi) + adq(b + \alpha\chi\beta),\\
a_1 &= abd\varepsilon(r + r_m + \alpha a\chi rr_m) + dqb(\varepsilon r + a\beta) + a\alpha\chi dq(\varepsilon + br\beta),\\
a_0 &= ab\varepsilon dq(1 + \alpha r\chi).
\end{aligned}
$$

We have used the Routh-Hurwitz criterion [36] to analyze the stability of the equilibrium points. Using the parameters given above, the stability boundary of the system is plotted in Fig. 3a) and Fig. 3b) for $\alpha = 1$ and $\alpha = 2$ respectively.

In Fig. 3a), we have two colored regions, while in Fig. 3b) we have three colored regions. If a coupled of values I_s and ℓ is chosen in the black regions, the system is stable around the single equilibrium point. However, if a coupled of values I_s and ℓ is chosen in the white regions, the system is unstable. In the blue region of Fig. 3b), the system has three equilibrium points, and one of these is stable.

2.3. Limit cycle prediction

Although precise knowledge of the waveform of a limit cycle is usually not mandatory, knowledge of the existence of a limit cycle, and its approximate amplitude and frequency, is a prerequisite to good system design. The limit cycle phenomenon deserves special attention since it is apt to occur in any nonlinear physical system. A limit cycle is desirable here since it provides a real situation where all the variables are not constant. We will apply the linear theory to the quasi-linearized system, and points of neutral stability are sought. Any undamped oscillations so arrived at are interpreted as limit cycles in the original nonlinear system.

If we consider the solution of Eq. (16) to be of the form of $\lambda = j\omega$, where $j^2 = -1$ and ω is the natural radian frequency of the system, then the following radian frequencies and the condition for self-starting are obtained:

$$\omega_1 = \sqrt{\frac{a_3 - \sqrt{a_3^2 - 4a_1a_5}}{2a_5}} \quad \text{and} \quad \omega_2 = \sqrt{\frac{a_3 + \sqrt{a_3^2 - 4a_1a_5}}{2a_5}}. \tag{17}$$

$$a_3^2 - 4a_1a_5 \geqslant 0 \text{ and } \left(a_1a_5 - a_3^2 - a_2a_5^2 + a_3a_4a_5\right)\omega_n^2 + \left(a_0a_5^2 + a_1a_3 - a_1a_4a_5\right) = 0,\ n = 1,\ 2. \tag{18}$$

During our investigations, we have found that for large values of the parameter ℓ, the system oscillates with the radian frequency ω_1 while it oscillates with the radian frequency ω_2 for small values of ℓ. With the stimulation current I_s varies from 0 mA up to 200 mA, we have found the corresponding values of ℓ that satisfy the set of Eqs. (18) and our result is presented in the graph of Fig. 4a). The corresponding value of the frequency obtained from Eq. (17) is plotted in Fig. 4b).

The curves of Fig. 4 are obtained for $\alpha = 1$ and the values of $\ell < 10$ m have been considered. We can notice from the graph that, as the stimulation current increases, the value of ℓ that satisfies the oscillation condition given by Eq. (18) can be found if 31.83 mA$\leq I_s \leq$ 159.1 mA.

2.4. Oscillation boundaries

Using the Routh-Hurwitz coefficients, we have determined the oscillation boundaries of the system and our results are presented in Fig. 3a). If the values of I_s and ℓ are chosen in the black areas of Fig. 3a), the system will converge towards the equilibrium point. Otherwise, the system will fall in the oscillation. For example, with $\ell = 1$ m we find that the system will oscillate for 33.7 mA$\leq I_s \leq$ 154.0 mA. To verify this result, we have consider the following three values of I_s: $I_s = 30$ mA, $I_s = 90$ mA and $I_s = 160$ mA. The corresponding time series of the membrane potential and the mechanical displacement are plotted respectively in Fig. 5 and Fig. 6.

As shown on the graphs of Fig. 5 and Fig. 6, when the stimulation current is less than 33.7 mA or greater than 154.0 mA, the system converges toward the single stable equilibrium point. While if the stimulation current is between 33.7 mA and 154.0 mA, the system provides oscillating signals. The frequency of the signal plotted

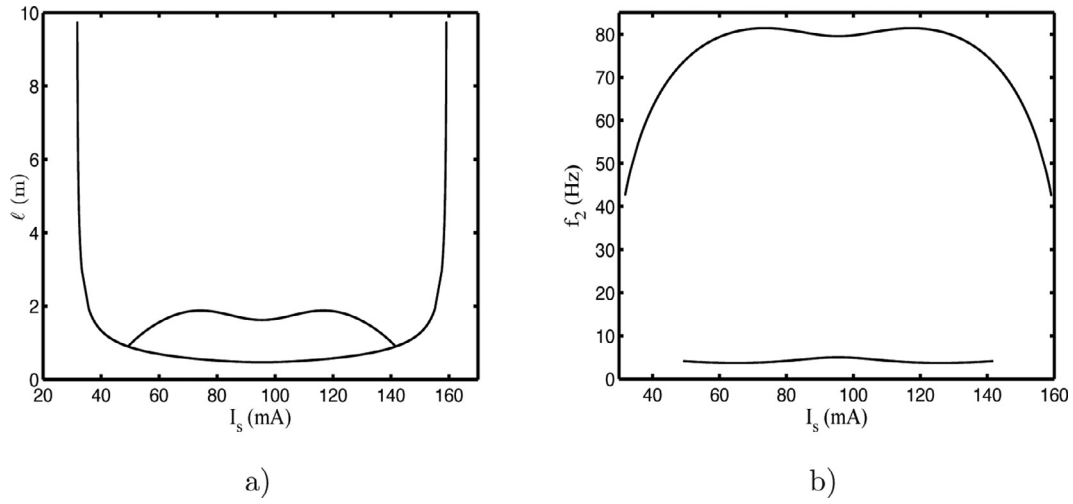

Fig. 4. a) The oscillation condition satisfied by the parameter ℓ as a function of I_s, b) the natural frequency of the system as a function of I_s.

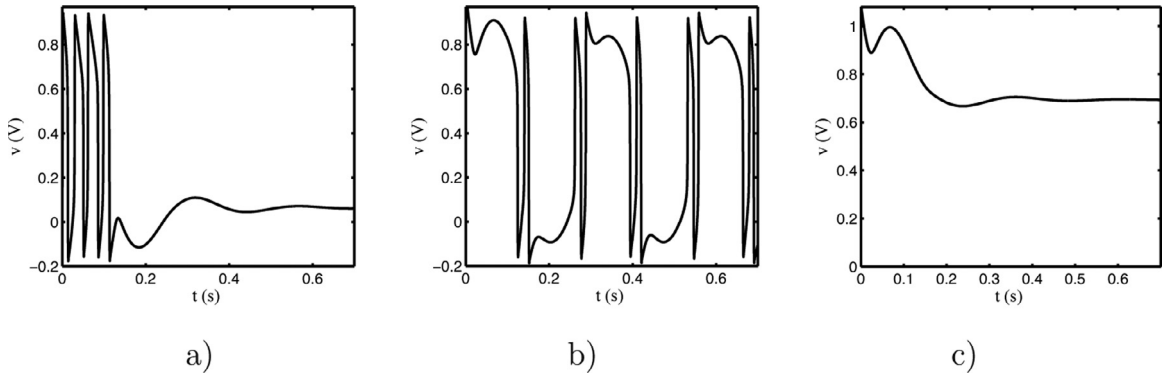

Fig. 5. Different time series of the membrane potential v for different values of I_s. a) $I_s = 30$ mA, b) $I_s = 90$ mA and c) $I_s = 160$ mA.

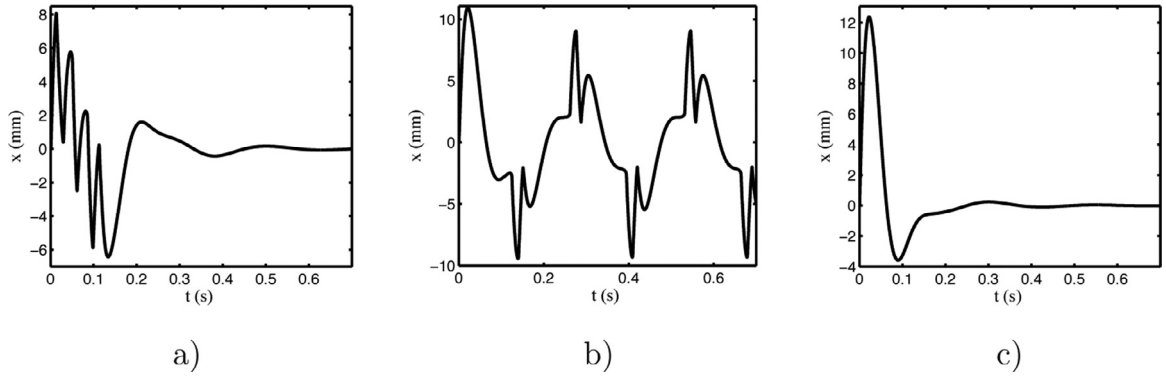

Fig. 6. Different time series of the mechanical displacement x for different values of I_s. a) $I_s = 30$ mA, b) $I_s = 90$ mA and c) $I_s = 160$ mA.

in the graph of Figs. 5b) and 6b) is 3.704 Hz. The obtained numerical results are in good agreement with our analytical predictions.

2.5. Effect of some parameters

It is interesting at this level to see how some parameters affect the dynamics of the system, specially the amplitude and frequency of the mechanical displacement. This element can be important to fix the parameters of the system. We will first analyze the effect of the length ℓ of the conductor used in the winding. Therefore, we plot the amplitudes of the membrane potential and the mechanical displacement as a function of ℓ and this for two different values of the spring constant as presented in Fig. 7.

For both Figs. 7a) and 7b), the full lines and the dashed lines are plotted respectively for $K = 10$ N/m and $K = 20$ N/m. As revealed by the graphs, when the system oscillates, the amplitude of the membrane potential is closed to unity while the amplitude of the mechanical displacement is a decreasing function of ℓ. Otherwise, the system converges to the equilibrium point. The mechanical displacement reaches its maximum value when $\ell \simeq 2$ m. As mentioned in the previous section and clearly confirmed by these graphs, the system presents large oscillation regions for small values of the spring constants. This is because electromechanical systems generally oscillate at low frequencies, which means small values of the spring constants. We can also notice from the graphs that the equilibrium points are not a function of the spring con-

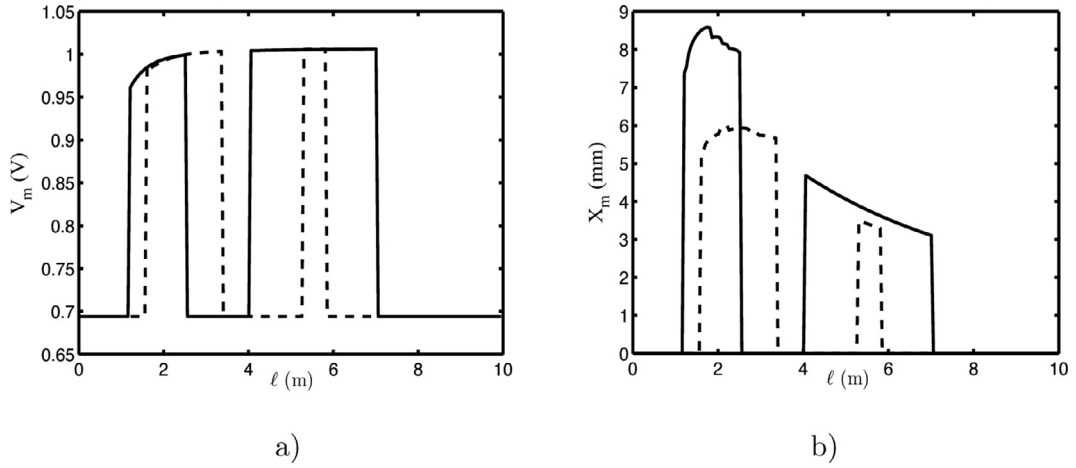

Fig. 7. a) Amplitude of the membrane potential V_m as function of ℓ, b) Amplitude of the mechanical displacement X_m as function of ℓ. Full line ($K = 10$ N/m) and dashed line ($K = 20$ N/m).

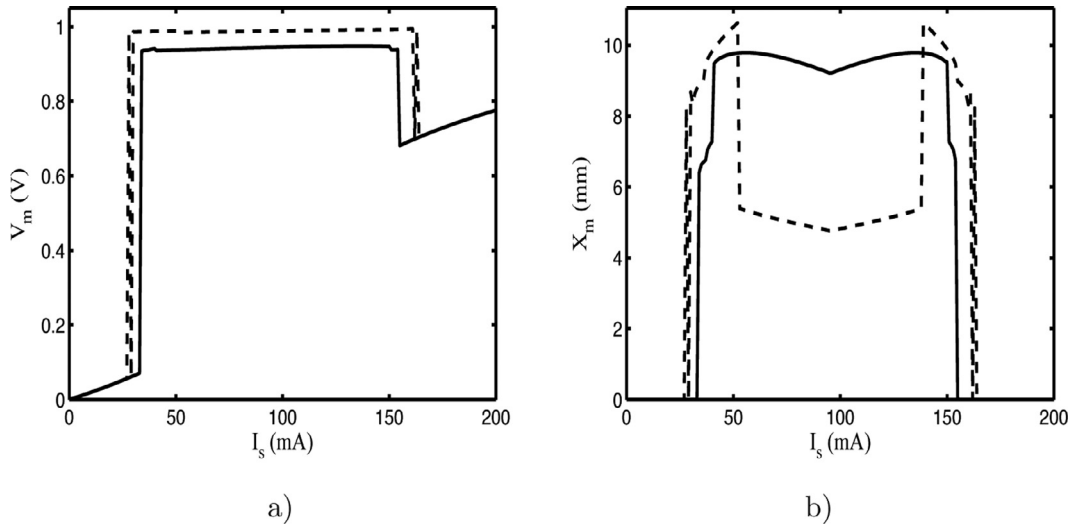

Fig. 8. a) Amplitude of the membrane potential V_m as a function of I_s, b) Amplitude of the mechanical displacement X_m as a function of I_s. Full line ($\ell = 1$ m) and dashed line ($\ell = 2$ m).

stant K and the length ℓ of the conductor used in the winding, and this has been observed during our analytical investigations presented previously. Finally, the graphs show that the amplitude of the mechanical displacement and the oscillation domain are decreasing functions of the spring constant.

Furthermore, we analyze the dynamical behavior of the system using the stimulation current I_s as the control parameter. The amplitude responses of electrical and mechanical subsystems are respectively shown in Fig. 8a) and Fig. 8b) for two values of ℓ.

For both Figs. 8a) and 8b), the curves with the full line are plotted for $\ell = 1$ m, while the curves with dashed lines are plotted for $\ell = 2$ m. Three regions can be identified in these figures. Firstly, for the stimulation current less than approximatively 30 mA (depending on the length of the conducting wire), the action potential is not produced, hence no oscillation of the mechanical system. Secondly, when 30 mA $\leq I_s \leq$ 162 mA, an action potential is generated and we have oscillation of the mechanical system. In the third region, the mechanical system is at equilibrium even if an action potential has been generated in the electrical system. We can notice from the graphs that when the system falls in the oscillation, the amplitude of the membrane potential and the amplitude of the mechanical displacement are not affected by the input current I_s. The figures also show that the amplitudes remain constant (no oscillation) as the stimulation current I_s increases until a critical value from where both amplitudes increase abruptly.

2.6. Chaotic behavior

The characteristic dynamical behaviors are finally investigated by varying the type of the input current source. We have done many simulations, but a part of transient chaos [43,44], permanent chaotic behavior has not been found in the autonomous system. Hence, the constant current source is replaced here by a sinusoidal current source of amplitude I_m and frequency f defined as

$$i_s = I_s + I_m \sin(\omega t) \text{ where } \omega = \frac{2\pi f}{\omega_0}, \tag{19}$$

where I_s represents the DC component and ω is the normalized radian frequency of the external source. We will study the dynamics of the system keeping constant the following parameters: $\ell = 4$ m, $L = 7.0$ mH and $f = 780.72$ Hz. For I_s equals successively 3 mA, -3.4 mA, -5 mA, -7 mA, -12 mA and -15 mA, the bifurcation diagrams v versus I_m are shown in Fig. 9.

In the bifurcation diagrams of Figs. 9a), 9b), 9c) and 9d), chaotic states are observed. The system follows a period-doubling route

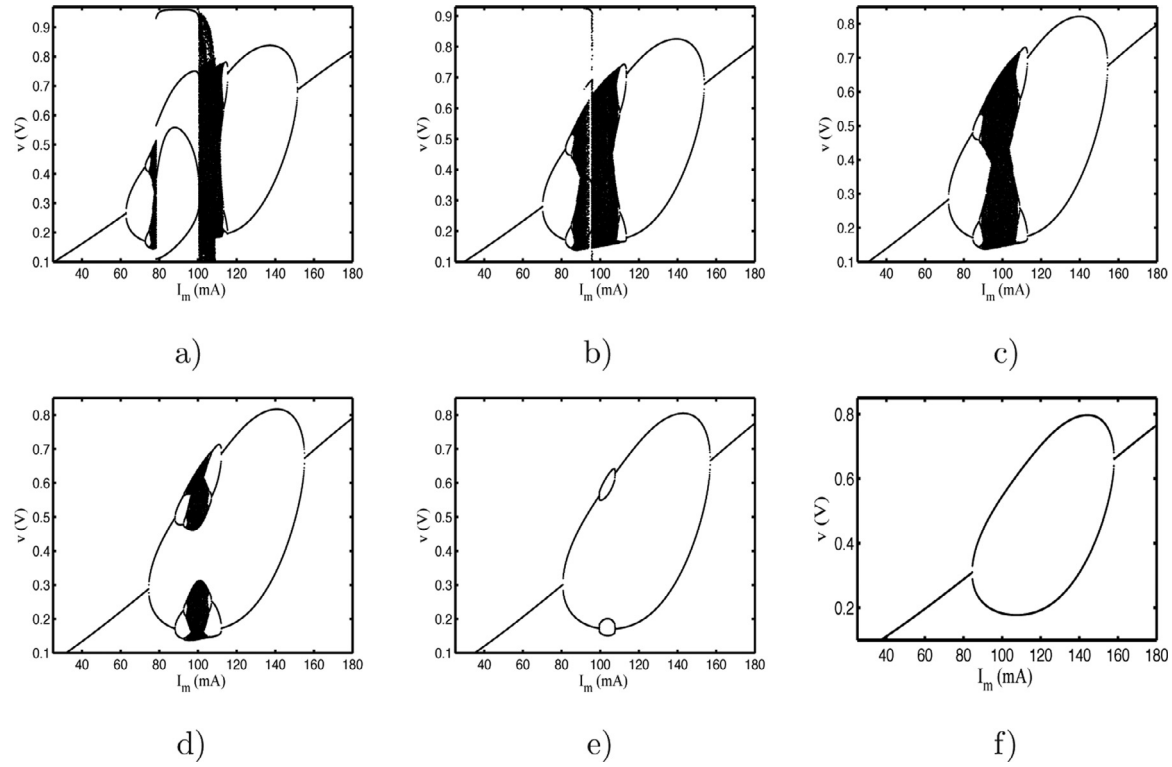

Fig. 9. Different Bifurcation diagrams v versus I_m of the system for different values of the DC component: a) $I_s = 3$ mA, b) $I_s = -3.4$ mA, c) $I_s = -5$ mA, d) $I_s = -7$ mA, f) $I_s = -12$ mA and e) $I_s = -15$ mA.

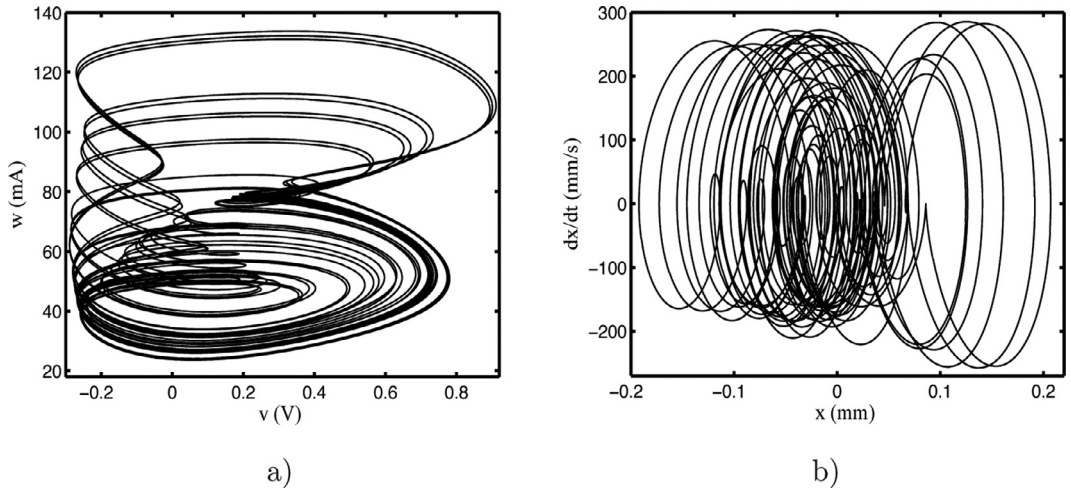

Fig. 10. Phase portraits when $I_s = 3.0$ mA, and $I_m = 102.0$ mA. a) w versus v and b) $\dot{x}$ versus x.

to chaos and also undergoes a reverse period-doubling sequence. These forward and reverse period doubling sequences, as a parameter of the system increases in a monotone way, are called anti-monotonicity. While in the bifurcation diagrams of Figs. 9e) and 9f), only periodic states are observed. For $I_s = -12$ mA, the system undergoes the sequence: $p_1 \to p_2 \to p_4 \to p_2 \to p_1$. For $I_s = -15$ mA, the system undergoes the sequence: $p_1 \to p_2 \to p_1$. These bifurcation diagrams show the period bubble and the primer bubble respectively.

The study of the system (8) with the external current source given by Eq. (19) reveals the existence of chaotic behavior, following the period-doubling route to chaos. Similar results can be obtained using a current source that provides a square signal with DC component I_s and frequency f. For illustration, phase portraits of the system in the chaotic state are shown in Figs. 10a) and 10b).

3. Array of electromechanical arms powered by an array of fitzhugh nagumo neurons

3.1. Description of the model and equations

As mentioned in the introduction, the other goal of this work is to analyze the behavior of a system consisting of an electromechanical system fixed at each node of a discrete line of coupled Fitzhugh-Nagumo type oscillator. The coupling between two neighborhood elements is made by a resistance R_c as illustrated in Fig. 11.

As mentioned previously, the block MS represents the electromechanical system. R_c is an intercellular resistance that represents the coupling resistance between the cells. $n = 1, 2, \cdots, N$, where $N = 6000$ is the total number of cells. Let v_n and u_n be re-

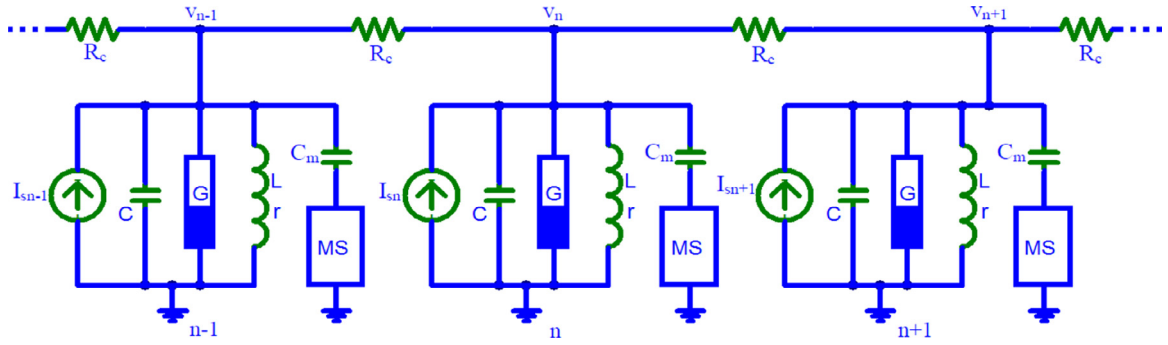

Fig. 11. Schematic representation of the array of Fitzhugh Nagumo coupled to electromechanical arms.

spectively the voltages drop across the capacitances C and C_m in the nth cell. Still in the nth cell, i_n and i_{m_n} are respectively the currents through the inductances L and L_m and x_n is the mechanical displacement of the mobile beam. The application of the Kirchhoff's and Newton laws to the complete system leads to the following differential equations:

$$\begin{cases} C\frac{dv_n}{dt} + i_n + i_{m_n} + \alpha v_n(v_n-\mu_1)(v_n-\mu_2) - \frac{1}{R_c}(v_{n+1}-2v_n+v_{n-1}) = I_{s_n}, \\ L\frac{di_n}{dt} + ri_n = v_n, \\ L_m\frac{di_{m_n}}{dt} + r_m i_{m_n} + u_n - v_n + B\ell\frac{dx_n}{dt} = 0, \\ m\frac{d^2x_n}{dt^2} + \lambda\frac{dx_n}{dt} + Kx_n = B\ell i_{m_n}, \\ C_m\frac{du_n}{dt} = i_{m_n}. \end{cases} \tag{20}$$

We will proceed as we have done in the previous section. Then, considering the dimensionless variables introduced in the previous section: v_n, w_n, z_n, u_n and x_n, the overall system is described by the following nonlinear ordinary differential equations:

$$\begin{cases} \dot{v}_n = a\big(I_{s_n} - \alpha v_n(v_n-\mu_1)(v_n-\mu_2) - w_n - z_n + \frac{1}{R_c}(v_{n+1}-2v_n+v_{n-1})\big), \\ \dot{w}_n = b(v_n - rw_n), \\ \dot{z}_n = d(v_n - u_n - r_m z_n - \gamma\dot{x}_n), \\ \ddot{x}_n = -\beta\dot{x}_n - \varepsilon x_n + \sigma z_n, \\ \dot{u}_n = qz_n. \end{cases} \quad \text{with } 1 \leqslant n \leqslant N \tag{21}$$

The parameters used in the system of Eqs. (21) have been defined in the above section and we will consider $\ell = 4$ m and $L = 240$ mH.

Let us first recall some interesting results when the mechanical part is not connected and the membrane inductance is neglected ($L = 0$ H) in the equivalent circuit. The coupling term in the first equation of system (21) can be approximated with partial derivatives with respect to distance, x', assuming that the spacing between two adjacent units is small. If we assume that the voltage v varies slowly from one unit section to the other, the discrete spatial coordinate n can be replaced by a continuous one x', the network is then described by the following diffusion equation:

$$\frac{1}{R_c}\frac{\partial^2 v}{\partial x'^2} + \frac{1}{a}\frac{\partial v}{\partial t'} - \frac{v}{r} - \alpha v(v-\mu_1)(v-\mu_2) = 0. \tag{22}$$

We start the analysis by looking for wave solutions of Eq. (22) in the form of $v(t', x') = V(\xi)$ where $\xi = x' - V_0 t'$ is a traveling wave variable. This assumption of a traveling wave converts the partial differential Eq. (22) into the second order ordinary differential equation

$$\frac{1}{R_c}\frac{d^2V}{d\xi^2} - \frac{V_0}{a}\frac{dV}{d\xi} - \frac{V}{r} - \alpha V(V-\mu_1)(V-\mu_2) = 0. \tag{23}$$

In the above ordinary differential equation, the traveling wave speed V_0 is an unknown parameter that must be obtained by the analysis. The corresponding traveling wave solution and the traveling wave speed are given by

$$V(\xi) = \frac{\mu_1+\mu_2+A}{4} + \frac{\sqrt{2B}}{4}\tanh\left(\frac{\sqrt{\alpha R_c B}}{4}\xi\right)$$
$$\text{and } V_0 = \frac{a}{4}\sqrt{\frac{2\alpha}{R_c}}(\mu_1+\mu_2-3A), \tag{24}$$

where the newly introduced parameters A and B are worth

$$A = -\sqrt{(\mu_1+\mu_2)^2 - \frac{4}{\alpha r}} \text{ and } B = \mu_1^2+\mu_2^2+(\mu_1+\mu_2)A - \frac{2}{\alpha r}. \tag{25}$$

Next, let us consider the influence of the recovery term in the system (21), where the inductance L and the mechanical part are included. There are no analytical expressions so far, and the results will be achieved in the following sections only through the computer simulations. Nevertheless, the expressions obtained in Eqs. (24) and (25) can provide some ideas. Looking at an understanding of the underlying physical processes and possible technical applications, we additionally study the influence of circuit parameters on the signal waveform.

3.2. Propagation of the signal and motion of the electromechanical arms

The set of discrete differential equations describes the propagation of electrical signal and the motion of N mechanical arms. To determine the propagation conditions, numerical solution is obtained using a fourth order Runge-Kutta algorithm with a time step $\Delta t = 10^{-3}$. The initial conditions are chosen as $v_n(0) = 0$, $w_n(0) = 0$, $x_n(0) = 0$, $\dot{x}_n(0) = 0$, $z_n(0) = 0$ and $u_n(0) = 0$ where $n = 1, 2, \cdots, N$. The boundary conditions are considered for the first and last nodes as $v_0 = v_1$, $v_{N+1} = v_N$. The excitation is performed with a constant current source applied just to the first cell, that is $I_{sn} = 0$ mA for $n \neq 1$.

We will first fix the stimulation current $I_{s1} = 10$ mA and analyze the effect of the coupling resistance R_c. After multiple simulations, we have found that the action potential is created in the first cell and propagates through the other cells for $18.7\,\Omega \leqslant R_c \leqslant 123.7\,\Omega$. Fig. 12 displays the signals propagation in the discrete line and the

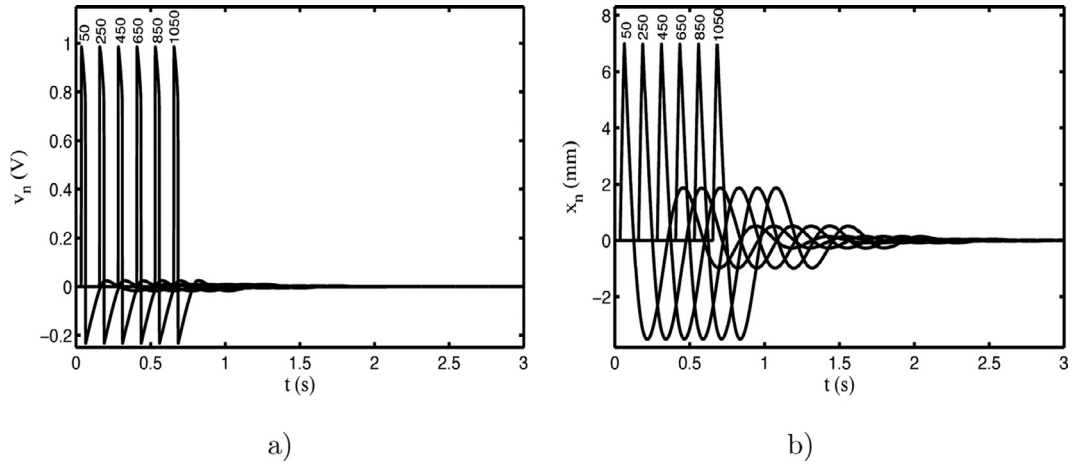

Fig. 12. Time evolution of the system at different cells for $I_{s1} = 10$ mA and $R_c = 20\,\Omega$. a) Membrane potential v_n, b) Displacement of the mechanical arm x_n. The rang of the corresponding cell is indicated in each curve.

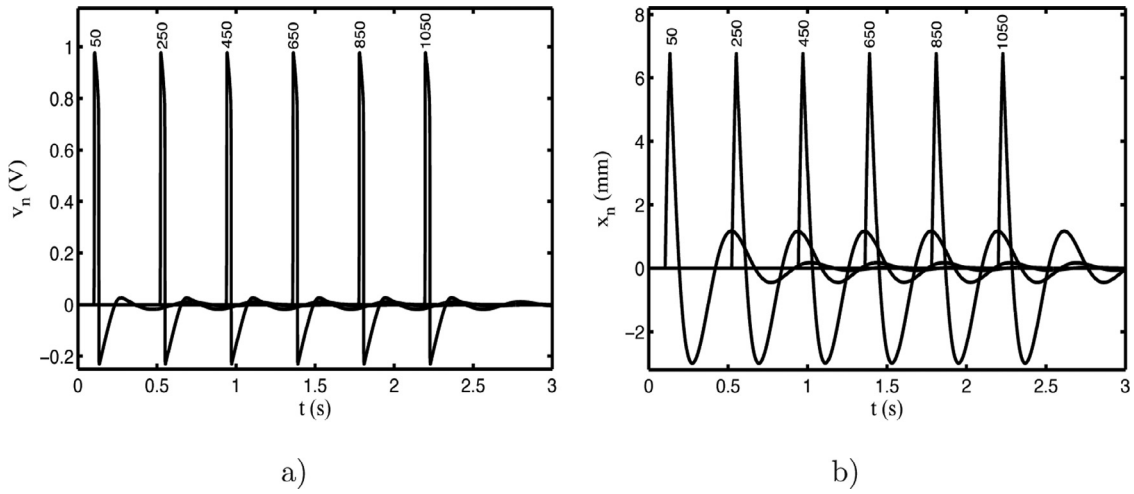

Fig. 13. Time evolution of the system at different cells for $I_{s1} = 10$ mA and $R_c = 80\,\Omega$. a) Membrane potential v_n, b) Displacement of the mechanical arm x_n. The rang of the corresponding cell is indicated in each curve.

behavior of the mobile beams when the action potential propagates in the line for $R_c = 20\,\Omega$.

Figs. 12a) and 12b) show respectively the propagation of the action potentials v_n and the displacement x_n of the mobile beams as a function of time for different cells such as $n = 50$, $n = 250$, $n = 450$, $n = 650$, $n = 850$, $n = 1050$. As shown in these Figures, the action potential shape is preserved during the propagation and each electromechanical subsystem exhibits a pulse-like behavior moving from its resting state, then increases to a maximal value and then decreases to the resting state. This observation is interesting since it indicates that the mobile beam executes an actuation work and then returns to its resting state. This profile is similar to the use of legs of artificial millipedes.

During our numerical investigations, we found that the traveling wave speed decreases as the coupling resistance increases. This fact is qualitatively in good agreement with the analytical expression of V_0 given in Eq. (24). For verification, the time evolution of the system at different cells is presented in Fig. 13 for $R_c = 80\,\Omega$.

The graphs in Figs. 12 and 13 are plotted for the same values of the parameters except that the first ones are plotted for $R_c = 20\,\Omega$ and the second ones for $R_c = 80\,\Omega$. We can notice that the traveling wave speed has decreased when the coupling resistance is increased from $20\,\Omega$ to $80\,\Omega$. A part of that traveling wave speed, the curves of Figs. 12 and 13 have the same behavior.

3.3. Effect of the stimulation current

We continue our investigations by analyzing the behavior of the discrete line when the stimulation current is increased to $I_{s1} = 25$ mA. We have then notice that, for certain values of the coupling resistance, an envelope of action potential propagates in the line. Our results plotted for $R_c = 100\,\Omega$ are shown in Fig. 14.

Fig. 14a) and Fig. 14b) show respectively the behavior of the nonlinear electrical line and the behavior of some electromechanical systems for different cells such as $n = 50$, $n = 250$, $n = 450$, $n = 650$, $n = 850$, $n = 1050$. A packet of three action potentials is provided by the first cell and propagates through the line. Each mechanical arm exhibits a packet of three pulse-like behavior before returning to rest.

3.4. Space-time evolution of mechanical arms

Finally, we present respectively in Fig. 15a) and 15b) the spatiotemporal evolution of the mechanical arm and the spatiotemporal variation between displacements of the arm of nearest-neighbor defined as $shift(t) = x_i(t) - x_{i+1}(t)$.

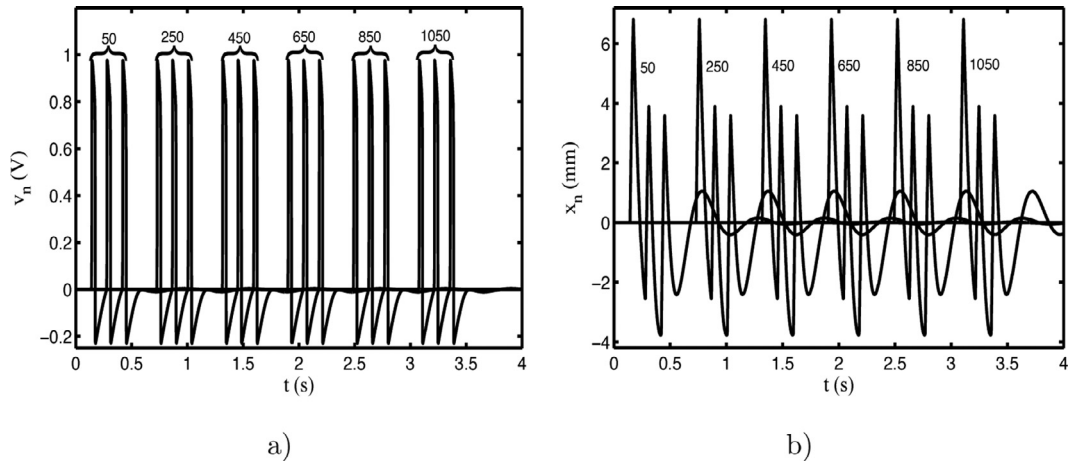

Fig. 14. Time evolution of the system at different cells for $I_{s1} = 25$ mA and $R_c = 100\,\Omega$. a) Membrane potential v_n, b) Displacement of the mechanical arm x_n. The rang of the corresponding cell is indicated in each curve.

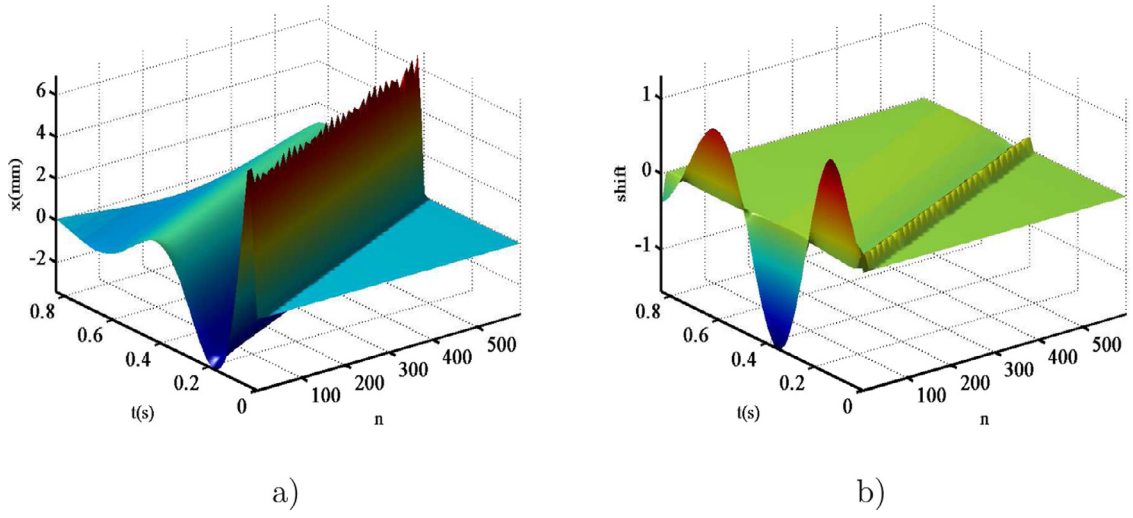

Fig. 15. a) Spatiotemporal evolution of the mechanical arm and b) spatiotemporal variation of dynamical shift.

4. Conclusion

We have firstly analyzed the dynamics of one single Fitzhugh-Nagumo neuron coupled to a mechanical arm. In this case, we have presented the oscillation boundaries where we have shown that for certain values of stimulation current, the system can converge towards the equilibrium point and for other values, the system can fall in oscillation or display a limit cycle behavior. The oscillation frequency and the oscillation conditions were determined. Forward period-doubling bifurcation sequences followed by reverse period-doubling sequences, as a parameter is varied in a monotone way, antimonotonicity is observed in the system.

Secondly, the investigations of an array of electromechanical arms powered by an array of discrete excitable Fitzhugh-Nagumo have been done. When the first cell is excited, the nerve impulse propagates in the electrical line, and each mechanical arm displays a pulse-like behavior. It was found that the train of three pulses can also propagate through the line according to the coupling strength.

Declaration of Competing Interest

The authors declare that they have no known competing financial interests or personal relationships that could have appeared to influence the work reported in this paper.

CRediT authorship contribution statement

N.K. Mbeunga: Writing – original draft, Data curation. **B. Nana:** Conceptualization, Methodology, Writing – review & editing. **P. Woafo:** Supervision, Writing – review & editing.

References

[1] Keener JP. Propagation and its failure in coupled systems of discrete excitable cells. SIAM J Appl Math 1987;47:556–72.
[2] Izhikevich EM. 2007 Dynamical systems in neuroscience. the geometry of excitability and bursting. the MIT press; 2007.
[3] Berglund N, Landon D. Mixed-mode oscillations and interspike interval statistics in the stochastic fitzhugh-nagumo model. Nonlinearity 2012;25:0951–7715.
[4] Zhang X, Wang W, Liu Q, Zhao X, Wei J, Cao R, Yao Z, Zhu X, Zhang F, Lv H, Long S, Liu M. An artificial neuron based on a threshold switching memristor. IEEE Electron Device Lett 2017;39:308–11.
[5] Kang Q, Huang BY, Zhou MC. Dynamic behavior of artificial hodgkin-huxley neuron model subject to additive noise. IEEE Trans Cybern 2015;46:2083–93.
[6] Hasegawa H. Responses of a hodgkin-huxley neuron to various types of spike–train inputs. Phys Rev E 2000;61:718–26.
[7] Dynamical phases of the hindmarsh-rose neuronal model. Studies of the transition from bursting to spiking chaos.
[8] Wu K, Luo T, Lu H, Wang Y. Bifurcation study of neuron firing activity of the modified hindmarsh-rose model. Neural Computing and Applications 2016;27:739–47.
[9] Hu X, Liu C, Liu L, Ni J, Li S. An electronic implementation for morris-lecar neuron model. Nonlinear Dyn 2016;84:2317–32.

[10] Shi M, Wang Z. Abundant bursting patterns of a fractional-order morris-lecar neuron model. Commun Nonlinear Sci Numer Simul 2014;19:1956–69.
[11] Wang J, Zhang T, Deng B. Synchronization of fitzhugh-nagumo neurons in external electrical stimulation via nonlinear control. Chaos, Solitons and Fractals 2007;31:30–8.
[12] Abbasian AH, Fallah H, Razvan MR, Cybern B. Symmetric bursting behaviors in the generalized fitzhugh-nagumo model 2013;107:465–76.
[13] Cosp J, Binczak S, Madrenas J, Fernández D. Implementation of compact VLSI fitzhugh-nagumo neurons. IEEE International Symposium on Circuits and Systems 2013;101:2370–3.
[14] Armanyos M, Radwan AG. 13Th international conference on electrical engineering/electronics. Computer Telecommunications and information Technology; 2016.
[15] Keener JP. Analog circuitry for the van der pol and fitzhugh-nagumo equations. IEEE Trans Syst Man Cybern 1983;13:1010–14.
[16] Alford JG. Models of unidirectional propagation in heterogeneous excitable media. Appl Math Comput 2010;216:1337–48.
[17] Cattani A. Fitzhugh-nagumo equations with generalized diffusive coupling. Mathematical Biosciences and Engineering 2014;11:203–15.
[18] García-Ojalvo J, Báscones R, Sagués F, Sancho JM, Schimansky-Geier L. Pulse propagation in bistable neural models via noise—induced resetting. AIP Conf Proc 2003;665:35–42.
[19] Makarov VA, Nekorkin VI, Velarde MG. Spiking behavior in a noise–driven system combining oscillatory and excitatory properties. Phys Rev Lett 2001;86:3431–4.
[20] Kostova T, Ravindran R, Schonbek M. Fitzhugh-nagumo revisited: types of bifurcations, periodical forcing and stability regions by a lyapunov functional. Internat J Bifur Chaos 2004;14:913–25.
[21] Zhang GJ, Xu JX. Stochastic resonance induced by novel random transitions of motion of fitzhugh-nagumo neuron model. Chaos Solitons and Fractals 2005;23:1439–49.
[22] Wang J, Zhang T, Deng B. Synchronization of fitzhugh-nagumo neurons in external electrical stimulation via nonlinear control. Chaos Solitons and Fractals 2007;31:30–8.
[23] Soriano DC, Machado MLC, Nadalin EZ, Suyama R, Attux R, Cajueiro JPC, Romano JMT. Proposal and analysis of a fitzhugh-nagumo neuronal circuit. IFAC Proceeding 2012;45:220–5.
[24] Nguyen LH, Hong KS. Synchronization of coupled chaotic fitzhugh-nagumo neurons via lyapunov functions. Math Comput Simul 2011;82:590–603.
[25] Zheng Z, Cross MC. Defect-induced propagation in excitable media. Internat J Bifur Chaos 2003;13:3125–33.
[26] Elmer CE, Van-Vleck ES. Spatially discrete fitzhugh-nagumo equations. SIAM J Appl Math 2004;65:1153–74.
[27] Klofaï Y, Essimbi BZ, Jäger D. An MMIC implementation of fitzhugh-nagumo neurons using a resonant tunneling diode nonlinear transmission line. Phys Scr 2015:1–7.
[28] Keener JP. Propagation and its failure in coupled systems of discrete excitable. Siam J Appl Appl Math 1987;47:556–72.
[29] Erneux T, Nicolis G. Propagating waves in discrete bistable reaction-diffusion systems. Physica D 1993;67:237–44.
[30] Anderson ARA, Sleeman BD. Wave front propagation and its failure in coupled systems of discrete bistable cells modelled by fitzhugh-nagumo dynamics. Internat J Bifur Chaos 1995;5:63–74.
[31] Booth V, Erneux T. Understanding propagation failure as a slow capture near a limit point. Siam J Appl Appl Math 1995;55:1372–89.
[32] Ratas I, Pyragas K. Effect of high-frequency stimulation on nerve pulse propagation in the fitzhugh-nagumo model. Nonlinear Dyn 2012;67:2899–908.
[33] Binczak S, Bilbault JM. Experimental propagation failure in a nonlinear electrical lattice. Internat J Bifur Chaos 2004;14:1819–30.
[34] Gurevich P, Reichelt S. Pulses in fitzhugh–nagumo systems with rapidly oscillating coefficients. multiscale Model Simul 2018;16:833–56.
[35] Mboussi NA, Noubissie S, Woafo P. Dynamics of arrays of legs powered by a discrete electrical model of nerve. Phys Lett A 2014;378:857–62.
[36] Kouami NM, Nana B, Woafo P. Analysis of array nanoelectromechanical beams driven by an electrical line of josephson junctions. Physica C: Supercond and Applicat 2020;574:1–8.
[37] Chedjou JC, Woafo P, Domngang S. Shilnikov chaos and dynamics of a self-sustained electromechanical transducer. J Vib Acoust 2001;123:170–4.
[38] Kitio Kwuimy CA, Woafo P. Dynamics, chaos and synchronization of self-sustained electromechanical systems with clamped-free flexible arm. Nonlinear Dyn 2008;53:201–14.
[39] Yamapi R, Aziz-Alaoui MA. Vibration analysis and bifurcations in the self-sustained electromechanical system with multiple functions. Commun Nonlinear Sci Numer Simul 2007;12:1534–49.
[40] Kitio Kwuimy CA, Woafo P. Experimental realization and simulations a self-sustained macroelectromechanical system. Mech Res Commun 2010;37:106–10.
[41] Kitio Kwuimy CA, Nana B, Woafo P. Experimental bifurcations and chaos in a modified self-sustained macro electromechanical system. J Sound Vib 2010;329:3137–48.
[42] Tlidi M, Mandel P, Lefever R. Localized structures and localized patterns in optical bistability. Phys Rev Lett 1994;73:640–4.
[43] Shen JJ, Yin HW, Dai JH. Dynamical behavior, transient chaos, and riddled basins of two charged particles in a paul trap. Phys Rev A 1997;55:2159.
[44] Tél T. The joy of transient chaos. Chaos 2015;25:097619.